

# Development of an 80 Gbit/s InP-based Mach-Zehnder Modulator

vorgelegt von  
M. Sc. Haitao Chen  
aus Nanjing (V.R. China)

Von der Fakultät IV - Elektrotechnik und Informatik  
der Technischen Universität Berlin  
zur Erlangung des akademischen Grades  
Doktor der Ingenieurwissenschaften  
- Dr.-Ing. -

genehmigte Dissertation

Promotionsausschuss:

Vorsitzender: Prof. Dr. rer. nat. G. Tränkle

Berichter: Prof. Dr.-Ing. K. Petermann

Berichter: Prof. Dr. rer. nat. D. Jäger (Uni Duisburg-Essen)

Tag der wissenschaftlichen Aussprache: 26.10.2007

Berlin 2007

D 83

© 2007 Haitao Chen

Gedruckt mit Unterstützung des Deutschen Akademischen Austauschdienstes.

## **Dedication**

To my parents, my wife and my daughter

## **Acknowledgements**

First of all I would like to thank Professor Klaus Petermann and Dr. Herbert Venghaus for their supervision, inspiration, and guidance throughout all of this work.

It has certainly been satisfying and rewarding to work with the modulator research group in Heinrich-Hertz-Institut. I offer my thanks to the members of the group for their long-term valuable help. Special thanks to Dr. Karl-Otto Velthaus and Dr. Detlef Hoffmann who helped me in this work. I would like to thank them also for their valuable advices, support, encouragement and valuable comments in writing of this dissertation and the published papers. Also, thanks to Dr. Ronald Kaiser, Holger Klein, Giorgis G. Mekonnen, Gabriele Bader, Bärbel Reinsperger, and Martin Gravert for their valuable help.

I would like also to acknowledge DAAD (the German Academic Exchange Service) and CSC (the China Scholarship Council), who give me the chance and financial support to accomplish my doctor study in Germany.

## Abstract

In this work, integrated InP-based electro-optical Mach-Zehnder modulators with capacitively loaded traveling-wave electrode are developed and characterized. The  $\pi$  phase shift in the upper and lower arm of the Mach-Zehnder interferometer is generated by electro-refraction due to the Quantum Confined Stark-Effect in a 20 period InGaAsP/InP multi quantum well (MQW) layer stack, which ensures a low driving voltage.

This thesis focuses on the microwave design and the optimization of the modulator. The basic theory that used in design and optimization are presented at first. Three different models are introduced and used for optimization. The significant design parameters of a capacitively loaded traveling wave electrode Mach-Zehnder modulator are analyzed in detail. Several optimizing strategies are given for reducing the microwave loss and improving the velocity match.

The experimental results suggest a packaged modulator has a 3 dB<sub>eo</sub> bandwidth of 45.6 GHz and the driving voltage of 2.6 V with -2.8 V bias. The bandwidth achieves 57 GHz after optimizing the p-contact and decreasing the n-bulk resistance in the modulator, as well as improving the velocity matching by inserting a BCB buffer layer under the traveling wave electrodes. Measurements show that the packaged modulator module has a clear open NRZ eye diagram at 80 Gbit/s data rate.



## Table of Contents

List of Tables .....	ix
List of Figures .....	x
List of Symbols .....	xv
List of Abbreviations .....	xviii
Chapter 1 .....	1
Introduction .....	1
1.1 Overview .....	1
1.2 Organization of the Dissertation .....	2
1.3 Direct Modulation .....	3
1.4 External Modulators .....	5
1.4.1 Electro-Optic Modulators .....	6
1.4.1.1 Directional coupler .....	6
1.4.1.2 Mach-Zehnder Interferometer .....	7
1.4.1.3 Materials .....	8
1.4.2 Electroabsorption Modulators .....	13
1.4.3 Comparison of Different Types of External Modulators .....	15
1.5 Motivation for the work .....	16
References .....	18
Chapter 2 .....	21
Basic Theory .....	21
2.1 Coplanar Lines .....	21
2.2 Transmission Line Theory .....	25
2.2.1 The Lumped-element Circuit Model of Transmission Line .....	26
2.2.2 Propagation Parameters of the Transmission Line .....	27
2.2.3 Analysis of the Periodically Loaded Transmission Line .....	29
2.3 III-V Compound Material .....	31
2.4 p-i-n Diode .....	33
2.4.1 p-n Junction .....	33

2.4.2	p-i-n junction.....	37
2.5	Metal-semiconductor Contacts .....	38
2.5.1	Ohmic Contact .....	38
2.5.2	Extracting the Contact Resistance .....	39
2.6	The Electro-optic Coefficient .....	41
2.7	Quantum Confined Stark Effect (QCSE).....	44
2.8	Chirp Analysis .....	47
	References.....	48
Chapter 3.....		49
Mach-Zehnder Modulator Design.....		49
3.1	Mach-Zehnder Interferometer.....	49
3.2	Electrode Consideration.....	51
3.2.1	Lumped Electrode.....	51
3.2.2	Push-Pull Structure .....	53
3.2.3	Traveling-Wave Electrode.....	56
3.3	Microwave Design.....	59
3.4	Definition of Electrical and Electro-Optical Bandwidth .....	61
3.5	Driving Voltage $V_{\pi}$ .....	66
	References.....	68
Chapter 4.....		69
Optimization towards Higher Speed and Lower Driving Voltage.....		69
4.1	Electromagnetic Simulation.....	69
4.1.1	Introduction of High Frequency Structure Simulator .....	69
4.1.2	Modeling Modulator in HFSS .....	73
4.1.2.1	Material Properties.....	73
4.1.2.2	Geometry and Corresponding Boundary Conditions .....	77
4.1.3	Simulation Results .....	81
4.2	The simple Circuit Model for the Modulator.....	82
4.3	Determining the Parameters for the Circuit Model.....	85
4.3.1	$L_0$ and $C_0$ of the CPS.....	85
4.3.2	Capacitance of the p-i-n Diode $C_{pin}$ .....	86
4.3.3	The Inductance of the Air Bridge in the Modulator .....	86

4.3.4	Parasitic Capacitance in the Modulator .....	87
4.3.5	The Resistances in the Active Area of a Modulator .....	89
4.4	Detailed Circuit model and Simulation Results .....	90
4.5	Bragg Frequency .....	93
4.6	Towards Velocity Match.....	95
4.6.1	Optical Group Index ( $n_{opt}$ ) .....	96
4.6.2	Microwave Effective Refractive Index ( $n_{\mu}$ ).....	97
4.6.3	The Strategy Towards Velocity Match .....	100
4.6.4	Co- and Counter-propagation .....	102
4.7	Minimization the Microwave Loss in the Modulator .....	104
4.7.1	The Microwave Loss in the Traveling-Wave Electrode .....	104
4.7.1.1	The Microwave Loss in the Normal CPS .....	104
4.7.1.2	The Microwave Loss in the CPS with Mesa.....	106
4.7.2	The Microwave Loss in the Active Area .....	107
4.7.2.1	Series Resistance Analysis.....	108
4.7.2.2	Optimizing the p-Contact Resistivity.....	110
4.7.3	Simulation Results of Optimized Modulator .....	111
4.8	Optimization Towards Lower Driving Voltage.....	113
4.9	Redesign of the Electrode Geometry .....	117
	References.....	120
Chapter 5.....		123
Fabrication and Packaging.....		123
5.1	Fabrication .....	123
5.2	Packaging.....	125
5.2.1	Optical Input and Output .....	125
5.2.2	The Module.....	126
5.2.3	Electrical Bonding and Connection .....	127
	References.....	133
Chapter 6.....		134
Characterization of Modulators and Measurements .....		134
6.1	C-V Characteristic Measurement.....	134
6.2	Measurement of the p-Contact Resistance.....	136

6.3	DC Measurements.....	138
6.4	S-Parameter Measurement.....	141
6.5	Electro-optic Measurement.....	141
6.6	System Measurements.....	144
	References.....	147
Chapter 7.....		148
Measured Results and Conclusions.....		148
7.1	Measured Results of Modulator.....	148
7.1.1	Measured Results of the First Generation 80 Gbit/s Modulator .....	148
7.1.2	Measured Results of the Second Generation 80 Gbit/s Modulator.....	153
7.2	Conclusions and Outlook.....	154
	Reference.....	154
Appendix A	The Scattering Matrix & the Transmission Matrix.....	155
Appendix B	Euler's formula.....	157
Appendix C	.....	158

## List of Tables

Table 1.1: Comparison of several types of optical intensity modulators.....	15
Table 4.1 Important physical properties of III-V compound materials [3].....	74
Table 4.2 Calculated material properties for modulator modeling in HFSS .....	75
Table 4.3 Material properties of the p-region with different built-in p-contact resistivity.....	76
Table 4.4 Calculated resistances in the active area of the modulator .....	89
Table 4.5 Comparison of parameters before and after optimizing .....	112
Table I Electron mobility, carrier concentration in n-type InP at 300K [2, 3] .....	158

## List of Figures

Fig. 1.1 A transmitter in a 40 Gbit/s ETDM system .....	2
Fig. 1.2 Transition function of a current modulated semiconductor laser [2] .....	4
Fig. 1.3 Direct modulation scheme .....	4
Fig. 1.4 External modulation scheme .....	5
Fig. 1.5 Schematic of a directional coupler .....	6
Fig. 1.6 Schematic of a Mach-Zehnder interferometer with 2 Y-branches .....	7
Fig. 1.7 Measured electro-optical response of a modulator .....	17
Fig. 2.1 CPW geometry and corresponding electric and magnetic field distribution [1] .....	21
Fig. 2.2 CPS geometry and corresponding electric and magnetic field distribution [1] .....	22
Fig. 2.3 Asymmetric CPS .....	22
Fig. 2.4 Calculated characteristic impedance as function of different geometry parameters of CPS using semi-isolating InP as substrate .....	24
Fig. 2.5 Voltage and current definitions and equivalent circuit for an incremental length of transmission line .....	26
Fig. 2.6 A two-port network model for the transmission line.....	28
Fig. 2.7 A periodically loaded transmission line .....	29
Fig. 2.8 Equivalent circuit of a unit cell in Fig. 2.7, uniform transmission line with shunt element in center .....	29
Fig. 2.9 Lattice constant and bandgap energies of ternary and quaternary compounds formed by using III-V group semiconductors [10] .....	32
Fig. 2.10 p-n junction under (a) reverse and (b) forward bias .....	34
Fig. 2.11 Distributed resistance model of a contact to a thin semiconductor layer .....	39
Fig. 2.12 (a) A TLM test structure and (b) contact resistance versus contact spacing .....	40
Fig. 2.13 Illustration of index ellipsoid, the dashed ellipse is the intersection of the index ellipsoid with the plane normal to the propagation direction.....	41
Fig. 2.14 Energy levels of a QW structure without and with applied electric field [16] .....	44
Fig. 2.15 Simulated absorption spectra for a QW under different electric field [15] ..	46

Fig. 3.1 Schematic of a Mach-Zehnder Interferometer with 2 Y-branch .....	49
Fig. 3.2 Transfer curve for MZI with 2 Y-branches .....	50
Fig. 3.3 Transfer curve of an MZI with 2 Y-branches with optical loss, $b=0.9$ .....	51
Fig. 3.4 Schematic of a MZM with a lumped electrode .....	52
Fig. 3.5 Cross section of the optical waveguide covered with a lumped electrode .....	52
Fig. 3.6 The equivalent circuit model for the MZM with a lumped electrode .....	52
Fig. 3.7 Schematic of a MZM with push-pull lumped electrodes .....	54
Fig. 3.8 The circuit model for series push-pull [4] .....	54
Fig. 3.9 Schematic of a MZI with one Y-branch and a $2 \times 2$ MMI and the ideal transfer matrix for each section.....	54
Fig. 3.10 Transmission character of Mach-Zehnder interferometer .....	56
Fig. 3.11 Intensity modulation using push-pull structure .....	56
Fig. 3.12 Schematic of a MZM with capacitive loaded segmented traveling-wave electrode.....	58
Fig. 3.13 Cross sectional view of a MZM with DC bias and HF circuit diagram .....	58
Fig. 3.14 Microwave design of the capacitively loaded TWE MZM .....	60
Fig. 3.15 Equivalent circuit of a traveling-wave electrode modulator .....	61
Fig. 4.1 Flow chart of general design process of HFSS.....	72
Fig. 4.2 Flow chart of the HFSS adaptive refinement process .....	73
Fig. 4.3 Simplified p-layer in modulator modeling in HFSS.....	76
Fig. 4.4 Carrier concentration of different layers in modulator with varied bias [7]... 77	77
Fig. 4.5 Top-view of a whole chip modulator model with 12 sections in HFSS.....	78
Fig. 4.6 (a) A section of modulator (b) An N-section segmented modulator .....	78
Fig. 4.7 An 8-cell 2-port network in Ansoft Designer .....	79
Fig. 4.8 (a) Top-view (b) Side-view of a single-section modulator model in HFSS... 80	80
Fig. 4.9 A 3-D view of a single-section modulator model with excitation and boundary condition .....	80
Fig. 4.10 Comparison between measured and simulated electrical insertion loss $S_{21}$ of the same modulator structure .....	81
Fig. 4.11 Microwave equivalent model for the TWE MZM.....	82
Fig. 4.12 One cell of the modulator and its transmission matrix.....	83

Fig. 4.13 Transmission matrix representation of TWE MZM.....	84
Fig. 4.14 Calculated $L_0$ and $C_0$ for an unloaded CPS.....	85
Fig. 4.15 Measured bias dependent capacitance of circular p-i-n diodes .....	86
Fig. 4.16 SEM photo of inner electrodes of the modulator .....	87
Fig. 4.17 Parasitic capacitance in the active area of a modulator .....	88
Fig. 4.18 The resistances in the active area of a modulator .....	89
Fig. 4.19 The hierarchical model for one section of a modulator in an EDA tool .....	90
Fig. 4.20 Circuit models of passive part and active part in a section of the modulator .....	90
Fig. 4.21 12-section TWE MZM model in ADS .....	91
Fig. 4.22 The simulation results using the detailed model .....	92
Fig. 4.23 Measured $S_{21}$ parameters of two modulators ( $l=3$ mm, $\eta=0.4$ ) with 250 $\mu\text{m}$ and 500 $\mu\text{m}$ period length, respectively .....	93
Fig. 4.24 The propagation of optical and electrical signals in the modulator [14] .....	95
Fig. 4.25 Measured data of a 12.2 mm long waveguide by the Fabry-Perot method ..	97
Fig. 4.26 Measured $S_{11}$ and converted corresponding $n_\mu$ of a modulator (#45C63) ....	98
Fig. 4.27 Measured phase and converted corresponding $n_\mu$ of a modulator (#45C63) ..	99
Fig. 4.28 Microwave index and the optic index of two modulators .....	100
Fig. 4.29 Cross-sectional view of CPS test structures .....	101
Fig. 4.30 Microwave indices of unloaded TWE test structures .....	101
Fig. 4.31 Electro-optical response of the modulators with and without BCB layer ..	102
Fig. 4.32 The electro-optical responses of a modulation under co- and counter-propagation conditions, respectively .....	103
Fig. 4.33 The CPS structures simulated in HFSS .....	105
Fig. 4.34 Simulated insertion loss of 1 mm CPS .....	105
Fig. 4.35 CPS with mesa.....	106
Fig. 4.36 The impact of mesa width on the insertion loss of the CPS .....	107
Fig. 4.37 The impact of the series resistance in the active area on the insertion loss of the modulator ( for $R_c=10.7 \Omega$ , the corresponding $\rho_c$ is $3 \times 10^{-5} \text{ cm}^2 \cdot \Omega$ ).....	108
Fig. 4.38 Simulated insertion loss of modulators with different $\rho_c$ using HFSS .....	110
Fig. 4.39 Simulation results of optimized modulator with different fill factors .....	112

Fig. 4.40 The relationship between the 3 dB <sub>e0</sub> bandwidth, the driving voltage and the fill factor of a modulator .....	114
Fig. 4.41 Measured C-V curves with two different i-region thickness.....	115
Fig. 4.42 The measured V <sub>π</sub> before and after optimizing i-layer's thickness.....	116
Fig. 4.43 Loading capacitance as function of microwave index of the unloaded CPS .....	116
Fig. 4.44 Cross sectional view of the modulator (a) before and (b) after redesign ...	117
Fig. 4.45 Characteristic impedance for CPS as a function of aspect ratio a/b.....	118
Fig. 4.46 Flow chart of the redesign process .....	119
Fig. 5.1 SEM photo of a pair of air bridges between TWE and optical waveguide in a fabricated modulator .....	124
Fig. 5.2 SEM photo of one side of a fabricated modulator.....	124
Fig. 5.3 (a) A 3-D model of the spot size converter with field distribution for the fundamental mode in the passive and fiber port waveguide, respectively (b) Alignment tolerances measured at the input port of the modulator compared to that of the tolerances of a tapered fiber to a passive waveguide [1] .....	125
Fig. 5.4 The CAD drawing of a packaged modulator module.....	126
Fig. 5.5 Measured electrical loss S <sub>21</sub> of a modulator before and after packaging .....	127
Fig. 5.6 A simplified 3-D model in HFSS .....	128
Fig. 5.7 Top-view and side-view of the 3-D model of a packaged module and simulation results .....	129
Fig. 5.8 Bonding wires (a) two bonding wires for each connection, (b) five bonding wires for ground and three for signal.....	130
Fig. 5.9 An optimized integrated CPS-CPW transition in a modulator.....	131
Fig. 5.10 Three different configurations of input and output pads (a) asymmetrical S-G configuration, (b) symmetric S-G configuration, (c) G-S-G pads, (d) measured electrical insertion losses of the three different configurations .....	131
Fig. 5.11 The module using G-S-G pads with long ground bar on the middle block	132
Fig. 5.12 The module using G-S-G pads with separated middle blocks.....	133
Fig. 5.13 Simulated electrical insertion loss S <sub>21</sub> of a modulator before and after optimized packaging .....	133
Fig. 6.1 The circular diode test structure: top view and cross sectional view. ....	134
Fig. 6.2 Measured C-V characteristic of round diodes .....	135

Fig. 6.3 Intrinsic layer thickness over bias voltage deduced from C-V measurements .....	135
Fig. 6.4 Layout of one TLM structure ( $w_c=100 \mu\text{m}$ ) .....	136
Fig. 6.5 Measured p-contact resistivities of two modulator wafers .....	137
Fig. 6.6 Setup of DC matrix measurement [2] .....	139
Fig. 6.7 (a) Normalized optical transmission with applied voltage to I- and U-electrode. (b) The transfer curve of the corresponding operating point in (a) .....	140
Fig. 6.8 The setup of electrooptic response measurement (200 MHz – 65 GHz) [3]	143
Fig. 6.9 Setup for 40 Gbit/s eye-diagram measurements of modulator .....	145
Fig. 6.10 Setup for 80 Gbit/s eye-diagram measurements of modulator .....	146
Fig. 7.1 A packaged modulator module [1] .....	149
Fig. 7.2 Normalized output vs. driving voltage of the module (#45 A50) at -2.8 V bias .....	149
Fig. 7.3 EO response of the packaged MZI modulator (#45 A50) at -2.8 V bias [1]	150
Fig. 7.4 Measured NRZ eye diagram of the packaged MZI modulator (#45 A50) at 40 Gbit/s with $1.55 \mu\text{m}$ optical signal (PRBS word length: $2^{31}-1$ , 10 ps/div) [1] .....	150
Fig. 7.5 Measured 40 Gbit/s PRBS BER curves of the packaged modulator (#45A50) .....	151
Fig. 7.6 Measured NRZ eye diagram of the packaged MZI modulator (#45 A50) at 80 Gbit/s with $1.55 \mu\text{m}$ optical signal (PRBS word length: $2^{15}-1$ , 5ps/div) .....	152
Fig. 7.7 Electro-optical response of a modulator (on-chip) with a TWE length of 4 mm. ( $l_E=200 \mu\text{m}$ , $A=500 \mu\text{m}$ , -6 V bias) .....	153
Fig. A.1 An arbitrary N-port network [1] .....	155
Fig. A.2 A two-port network .....	156
Fig. A.3 A cascade connection of two two-port networks .....	156

## List of Symbols

$\alpha$	Microwave attenuation constant
$\alpha_c$	attenuation constant due to Ohmic loss
$\alpha_{chirp}$	chirp parameter
$\alpha_d$	attenuation constant due to dielectric loss
$\beta_\mu$	complex microwave propagation constant of the signal in the electrode
$\beta_{opt}$	complex optical propagation constant of the signal in the optical waveguide
$\beta_{opt}^\mu$	velocity mismatch in the modulator
$\gamma$	complex transmission constant
$\delta$	skin effect factor
$\epsilon_{eff}$	effective dielectric constant
$\eta$	fill factor of a modulator
$\lambda$	wavelength
$\lambda_0$	wavelength in free space
$\Lambda$	period length of a modulator
$\mu_e$	electron mobility
$\mu_h$	hole mobility
$\rho_1$	input electrode structure reflection coefficient
$\rho_2$	output electrode structure reflection coefficient
$\rho_c$	contact resistivity
$\sigma$	conductivity
$\omega_m$	modulation frequency
$\phi(f)$	accumulated phase delay of $S_{21}$
$a$	lattice constant
$b$	optical imbalance factor in MZI
$C_0$	shunt capacitance per unit length

$C_L$	loading capacitance of a modulator per unit length
$C_{pin}$	junction capacitance of the p-i-n diode per unit area
$C_s$	parasitic capacitance per unit length
$d$	distance between two optical waveguides
$d_b$	diameter of the air-bridge
$d_i$	thickness of intrinsic layer
$d_p$	thickness of the p-layer
$d_{pin}$	depletion layer width of reverse biased pin diode
$d_s$	skin depth
$E_g$	bandgap energy
$f_{Bragg}$	Bragg frequency
$G_0$	shunt conductance per unit length
$l$	traveling-wave electrode length
$L_0$	series inductance per unit length
$L_b$	inductance of the air-bridge
$l_b$	length of the air-bridge
$l_E$	active electrode length
$l_{eff}$	effective modulation length
$n$	electron density
$n_0$	optical index of the active layer at zero applied voltage
$n_{opt}$	optical index
$n_\mu$	microwave index
$n_\mu'$	microwave index of the loaded CPS
$p$	hole density
$P_{in}$	input optical power
$P_{out}$	output optical power
$r$	modulation reduction factor
$R_0$	series resistance per unit length
$R_c$	contact resistance
$r_{ij}$	electro-optic coefficient
$R_n$	bulk resistance of the n-layer

$R_p$	bulk resistance of the p-layer
$R_{sh}$	sheet resistance
$\tan\delta$	dielectric loss tangent
$T_{MZI}$	optical intensity transfer function
$v_u$	velocity of the electrical signal
$V_g$	amplitude of the generator voltage
$v_{gr-o}$	group velocity of the optical signal
$v_{opt}$	velocity of the optical signal
$v_p$	phase velocity
$V_\pi$	driving voltage
$w_c$	width of the contact
$w_{wg}$	width of the optical waveguide
$Z_0$	characteristic impedance of unloaded CPS
$Z_m$	characteristic impedance of the modulator
$Z_S$	source impedance, normally is 50 $\Omega$
$Z_T$	terminating impedance
$\Delta\lambda$	wavelength difference between two adjacent maximum points
$\Delta\phi$	phase difference

## List of Abbreviations

3-D	Three dimensional
ASE	Amplified spontaneous emission
BCB	Benzocyclobuten
BER	Bit error rate
CPS	Coplanar strips
CPW	Coplanar waveguides
C-V	Capacitance-Voltage
CW	Continuous wave
DWDM	Dense wavelength division multiplexing
EA	Electroabsorption
EAM	Electroabsorption modulator
ECL	External cavity laser
EDFA	Erbium-doped fiber amplifier
EM	Electromagnetic
EO	Electro-optic
ETDM	Electrical time division multiplexing
FEM	Finite element method
GPIO	General purpose interface bus
G-S	Ground signal
G-S-G	Ground signal ground
III-V	Semiconductor based on group III and group V elements
MBE	Molecular beam epitaxy
MMI	Multimode interference
MOCVD	Metal organic chemical vapor deposition
MQW	Multi quantum wells
MZI	Mach-Zehnder interferometer
MZM	Mach-Zehnder modulator
NLO	Nonlinear optical
NRZ	Non return to zero

PRBS	Pseudorandom binary sequence
QCSE	Quantum confined Stark effect
SEM	Scanning electron microscope
S-G	Signal ground
SOA	Semiconductor optical amplifier
SOLT	Short, open, load, thru
SSC	Spot-size converter
TDM	Time division multiplexing
TE	Transverse electric
TEM	Transverse electromagnetic
TLM	Transmission line method
TM	Transverse magnetic
TWE	Traveling-wave electrode
WDM	Wavelength division multiplexing



# Chapter 1

## Introduction

### 1.1 OVERVIEW

The use of light for communication purposes is not new. It can date back to antiquity if we interpret optical communications in a broad sense [1]. Most civilizations have used mirrors, fire beacons, or smoke signals to convey a single piece of information [2].

Development of fibers and devices for optical communication began in the early 1960s and continues strongly today. But the real change came in the 1980s. During this decade optical communication in public communication networks developed from the status of a curiosity into being the dominant technology. Transmitting signals by using light through optical fiber is the most effective way to move large amounts of data rapidly over long distances. Nowadays, in the era of information technology, the optical fiber transmission links form the backbone of the communications infrastructure. Recently, the bit rates of the electrical time-domain multiplexed (ETDM) system are improving from 2.5 Gbit/s to 10 Gbit/s and even 40 Gbit/s in deployed systems.

It is well known that the electrical signal still conquers our communication terminals in everyday life. But to take advantage of the optical transmission system, these electrical signals must be converted into optical ones which can be transferred in fibers. The electro-optic modulator (cf. Fig. 1.1) is such a device that converts the electrical signal to the optical one. For example, in a 40 Gbit/s electrical time-division multiplexing (ETDM) transmitter, low speed signals used in communication terminals will be hierarchically multiplexed into a high speed one (40 Gbit/s) at first, and then

the high speed electrical signal will be transformed into an optical signal which can be transferred in an optic fiber as shown in Fig. 1.1.

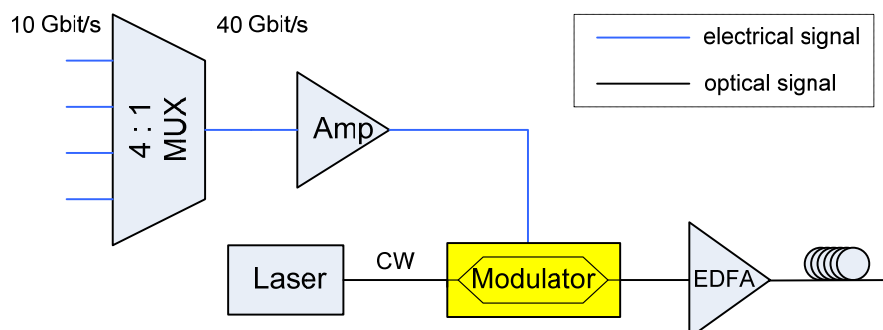


Fig. 1.1 A transmitter in a 40 Gbit/s ETDM system

In addition, high-bandwidth optical modulation has also applications in fiber-optic RF signal transmission and optoelectronic signal processing [3].

Lightwaves have various characteristics that can be modulated to carry information, including the intensity, phase, frequency and polarization. Among these, the intensity modulation is the most popular for optical fiber communication systems, primarily due to the simplicity of envelope photodetection. The modulator discussed in this work also uses intensity modulation.

## 1.2 ORGANIZATION OF THE DISSERTATION

This dissertation is organized as follows. In Chapter 1, different types of modulators are introduced and compared. The motivation of this work is presented at the end of the chapter.

In Chapter 2 the theoretical foundation of traveling-wave electrode electro-optic modulators is presented. Chapter 3 discusses the design consideration of the high-speed Mach-Zehnder modulator. Chapter 4 describes the electrical optimization to 80 Gbit/s including the simulations and experiments.

Chapter 5 explains the fabrication process and the involved packaging technology.

Chapter 6 introduces the corresponding measurements that are used for characterizing the modulators and test structures.

Chapter 7 shows experimental results and gives an overall summary and an outlook of further work.

### 1.3 DIRECT MODULATION

There are two groups of modulation methods: one is direct modulation, the other is external modulation. Each has its own pros and cons. They will be introduced in this and next section in detail.

The most straightforward method for modulation is to directly modulate the laser source. Due to the requirements of bandwidth and efficiency, only semiconductor lasers are of practical interest for direct modulation [4].

A unique feature of semiconductor lasers is that the semiconductor laser can be modulated directly by modulating the excitation current. As shown in Fig. 1.2 for a semiconductor laser, the output power of light intensity increases linearly with the injection current above threshold. For an injection current  $I = I_0 + i(t)$ , the optical output power is  $P(t) = P_0 + p(t)$ , where  $(I_0, P_0)$  is the bias point for the direct modulation of the semiconductor laser [5]. Using this feature, the direct modulation scheme can be configured as Fig. 1.3.

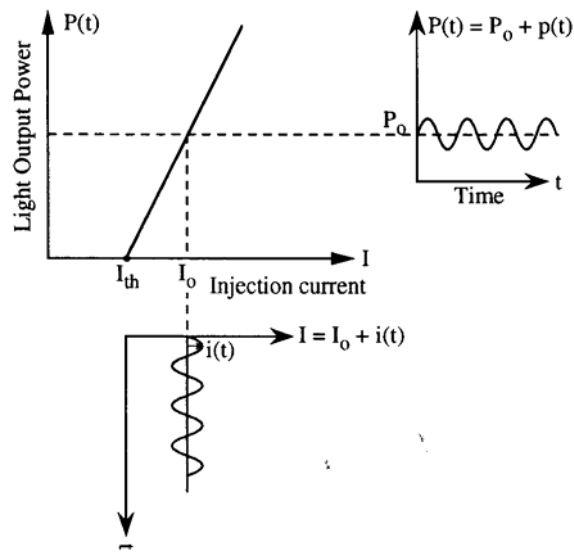


Fig. 1.2 Transition function of a current modulated semiconductor laser [2]

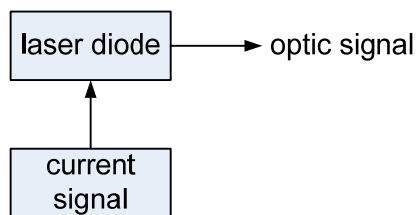


Fig. 1.3 Direct modulation scheme

Modulation bandwidths of 25 GHz and higher have been reported for semiconductor lasers operating at 1.55  $\mu\text{m}$  [5] and shorter wavelengths. The widest 3 dB bandwidth of a directly modulated laser reported to date is 37 GHz [6]. However, when the modulation frequency increases toward the relaxation resonance frequency of a semiconductor laser, both the relative intensity noise and distortions increase rapidly [7]. This severely limits the feasibility of direct modulation for a higher frequency. The large frequency chirp also precludes the direct modulation for long-distance communications systems (this will be explained in Chapter 2).

## 1.4 EXTERNAL MODULATORS

At bit rates of 10 Gbit/s or higher, the frequency chirp imposed by direct modulation becomes large enough that direct modulation of semiconductor laser is rarely used [2].

Unlike direct modulation, external modulation has been shown to have superior performance for wide bandwidth optical fiber communications, however with the potential disadvantages of adding system complexity and cost.

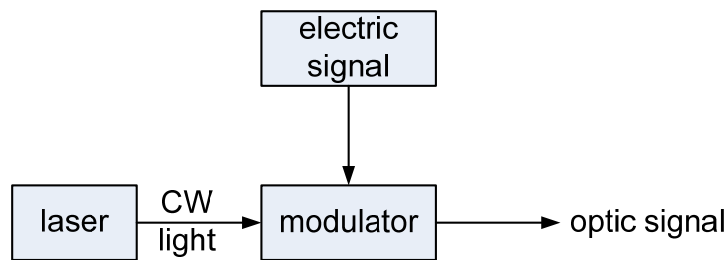


Fig. 1.4 External modulation scheme

As shown in Fig. 1.4 for a high-speed transmitter, the laser is biased at a constant current to provide the CW output, and an external optical modulator placed next to the laser converts the CW light into a data-coded pulse train with correct modulation format.

In the external modulation scheme, the light output passes through a material whose optical properties can be modified by an applied external electric field.

External optical modulators with bandwidths greater than 10 GHz are typically fabricated from the electro-optic crystal  $\text{LiNbO}_3$ , electro-optic polymers or III-V semiconductor compounds. Some of these devices have shown modulation frequencies in excess of 40 GHz.

According to the physical effects that are used in the respective modulator, these modulators can be grouped into two categories: one is the electro-optic (EO) modulator, the other is the electro-absorption (EA) modulator.

### 1.4.1 Electro-Optic Modulators

The electro-optic effect is most widely used for high speed modulation. Electro-optic modulators can produce amplitude, frequency or phase modulation in an optical signal by exploiting the electro-optic effect in which the optical properties of a crystal can be altered by an electric field.

Directional coupler and Mach-Zehnder interferometer are two waveguide structures that are often used for intensity modulation with the electro-optic effect.

#### 1.4.1.1 Directional coupler

A directional coupler consists of two side by side waveguides separated by a few micrometers (cf. Fig. 1.5). The overlap of guided waves in the two waveguides couples energy back and forth between the waveguides.

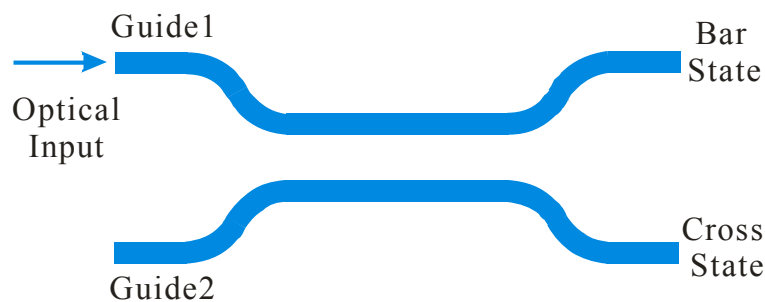


Fig. 1.5 Schematic of a directional coupler

When no voltage is applied, the two guides are phase-matched. The light input into guide 1 is nearly 100% coupled into guide 2 (cross-state) provided the coupler length is properly chosen.

When a voltage is applied, there is a change in the refractive index due to the applied electric field which can be made unequal in the two guides by implementing an appropriate design. This leads to a mismatch in the phase velocities in both guides and also to a reduction in coupling length. By adjusting the device parameters most of

the power can be transferred back to guide 1 (the bar-state) at the end of the directional coupler.

For directional coupler devices based on bulk material, the size of the device is fairly large since the electro-optic coefficient is not so large. Typically, the devices require an interaction length of  $\sim 1\text{cm}$  or more and a bias voltage of  $\sim 5\text{-}10\text{V}$ . The switching voltage of a directional coupler modulator is  $\sqrt{3}$  times larger than that required for a Mach-Zehnder modulator (see section 1.4.1.2). Due to these reasons, for digital applications the directional coupler structure is less been used than the Mach-Zehnder interferometer in intensity modulator design.

However, recent research shows that with multi-section design directional coupler based modulators have high linearity which is important for analog applications, such as RF-fiber links. Several corresponding designs have been published [12,13].

#### 1.4.1.2 Mach-Zehnder Interferometer

A Mach-Zehnder optical modulator uses an interferometric configuration of waveguides to enable the conversion of phase modulation into intensity modulation. Fig. 1.6 is a schematic drawing of such an interferometer. The optical wave enters from the left side and then splits equally into two beams by a splitter. The divided two beams propagate in two separate waveguides that are isolated from each other. The waveguides are often called “two arms”. At the end two beams are combined together.

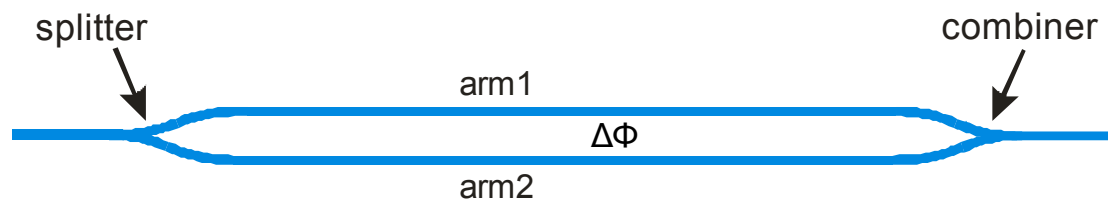


Fig. 1.6 Schematic of a Mach-Zehnder interferometer with 2 Y-branches

The splitter and combiner here can be a Y-branch, a directional coupler or a  $2 \times 2$  multimode interference (MMI) coupler.

A relative phase difference  $\Delta\phi$  is introduced between two arms. When the differential phase shift  $\Delta\phi$  between the two arms equals  $\pm\pi$ , destructive interference occurs, corresponding to the off-state or “0” level for the modulator. With no differential phase shift, constructive interference occurs, corresponding to the on-state or “1” level for the modulator.

Due to its simple structure and the potential of push-pull operation (further discussed in Chapter 3), the Mach-Zehnder interferometer (MZI) is the most popular device for implementing optical intensity modulation using the electro-optic effect. The modulators in this work are also based on the concept of the MZI.

### **1.4.1.3 Materials**

Many different materials can be used to fabricate electro-optic modulators, including lithium niobate, III-V compounds, polymers and even silicon. In this section, a brief introduction will be given for each material mentioned above.

#### **Lithium Niobate (LiNbO<sub>3</sub>)**

Lithium niobate (LiNbO<sub>3</sub>) is the most widely used material for the manufacture of electro-optic devices, including phase modulators, polarization modulators, Mach-Zehnder intensity modulators and directional-coupler intensity modulators.

LiNbO<sub>3</sub> is a ferroelectric anisotropic crystal with 3-m crystal symmetry. Depending on the orientation of an applied electric field, different electrooptic coefficients are relevant.

The most popular method of fabricating optical waveguides in LiNbO<sub>3</sub> is accomplished by diffusing titanium (Ti) which is deposited at the desired location of

the waveguide [8]. The dimensions of the optical waveguide can be controlled by properly choosing the initial Ti stripe width, film thickness and diffusion conditions. The resulting single-mode waveguide has a very low optical propagation loss, typically less than 0.2 dB/cm, and its mode size can be matched very well to that of a single-mode optical fiber.

Due to its properties of enabling low-loss waveguides, high electro-optic effect and high optical coupling efficiency with single-mode optical fiber, so far LiNbO<sub>3</sub> has been the material of choice for optical modulators at bit rates of 10 Gbit/s and above. LiNbO<sub>3</sub> travelling-wave modulators, based on a Mach-Zehnder interferometer waveguide structure, are the most widespread modulators in deployed systems [8].

However, LiNbO<sub>3</sub> Mach-Zehnder modulators have not only a large size, but also a bias-drifting problem which requires an extra bias control circuit. High driving voltage also limits their applications. In addition, the LiNbO<sub>3</sub> modulator is difficult to be integrated with other components

### **III-V Semiconductors**

III-V compound semiconductors, such as GaAs, InP and their ternary and quaternary alloys, are also candidate materials for EO modulators. There are two types of applications: one is using bulk material, the other is based on multi-quantum-wells (MQW).

Although their EO coefficients (defined in section 2.6) are 20 times smaller than that of LiNbO<sub>3</sub>, efficient modulation can still be obtained with these materials. This is because semiconductor crystal growth and fabrication techniques provide great flexibility for waveguide geometry control, so that the optical guided mode can be confined to a very small region (2-3  $\mu\text{m}$  spot size), and thus a very large electric field can be achieved even with a small voltage applied across the small dielectric gap. Additionally, III-V semiconductors have large optical refractive indices, for example, at optical wavelength of 1.3-1.6  $\mu\text{m}$ , the optical index is 3.2 for InP and 3.4 for GaAs,

compared to 2.2 for LiNbO<sub>3</sub>. This indicates a 3-4 times improvement for the index change in a linear electro-optic modulation application. All these factors make the efficiency of III-V EO modulators comparable to that of LiNbO<sub>3</sub> modulators. In addition, III-V EO modulators can potentially be integrated with a wide range of components such as lasers, semiconductor optical amplifiers (SOAs), photodetectors, passive optical circuits and even electronic drivers.

One popular type of III-V semiconductor EO modulator is based on bulk GaAs/AlGaAs waveguides grown on GaAs substrates due to the availability of large GaAs substrates (4" diameter), and those EO modulators are typically 2-3 cm long. In the GaAs/AlGaAs waveguide, the GaAs layer has higher optical index than the AlGaAs layer, the latter is lattice-matched to GaAs for all values. By sandwiching the GaAs layer between two AlGaAs layers, optical confinement in the vertical growth direction can be achieved. The lateral optical confinement is usually obtained by material etching. Shallow-etched rib waveguides are preferred over deep-ridge waveguides to achieve single-mode waveguiding. The resulting optical waveguides may have propagation loss ranging from tenths of dB/cm to a few dB/cm, depending on the waveguide structure and the fabrication process.

Another type of modulator, which is also made of III-V compound materials, uses the quantum confined Stark effect (QCSE) in multi-quantum-wells (MQW). Since strong index changes can be induced by QCSE (this will be discussed in detail in section 2.7), the relevant driving voltage for this type of device is relatively low compared to that of LiNbO<sub>3</sub> modulators. This is very attractive, because the lower the driving voltage is, the lower the power consumption, cost and size of the transmitter module become [9]. In addition, the compact size is also a notable advantage. The modulators in this work are also of this type.

## **Polymers**

Compared to  $\text{LiNbO}_3$  and III-V semiconductors, organic polymers are relatively immature EO materials, but they also possess a great potential for more advanced modulators. For example, a polymer modulator operating up to 150 GHz was reported in 2002 [10].

The advantages of EO polymers mostly come from the applicability of the spin-coating technique. This does not only make it possible to integrate polymer EO devices with various electronic and optoelectronic components [11], but also offers the opportunity to fabricate multiple devices stacked in the vertical direction. Metal electrodes can be buried between different polymer layers, and this makes the electrode design very flexible. To lower the fabrication cost, polymer EO devices can be fabricated directly on top of optical submounts. The optical refractive index of polymers is close to that of single-mode optical fibers. This provides a good match between the polymer waveguide mode and the fiber mode.

Polymer modulators may have great potential in the future, but their optical power handling capability is currently much less than that of modulators based of other materials, and their thermal and photochemical stabilities need to be improved.

## **Silicon**

Unlike the materials mentioned before, silicon as a ‘new’ material of optical components has been prompted on account of the demand for low-cost solutions from industry. There are also strong motivations for considering optics for shorter distance interconnects, especially using silicon photonic, a platform in which one could make electronics, waveguides, other optical components and optoelectronic devices.

Silicon is attractive from a cost standpoint because mature silicon processing technology and manufacturing infrastructure already exist and can be used to build cost-effective devices in large volume. In addition, silicon photonics technology

provides the possibility of monolithically integrating optical elements and advanced electronics on silicon using bipolar or CMOS technology [12].

Although unstrained pure crystalline silicon exhibits no linear electro-optic effect and the refractive index changes due to the Franz-Keldysh and Kerr effects are also small [13], several silicon waveguide-based optical modulators have been proposed and demonstrated [14,15] by using the free carrier plasma dispersion effect in a forward-biased pin diode geometry.

Since the modulation speed due to the free carrier plasma dispersion effect is determined by the rate at which carriers can be injected and removed, the long recombination carrier lifetime in the intrinsic silicon region generally limits the modulation frequency of these silicon-based devices.

A breakthrough was claimed by a group from Intel Corp. in 2004. They made a Si-based electro-optical modulator that can modulate light at 1~2 GHz, which is unprecedented in a silicon-based modulator, by introducing a metal-oxide-semiconductor (MOS) capacitor as phase shifter into the modulator structure [16]. Because charge transport in the MOS capacitor is governed by majority carriers, the device bandwidth is not limited by the relatively slow carrier recombination processes of pin diode devices. This group had optimized the device for a 10 Gbit/s application, recently [17].

Another breakthrough in silicon modulators was announced in 2005 by a team from Stanford University. They have reported that QCSE in thin germanium quantum-well structures grown on silicon has strengths comparable to that in III-V materials [18]. This discovery may be promising for small, high-speed, modulator devices fully compatible with silicon electronics manufacture.

Although there have been claimed breakthroughs in silicon-based modulator design, currently the modulation bandwidth and the power consumption of such devices is still not comparable with that of modulators based of other materials.

## 1.4.2 Electroabsorption Modulators

The electroabsorption (EA) effect denotes the change of the optical absorption coefficient in materials due to the presence of an electric field. The EA effect in a single optical waveguide directly results in optical intensity modulation. The primary materials for fabricating EAMs working at 1.3-1.6  $\mu\text{m}$  optical wavelengths are currently III-V semiconductors, specifically, ternary and quaternary alloys (including InGaAs, InAlAs, InAsP, InGaP, InGaAsP and InGaAlAs, etc.) grown on InP substrate. Similar to semiconductor-based EO modulators, EAMs can also be integrated with a variety of other devices. The most notable integrated chips include electroabsorption modulated lasers (EML) [19], and tandem EA modulators (often with SOA) for RZ data transmission and wavelength-division demultiplexing [20]. Another attraction of EAMs is their compact size (typically 80-300  $\mu\text{m}$  long) due to their high efficiency. This leads to small footprint for a single device and high yield per wafer which lowers the fabrication cost.

An EA waveguide usually consists of p-i-n semiconductor layers, among which the intrinsic layer has higher optical refractive index than the p-type and n-type doped layers. This provides vertical optical confinement. The lateral optical confinement is usually achieved by a deep mesa etch. The etched deep-ridge waveguide can then be planarized using polyimide or regrown semi-insulating InP. In a typical EA waveguide design, both the optical mode and the applied electric field are tightly confined in a small area around the intrinsic layer, which enables highly efficient modulation.

The optical propagation loss in EA waveguides is much larger than that in EO waveguides, typically ranging from 15 to 20 dB/mm. This high optical propagation loss is mainly attributed to three sources: the first is the residual absorption loss in the active layer; the second is the interband absorption loss induced by free carriers in the highly doped layers, primarily in p-type layers; the third is the scattering loss caused

by the roughness of the deep-ridge waveguide sidewalls and defects in the grown materials. Fortunately, due to their short length the overall optical loss is tolerable.

The tight optical confinement results in a small, elliptical mode profile in EA waveguides, typically 2-4  $\mu\text{m}$  lateral and 1-2  $\mu\text{m}$  vertical effective mode sizes which can have large optical coupling loss to a single-mode optical fiber whose mode size is typically 9  $\mu\text{m}$  in diameter. To overcome this problem, either a micro ball lens is inserted between the EA waveguide and the fiber tip, or an optical lens can be directly fabricated on the fiber tip to produce a mode size of 3-4  $\mu\text{m}$  at the focal plane that is 20  $\mu\text{m}$  away from the fiber tip. Integrating a spot-size converter (SSC) at both ends of the EA waveguide can further reduce the coupling loss. A SSC is a passive optical waveguide with adiabatic vertical and/or lateral tapers in geometry and/or optical refractive index. It converts the small elliptical EA waveguide mode at one end to a near-circular expanded mode (mode size 3-4  $\mu\text{m}$ ) at the other end, or vice versa. Integrating with a SSC makes the EAM longer, which makes cleaving and handling easier and also reduces the amount of unguided light directly coupled from the input fiber to the output fiber, resulting in an improved ON/OFF extinction ratio for digital links. Such SSC can be also used in a MQW based EO modulator.

Compared with EO modulators, the main disadvantages of EAM are low saturation power, large chirp, narrow optical bandwidth and need of temperature control. Nevertheless, EAMs are very attractive due to their small chip-size, low driving voltage and the compatibility for integration with other components. Limited by their inherent chirp, EAMs are not suitable for long-haul systems and are normally used in short distance transmission systems.

### 1.4.3 Comparison of Different Types of External Modulators

In the previous sections different types of modulators based of different materials have been briefly introduced. Table 1.1 gives a short summary of those modulators with a comparison of a few important characteristics.

Table 1.1: Comparison of several types of optical intensity modulators

TYPE	EO MZM			EAM	
MATERIAL	LiNbO <sub>3</sub>	III-V Compound		Polymer	InP
		bulk	MQW		
Optical loss	low	medium	medium	low	high
Driving voltage	high	medium	low	high	low
Chirp	Low	low	low	low	high
Footprint	big	big	small	big	small
Highest speed	50 GHz	40 GHz	57 GHz	110 GHz	50 GHz
Commercial use	yes	yes	yes	yes	yes
extra	Bias-control circuit	-	-	-	Temperature stabilizing unit

## 1.5 MOTIVATION FOR THE WORK

The rapid growth of data traffic, caused mainly by increasing use of the Internet including recent expanded use of multimedia services and wireless access, has stimulated the demand for high-capacity photonic network systems. High capacity optical networks are based on a combination of wavelength-division multiplexing (WDM) and time-division multiplexing (TDM) for purposes ranging from long-distance transmission between nodes to short-reach optical links such as metro/access links. Moreover, the next generation networks (NGN) are not far away from us and the 100 Gbit/s Ethernet is also in progress. All of these will inevitably need transmitters which can operate above 40 Gbit/s.

The maximum direct modulation bandwidth in semiconductor lasers is limited to a few GHz. The frequency chirp associated with high-speed direct modulation of laser diodes above a few Gbit/s has become a clear problem and results in serious consequences in high data rate long-distance optical-fiber transmission systems. The electro-optical modulator is the only choice for transmitters operating at bit rates beyond 10 Gbit/s in a long-haul transmission system.

Nowadays, electro-optical modulators have become the decisive components in the ETDM long-haul transmission system, whose data speed exceeds 40 Gbit/s. There is no such a product with corresponding speed in the market. Although there are reports about 80 Gbit/s or 100 Gbit/s ETDM transmitter systems [21,22], the modulators used in those systems are still 40 Gbit/s ones, but not 80 Gbit/s or 100 Gbit/s ones. This largely restricts the performance of the whole system. The aim of this work is to develop an electro-optical modulator enabling operation well above 40 Gbit/s in order to improve the performance of the corresponding ETDM system.

Moreover, high speed modulation of optical waves is also of great interest for radar, satellite links and electronic warfare systems.

As mentioned in section 1.4, the InP-based MQW Mach-Zehnder modulator has compact size, low driving voltage, zero or controllable chirp and the compatibility for integration with other components. In addition, it is also suitable for advanced modulation formats such as CS-RZ [23] and RZ-DPSK [24] for example. Its optical insertion loss could also be reduced to a level comparable to that in LiNbO<sub>3</sub>-based modulators. All these properties make it attractive for modulation rates well above 40 Gbit/s.

The modulator research group in the Fraunhofer-Institute for Telecommunications Heinrich-Hertz-Institut has many years of research experience in InP-based MQW Mach-Zehnder modulators. The electro-optical response of a modulator of a preliminary version had achieved 20 GHz (cf. Fig. 1.7) and served as a basis for further development. This work focuses on optimizing the electrical design of the developed modulators and making them work up to 80 Gbit/s.

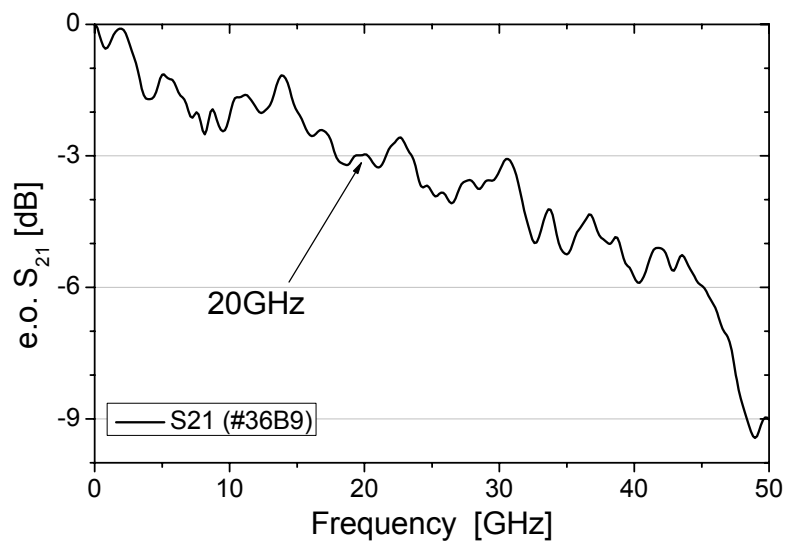


Fig. 1.7 Measured electro-optical response of a modulator

## REFERENCES

- [1] G. J. Holzmann and B. Pehrson, "The early history of data networks", IEEE computer society press, Los Alamos, CA (1995)
- [2] G. P. Agrawal, "Fiber-optic communication systems", 3<sup>rd</sup> Ed., Wiley, New York (2002)
- [3] R.G. Walker, "Low-voltage, 50  $\Omega$ , GaAs/AlGaAs travelling-wave modulator with bandwidth exceeding 25 GHz", *Electron. Lett.* **25**, 1549-1550 (1989).
- [4] S. L. Chuang, "Physics of Optoelectronic Devices", Wiley, 487-488 (1995)
- [5] P. A. Morton, R. A. Logan, T. Tanbun-Ek, P. F. Sciortino, Jr, A. M. Sergent, R. K. Montgomery, and B. T. Lee, "25 GHz bandwidth 1.55  $\mu\text{m}$  GaInAsP p-doped strained multiquantum well lasers," *Electron. Lett.* **28**, 2156–2157 (1992).
- [6] S. Weiser, E. C. Larkins, K. Czotscher, w. Benz, J. Daleiden, J. Fleissner, M. Maier, J. D. Ralston, B. Romero, A. Schonfelder and J. Rosenzweig, "37 GHz direct modulation bandwidth in short-cavity InGaAs/GaAs MQW lasers with C-doped active regions," paper SCL1.1, IEEE Lasers and Electro-Optic Society Annual Meeting, San Jose, CA, Oct. 30- Nov. 2, (1995)
- [7] N. K. Dutta, N. A. Olsson, L. A. Koszi, P. Besomi, R. B. Wilson, and R. J. Nelson, "Frequency chirp under current modulation in InGaAsP injection lasers," *J. Appl. Phys.* **56**, 2167-2169 (1984).
- [8] K. Noguchi, O. Mitomi, and H. Miyazawa, "Millimeter-Wave Ti:LiNbO<sub>3</sub> Optical Modulators," *IEEE J. Lightwave Technology*, **16**, 615-619 (1998)
- [9] T. Yamannka, "High-performance InP-based optical modulators", OWC1, OFC2006
- [10] M. Lee, H. E. Katz, C. E. D. M. Gill, P. Gopalan, J. D. Heber and D. J. McGee, "Broadband Modulation of light by using an electro-optic polymer," *Science*, **298**, 1401-1403 (2002)
- [11] S. Kalluri, M. Ziari, A. Chen, V. Chuyanov, W. H. Steier, D. Chen, B. Jalali, H. Fetterman, and L. R. Dalton, "Monolithic integration of waveguide polymer electrooptic modulators on VLSI circuitry," *IEEE Photon. Technol. Lett.* **8**, 644-646 (1996)
- [12] R. A. Soref, "Silicon-based optoelectronics," *Proc. IEEE* **81**, 1687-1706 (1993)
- [13] R. A. Soref and B. R. Bennett, "Electro optical effects in silicon," *IEEE J. Quantum Electron*, **QE-23**, 123-129 (1987)
- [14] C. K. Tang and G. T. Reed, "Highly efficient optical phase modulator in SOI waveguides," *Electron. Lett.* **31**, 451-452 (1995)

- [15] P. Dainesi, "CMOS compatible fully integrated Mach-Zehnder interferometer in SOI technology," *IEEE Photon. Technol. Lett.* **12**, 660-662 (2000)
- [16] A. Liu, R. Jones, L. Liao, D. Samara-Rubio, D. Rubin, O. Cohen, R. Nicolaescu, and M. Paniccia, "A high-speed silicon optical modulator based on a metal-oxide-semiconductor capacitor," *Nature* **427**, 615-618 (2004)
- [17] L. Liao, "High-speed silicon Mach-Zehnder modulator," *Opt. Express* **13**, 3129 (2005)
- [18] Y. Kuo, Y. Lee, Y. Ge, S. Ren, J. E. Roth, T. I. Kamins, D. A. B. Miller, and J. S. Harris, "Strong quantum-confined Stark effect in germanium quantum-well structures on silicon," *Nature* **437**, 1334-1336 (2005)
- [19] K. Wakita, I. Kotaka, H. Asai, M. Okamoto, Y. Kondo, and M. Naganuma, "High-speed and low-drive voltage monolithic multiple quantum-well modulator/DFB laser light source," *IEEE Photon. Technol. Lett.* **4**, 16-18, (1992)
- [20] N. Souli, A. Ramdane, F. Devaux, A. Ougazzaden, and S. Slemkes, "Tandem of electroabsorption modulators integrated with distributed feedback laser and optical amplifier for 20-Gbit/s pulse generation and coding at 1.5  $\mu\text{m}$ ," in *Proc. OFC'97 Tech. Dig. (Optical Fiber Communication)*, **6**, paper WG6, 141-142 (1997)
- [21] K. Schuh, "85.4Gbit/s ETDM transmission over 401 km SSMF applying UFEC", *ECOC2005 Th4.1.4*, (2005)
- [22] Peter J. Winzer, "107Gb/s optical ETDM transmitter for 100 G Ethernet transport", *ECOC2005 Th4.1.1*, (2005)
- [23] Y. Miyamoto, "320 Gbit/s (8x40 Gbit/s) WDM transmission over 367 km with 120 km repeater spacing using carrier-suppressed return-to-zero format," *Electronics Lett.* **35**, 2041-2042 (1999)
- [24] A. H. Gnauck, "2.5 Tb/s (64x42.7 Gbit/s) transmission over 40x100 km NZDSF using RZ-DPSK format and all-Raman-amplified spans," in *Technical Digest of Optical Fiber Communication Conference (OFC2002)* , Post-deadline paper, FC2 (2002).



## Chapter 2

### Basic Theory

The traveling-wave electrode Mach-Zehnder modulator is an electro-optic device. To design and optimize such a device, it involves the knowledge of semiconductor, high frequency microwave, and electro-optical effects. All of these will be introduced briefly in this chapter.

#### 2.1 COPLANAR LINES

The term coplanar lines is used for those transmission lines where all the conductors are in the same plane, namely on the top of the dielectric substrate. Coplanar waveguide (CPW) (cf. Fig. 2.1a) and coplanar strips (CPS) (cf. Fig. 2.2a) are coplanar lines [1]. A distinct advantage of these two types of transmission line lies in the fact that mounting lumped components in shunt or series configuration is much easier. Drilling holes or slots through the substrates is not needed.

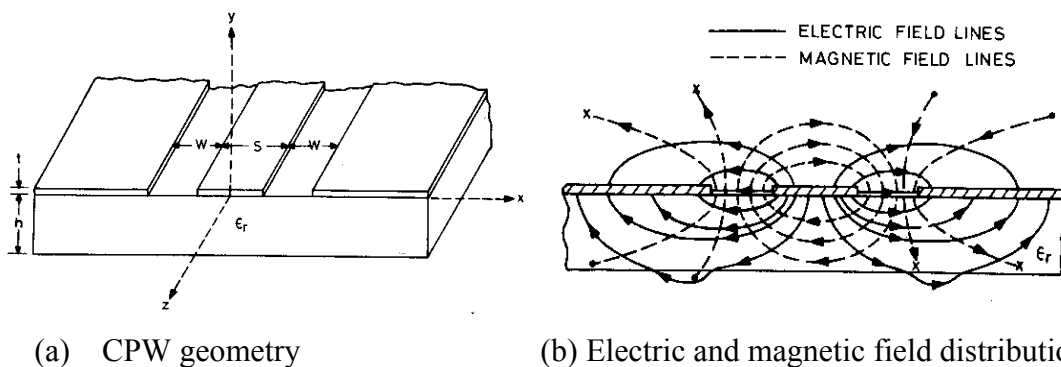


Fig. 2.1 CPW geometry and corresponding electric and magnetic field distribution [1]

As shown in Fig. 2.1(a), CPW consists of two slots each of width  $w$  printed on a dielectric substrate. The spacing between the slots is denoted by  $s$ . The electric and magnetic field configurations for quasi-static approximation are shown in Fig. 2.1(b).

The configuration of CPS, which is complementary to the CPW, is shown in Fig. 2.2(a). CPS consists of two strips, generally of equal width  $w$  on a dielectric substrate. The spacing between the strips is denoted by  $s$ . The electric and magnetic field configurations are shown in Fig. 2.2(b).

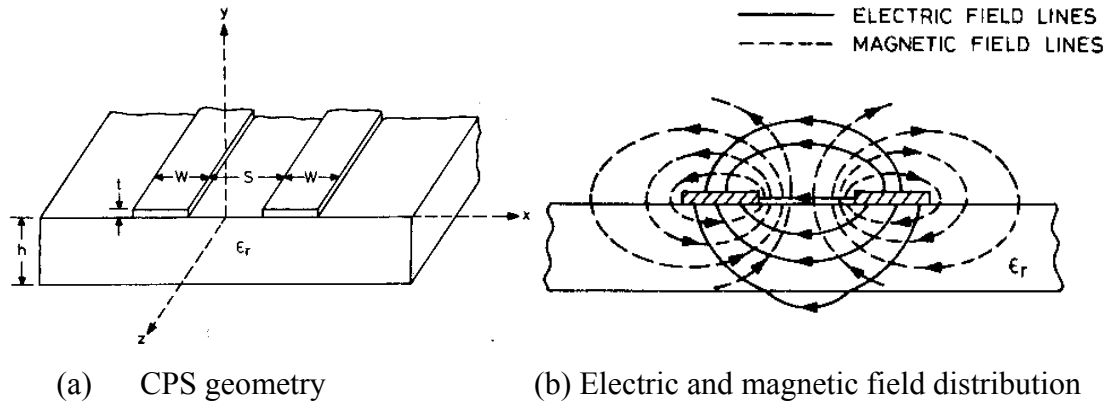


Fig. 2.2 CPS geometry and corresponding electric and magnetic field distribution [1]

Sometimes, it is also desirable to use an asymmetric CPS (cf. Fig. 2.3) to adjust the characteristic impedance by changing the width of one of the strips while keeping the width of the other strip and the slot width fixed.

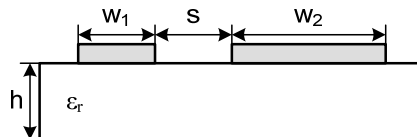


Fig. 2.3 Asymmetric CPS

CPW and CPS support quasi-TEM modes and have been analysed using quasi-static as well as full-wave methods. Expressions for characteristic impedance  $Z_0$  and effective dielectric constant  $\epsilon_{r\text{eff}}$  of CPW, CPS and asymmetric CPS are given in table 2.1.

Table 2.1 Expressions for coplanar lines characteristic impedance and effective dielectric constant [1]

Structure	Characteristic Impedance ( $\Omega$ )	Effective dielectric constant
CPW	$Z_0 = \frac{30\pi}{\sqrt{\epsilon_{reff}}} \frac{K'(k)}{K(k)}$	$\epsilon_{reff} = 1 + \frac{\epsilon_r - 1}{2} \frac{K'(k)K(k_1)}{K(k)K'(k_1)}$  $k = \frac{a}{b}$ , $a = \frac{s}{2}$ , $b = \frac{s}{2} + w$  $k_1 = \frac{\sinh(\frac{\pi a}{2h})}{\sinh(\frac{\pi b}{2h})}$
CPS	$Z_0 = \frac{120\pi}{\sqrt{\epsilon_{reff}}} \frac{K(k)}{K'(k)}$	
Asymmetric CPS	$Z_0 = \frac{60\pi}{\sqrt{\epsilon_{reff}}} \frac{K(k_2)}{K'(k_2)}$	$k_2 = \sqrt{1 - \frac{w_1}{s+w_1} \frac{w_2}{s+w_2}}$  $w_1$ and $w_2$ are the strips' width

The  $K(k)$  in table 2.1 represents a complete elliptic function of the first kind and is defined as

$$K(k) = \int_0^{\frac{\pi}{2}} \frac{d\varphi}{\sqrt{1 - k^2 \cdot \sin^2 \varphi}} \quad (2.1.1)$$

$K'(k)$  is its complementary function and can be calculated by

$$K(k)^2 + K'(k)^2 = 1 \quad (2.1.2)$$

Expression (2.1.3) [2] is an accurate and simple approximation of  $\frac{K(k)}{K'(k)}$

and has only a relative error lower than  $3 \times 10^{-6}$ :

$$\frac{K(k)}{K'(k)} \approx \frac{\pi}{\ln\left(2 \cdot \frac{1 + \sqrt{k'}}{1 - \sqrt{k'}}\right)} \quad \text{for } 0 \leq k \leq \frac{\sqrt{2}}{2}$$

$$\frac{K(k)}{K'(k)} \approx \frac{1}{\pi} \cdot \ln\left(2 \cdot \frac{1 + \sqrt{k}}{1 - \sqrt{k}}\right) \quad \text{for } \frac{\sqrt{2}}{2} \leq k \leq 1 \quad (2.1.3)$$

with  $k^2 + k'^2 = 1$

As an example, Fig. 2.4 shows a calculated characteristic impedance curve of the CPS using semi-isolating InP as the substrate.

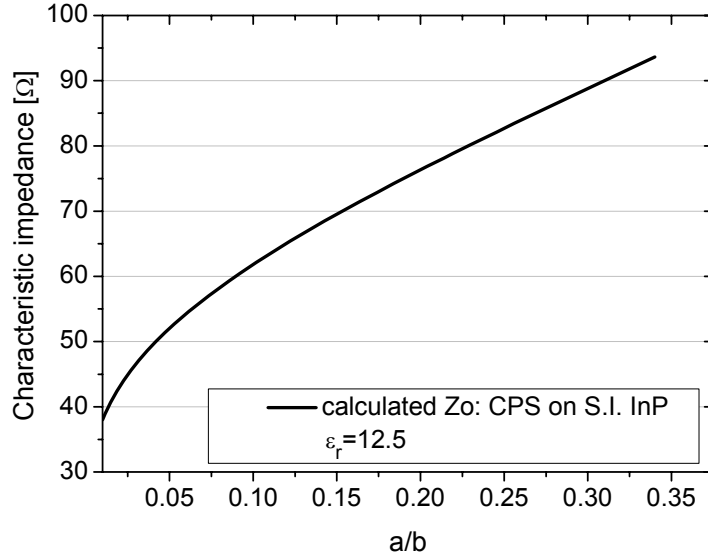


Fig. 2.4 Calculated characteristic impedance as function of different geometry parameters of CPS using semi-isolating InP as substrate ( $a$ ,  $b$  defined in table 2.1)

The coplanar lines have three types of losses: dielectric, Ohmic and radiation/surface wave. The expression for the attenuation constant due to dielectric loss in CPS is [1]

$$\alpha_d = 27.3 \cdot \frac{\epsilon_r}{\sqrt{\epsilon_{reff}}} \cdot \frac{\epsilon_{reff} - 1}{\epsilon_r - 1} \cdot \frac{\tan \delta}{\lambda_0} \text{ dB/unit length} \quad (2.1.4)$$

Here  $\lambda_0$  is the wavelength in free space,  $\tan \delta$  is the dielectric loss tangent of the substrate material.

The Ohmic loss (also called conductor loss) of coplanar lines is given as [1]

$$\alpha_c = \frac{8.68 R_s \sqrt{\epsilon_{reff}}}{480 \pi K(k_1) K'(k_1) (1 - k_1^2)} \left\{ \frac{1}{a} \left[ \pi + \ln \left( \frac{8 \pi a (1 - k_1)}{t (1 + k_1)} \right) \right] + \frac{1}{b} \left[ \pi + \ln \left( \frac{8 \pi b (1 - k_1)}{t (1 + k_1)} \right) \right] \right\} \quad (2.1.5)$$

with unit of dB/unit length. Here  $a$ ,  $b$ ,  $\epsilon_{reff}$ ,  $k$  and  $k_1$  are defined in table 2.1, series expansions for  $K(k)$ , needed for the evaluation of (2.1.5) are given as [3]

for  $0 \leq k \leq 0.707$

$$K(k) = \frac{\pi}{2} \left\{ 1 + 2 \left( \frac{k^2}{8} \right) + 9 \left( \frac{k^2}{8} \right)^2 + 50 \left( \frac{k^2}{8} \right)^3 + 306.25 \left( \frac{k^2}{8} \right)^4 + \dots \right\}$$

for  $0.707 \leq k \leq 1$

(2.1.6)

$$K(k) = p + (p-1) \left( \frac{k'}{2} \right)^2 + \frac{9}{4} \left( p - \frac{7}{6} \right) \left( \frac{k'}{2} \right)^4 + \frac{25}{4} \left( p - \frac{37}{30} \right) \left( \frac{k'}{2} \right)^6 + \dots$$

where  $p = \ln \left( \frac{4}{k'} \right)$

In addition to the dielectric and Ohmic losses, coupling of power to surface waves and radiation from unwanted (parasitic) modes also contribute to the total loss of coplanar lines. Coplanar lines with finite thickness substrate can also be leaky. However, if the substrate thickness  $h$  according to [4]

$$h < \frac{0.12 \cdot \lambda_0}{\sqrt{\epsilon_r}} \quad (2.1.7)$$

power leakage can be avoided since the cutoff frequency of the surface modes is pushed above the operating frequency. That is, for InP substrate and work frequency of 40 GHz, the substrate thickness  $h$  should be smaller than 255  $\mu\text{m}$ .

## 2.2 TRANSMISSION LINE THEORY

At frequencies where the wavelength is several orders of magnitude larger than the greatest dimensions of the circuit or system being examined, conventional circuit elements such as capacitors, inductors, resistors and transistors are the basic building blocks for the circuits or systems. The description or analysis of such circuits may be adequately carried out in terms of loop currents and node voltages without consideration of propagation effects. However, as the frequency is raised to a point where the wavelength is no longer large compared to the circuit dimensions, propagation effects can no longer be ignored [5]. This problem can be solved by using

transmission line theory. On the other hand, coplanar lines are also transmission lines. Hence, the transmission line theory is the basis for analyzing the high-speed traveling-wave modulator.

### 2.2.1 The Lumped-element Circuit Model of Transmission Line

A unique property of the transmission line is that a satisfactory analysis of its properties may be carried out by treating it as a network with distributed parameters and solving for the voltage and current waves that may propagate along the line. As shown in Fig. 2.5(a), a transmission line is often schematically represented as a two-wire line since transmission lines always have at least two conductors. The short piece of line of length  $\Delta z$  of Fig. 2.5(a) can be modeled as a lumped-element circuit, as shown in Fig. 2.5(b), where  $R_0$ ,  $L_0$ ,  $G_0$ ,  $C_0$  are per unit length quantities of series resistance, series inductance, shunt conductance and shunt capacitance, respectively.

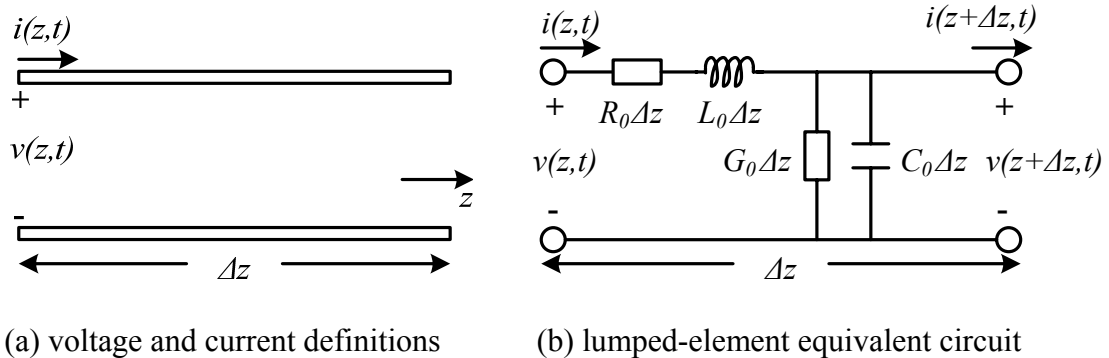


Fig. 2.5 Voltage and current definitions and equivalent circuit for an incremental length of transmission line

The series inductance  $L_0$  represents the total self-inductance of the two conductors, and the shunt capacitance  $C_0$  is due to the close proximity of the two conductors. The series resistance  $R_0$  represents the resistance due to the finite conductivity of the conductors, and the shunt conductance  $G_0$  is due to the dielectric loss in the material between the conductors.  $R_0$  and  $G_0$ , therefore, represent loss. A finite length of transmission line can be viewed as a cascade of sections of the form of Fig. 2.5(b).

According to Kirchoff's law and letting  $\Delta z \rightarrow 0$ , we can get the following relationships

$$\frac{dV(z)}{dz} = -(R_0 + j\omega L_0)I(z) \quad (2.2.1)$$

$$\frac{dI(z)}{dz} = -(G_0 + j\omega C_0)V(z) \quad (2.2.2)$$

with

$$v(z, t) = V(z)e^{j\omega t} \quad (2.2.3)$$

$$i(z, t) = I(z)e^{j\omega t} \quad (2.2.4)$$

### 2.2.2 Propagation Parameters of the Transmission Line

The propagation equations of a transmission line can be obtained from (2.2.1) and (2.2.2):

$$\frac{d^2V}{dz^2} = \gamma^2 V \quad (2.2.5)$$

$$\frac{d^2I}{dz^2} = \gamma^2 I \quad (2.2.6)$$

with the complex transmission constant  $\gamma$  given by

$$\gamma = \sqrt{(R_0 + j\omega L_0)(G_0 + j\omega C_0)} = \alpha + j\beta \quad (2.2.7)$$

Traveling-wave solutions for (2.2.5) and (2.2.6) are

$$V = V_{0+}e^{-\gamma z} + V_{0-}e^{\gamma z} \quad (2.2.8)$$

$$I = I_{0+}e^{-\gamma z} + I_{0-}e^{\gamma z} \quad (2.2.9)$$

where the  $e^{-\gamma z}$  term represents wave propagation in the  $+z$  direction, and the  $e^{\gamma z}$  term represents wave propagation in the  $-z$  direction,  $V_{0\pm}$  and  $I_{0\pm}$  are constants that should be defined by the boundary conditions.

The phase velocity is given by

$$v_p = \frac{\omega}{\beta} \quad (2.2.10)$$

The characteristic impedance  $Z_0$  of the transmission line can be defined as [5]

$$Z_0 = \sqrt{\frac{R_0 + j\omega L_0}{G_0 + j\omega C_0}} \quad (2.2.11)$$

As shown in Fig. 2.6, the transmission line with characteristic impedance  $Z_0$ , propagation constant  $\gamma$ , and length  $l$  can be described as a two-port network. The transmission matrix (also called ABCD matrix, definition in Appendix A) of this two-port network is [6]

$$\begin{bmatrix} A & B \\ C & D \end{bmatrix} = \begin{bmatrix} \cosh(\gamma l) & Z_0 \sinh(\gamma l) \\ \frac{1}{Z_0} \sinh(\gamma l) & \cosh(\gamma l) \end{bmatrix} \quad (2.2.12)$$

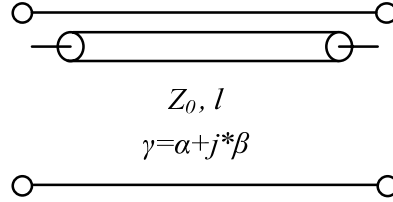


Fig. 2.6 A two-port network model for the transmission line

One can get the transmission matrix by converting the measured scattering matrix as follows [6]

$$\begin{bmatrix} A & B \\ C & D \end{bmatrix} = \begin{bmatrix} \frac{(1 + S_{11})(1 - S_{22}) + S_{12}S_{21}}{2S_{21}} & Z_r \frac{(1 + S_{11})(1 + S_{22}) - S_{12}S_{21}}{2S_{21}} \\ \frac{1}{Z_r} \frac{(1 - S_{11})(1 - S_{22}) - S_{12}S_{21}}{2S_{21}} & \frac{(1 - S_{11})(1 + S_{22}) + S_{12}S_{21}}{2S_{21}} \end{bmatrix} \quad (2.2.13)$$

here  $Z_r$  is the reference impedance used in the measurement and is normally equal to  $50 \Omega$ .

The propagation parameter  $\gamma$  and the characteristic impedance  $Z_0$  can be calculated from (2.2.12):

$$\gamma = \frac{\ln\left(\frac{A+D}{2} + \sqrt{BC}\right)}{l} \quad (2.2.14)$$

$$Z_0 = \sqrt{\frac{B}{C}} \quad (2.2.15)$$

From (2.2.7) and (2.2.11), the  $R_0$ ,  $L_0$ ,  $G_0$ ,  $C_0$  can be calculated by (2.2.16) using the propagation parameter  $\gamma$  and characteristic impedance  $Z_0$ , respectively.

$$\begin{aligned} L_0 &= \frac{\text{Im}(\gamma \cdot Z_0)}{\omega} & R_0 &= \text{Re}(\gamma \cdot Z_0) \\ C_0 &= -\frac{\text{Im}(\frac{\gamma}{Z_0})}{\omega} & G_0 &= \text{Re}(\frac{\gamma}{Z_0}) \end{aligned} \quad (2.2.16)$$

### 2.2.3 Analysis of the Periodically Loaded Transmission Line

The periodically loaded transmission line (cf. Fig 2.7) may have a lower phase velocity than the smooth transmission line. This property is used as a slow-wave property in modulator design.

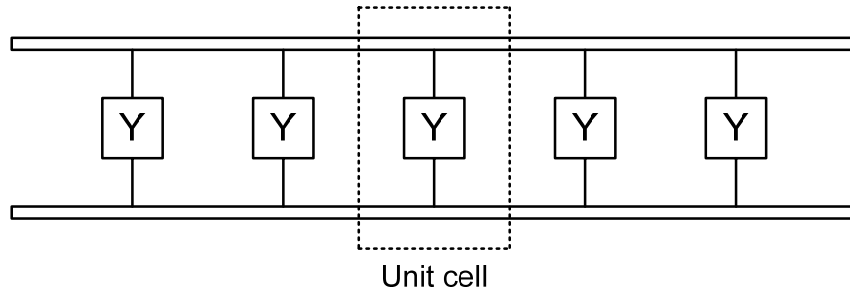


Fig. 2.7 A periodically loaded transmission line

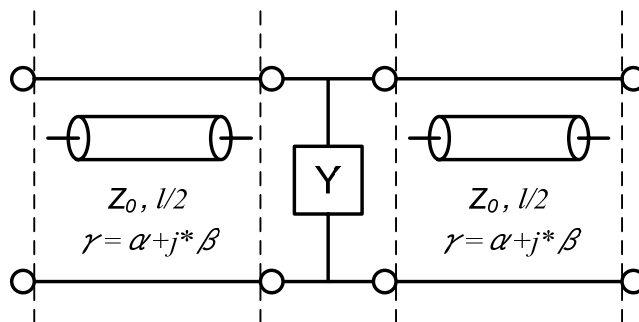


Fig. 2.8 Equivalent circuit of a unit cell in Fig. 2.7, uniform transmission line with shunt element in center

The transmission matrix for a unit cell as Fig. 2.8 can be described as:

$$\begin{bmatrix} A_0 & B_0 \\ C_0 & D_0 \end{bmatrix} = \begin{bmatrix} \cosh\left(\frac{\gamma l}{2}\right) & Z_0 \sinh\left(\frac{\gamma l}{2}\right) \\ \frac{1}{Z_0} \sinh\left(\frac{\gamma l}{2}\right) & \cosh\left(\frac{\gamma l}{2}\right) \end{bmatrix} \cdot \begin{bmatrix} 1 & 0 \\ Y & 1 \end{bmatrix} \cdot \begin{bmatrix} \cosh\left(\frac{\gamma l}{2}\right) & Z_0 \sinh\left(\frac{\gamma l}{2}\right) \\ \frac{1}{Z_0} \sinh\left(\frac{\gamma l}{2}\right) & \cosh\left(\frac{\gamma l}{2}\right) \end{bmatrix} \quad (2.2.17)$$

Multiplication of the matrices and use of identities for hyperbolic functions gives [7]

$$\begin{aligned} A_0 &= D_0 = \cosh(\gamma l) + \frac{YZ_0}{2} \cdot \sinh(\gamma l) \\ B_0 &= Z_0 \cdot \left[ \frac{YZ_0}{2} \cdot (-1 + \cosh(\gamma l)) + \sinh(\gamma l) \right] \\ C_0 &= \frac{1}{Z_0} \cdot \left[ \frac{YZ_0}{2} \cdot (1 + \cosh(\gamma l)) + \sinh(\gamma l) \right] \end{aligned} \quad (2.2.18)$$

Note that the unit cell is symmetric ( $A_0 = D_0$ ) and reciprocal ( $A_0 D_0 - B_0 C_0 = 1$ ).

The overall transfer matrix for  $N$  like networks is just the  $N^{\text{th}}$  power of that for a single network:

$$\begin{bmatrix} A & B \\ C & D \end{bmatrix} = \begin{bmatrix} A_0 & B_0 \\ C_0 & D_0 \end{bmatrix}^N \quad (2.2.19)$$

For a network with reciprocity, this results in [7]

$$\begin{bmatrix} A & B \\ C & D \end{bmatrix} = \begin{bmatrix} \frac{A_0 \cdot \sinh N\Gamma - \sinh(N-1)\Gamma}{\sinh \Gamma} & B_0 \cdot \frac{\sinh N\Gamma}{\sinh \Gamma} \\ C_0 \cdot \frac{\sinh N\Gamma}{\sinh \Gamma} & \frac{D_0 \cdot \sinh N\Gamma - \sinh(N-1)\Gamma}{\sinh \Gamma} \end{bmatrix} \quad (2.2.20)$$

$$\text{with } \cosh \Gamma = \frac{A_0 + D_0}{2}$$

Because of the unit cell's symmetry and reciprocity, the matrix of whole network can be simplified as [7]

$$\begin{bmatrix} A & B \\ C & D \end{bmatrix} = \begin{bmatrix} \cosh N\Gamma & \sqrt{\frac{B_0}{C_0}} \sinh N\Gamma \\ \sqrt{\frac{C_0}{B_0}} \sinh N\Gamma & \cosh N\Gamma \end{bmatrix} \quad (2.2.21)$$

$$\text{with } \cosh \Gamma = A_0$$

### 2.3 III-V COMPOUND MATERIAL

Almost any semiconductor with a direct bandgap can be used to make a p-n homojunction capable of emitting or absorbing light. The choice is, however, considerably limited in the case of hetero-structure devices because their performance depends on the quality of the hetero-junction interface between two semiconductors of different bandgaps. To reduce the formation of lattice defects, the lattice constant of the two materials should match to better than 0.1%. Such semiconductors can be fabricated artificially by forming ternary or quaternary compounds in which a fraction of the lattice sites in a naturally occurring binary semiconductor is replaced by other elements.

As discussed before, it is beneficial to operate lightwave systems in the wavelength range 1.3-1.6  $\mu\text{m}$ , where both dispersion and loss of optical fibers are considerably reduced compared to the 0.85  $\mu\text{m}$  region. InP is the base material for semiconductor optical sources emitting light in this wavelength region. As seen in Fig. 2.9 by the horizontal line passing through InP, the bandgap of InP can be reduced by making the quaternary compound  $\text{In}_{1-x}\text{Ga}_x\text{As}_y\text{P}_{1-y}$  while the lattice constant 'a' remains matched to InP ( $a = 5.87\text{\AA}$ ). The fractions x and y cannot be chosen arbitrarily but are related by [8]

$$x(y) = \frac{0.19y}{0.417 - 0.012y} \quad (2.3.1)$$

to ensure matching of the lattice constant. The bandgap of the quaternary compound can be expressed in terms of y only and is well approximated by [9]

$$E_g(y) = 1.35 - 0.72y + 0.12y^2 \quad (0 \leq y \leq 1) \quad (2.3.2)$$

here  $E_g$  is expressed in electron-volt (eV) units.

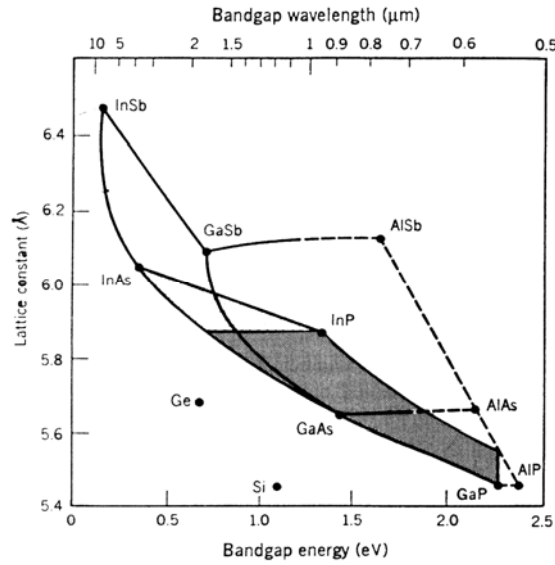


Fig. 2.9 Lattice constant and bandgap energies of ternary and quaternary compounds formed by using III-V group semiconductors [10]

The wavelength of the emitted light is determined by the bandgap since the photon energy is approximately equal to the bandgap energy. The corresponding light wavelength,  $\lambda$ , can be obtained using [10]

$$E_g \approx h\nu = \frac{hc}{\lambda} \quad (2.3.3)$$

where  $h$  is the Planck constant,  $\nu$  is the frequency of the photon and  $c$  is the speed of light in free space. If  $E_g$  is expressed in eV, the light wavelength in microns ( $\mu\text{m}$ ) is given by [10]

$$\lambda = \frac{1.24}{E_g} \quad (2.3.4)$$

The smallest bandgap of  $\text{In}_{1-x}\text{Ga}_x\text{As}_y\text{P}_{1-y}$  occurs for  $y=1$ . The corresponding ternary compound  $\text{In}_{0.54}\text{Ga}_{0.46}\text{As}$  emits light near  $1.65 \mu\text{m}$  ( $E_g=0.75\text{eV}$ ). By a suitable choice of the mixing fractions  $x$  and  $y$ ,  $\text{In}_{1-x}\text{Ga}_x\text{As}_y\text{P}_{1-y}$  sources can be designed to operate in the wide wavelength range  $1.0\text{-}1.65 \mu\text{m}$  that includes the region  $1.3\text{-}1.6\mu\text{m}$ , which is important for optical communication systems.

## 2.4 P-I-N DIODE

In a modulator, it is the reverse biased p-i-n diode that provides the electrical field which is used to change the optical refractive index in an optical waveguide of the modulator.

A p-i-n junction is similar to a p-n junction, but contains in addition an intrinsic or un-intentionally doped region between the  $n$ -type and  $p$ -type layer. Its analysis is similar to that of a p-n diode. Hence we start this section with p-n junction.

### 2.4.1 p-n Junction

A p-n junction is composed of a doped  $p$ -type semiconductor with an acceptor density  $N_A$  on one side of a junction and a doped  $n$ -type semiconductor with a donor density  $N_D$  on the other.

At thermal equilibrium, no external voltage is applied between the  $n$ - and  $p$ -type material, there is an internal potential,  $\phi_i$ , which is also called as the built-in potential. It is caused by the workfunction difference between the  $n$ - and  $p$ -type semiconductors. The built-in potential,  $\phi_i$ , is defined as [11]

$$\phi_i = \frac{kT}{q} \ln \frac{N_A N_D}{n_i^2} \quad (2.4.1)$$

where  $n_i$  represents the intrinsic density.

We now consider a p-n diode with an applied bias voltage,  $V_a$ . A forward bias corresponds to applying a positive voltage to the anode (the  $p$ -type region) relative to the cathode (the  $n$ -type region). A reverse bias corresponds to a negative voltage applied to the anode. Both bias modes are illustrated with Fig. 2.10. The applied voltage is proportional to the difference between the Fermi energy in the  $n$ -type and  $p$ -type quasi-neutral regions.

As a negative voltage is applied, the potential across the semiconductor increases and so does the depletion layer width. As a positive voltage is applied, the potential across the semiconductor decreases and with it the depletion layer width. The

total potential across the semiconductor equals the built-in potential minus the applied voltage, or:

$$\phi = \phi_i - V_a \quad (2.4.2)$$

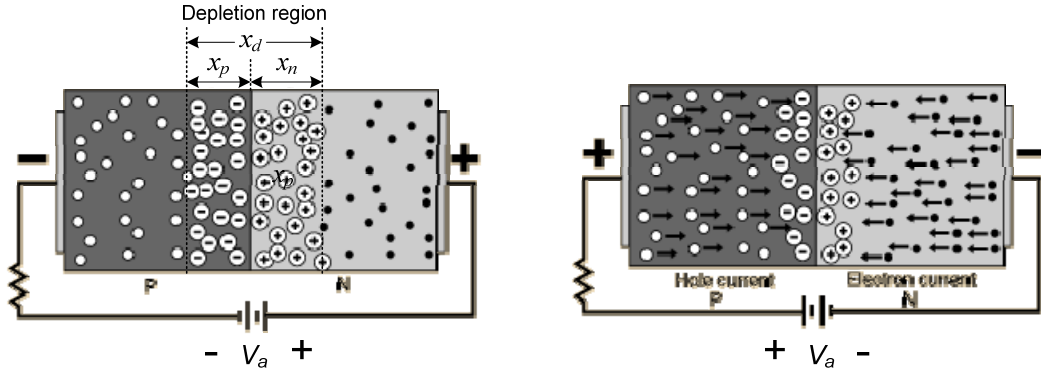


Fig. 2.10 p-n junction under (a) reverse and (b) forward bias

The full-depletion approximation assumes that the depletion region around the junction has well-defined edges. It also assumes that the transition between the depleted and the quasi-neutral region is abrupt. We define the quasi-neutral region as the region adjacent to the depletion region where the electric field is small and the free carrier density is close to the net doping density.

We will therefore start the electrostatic analysis using an abrupt charge density profile, while introducing two unknowns, namely the depletion layer width in the  $p$ -type region,  $x_p$ , and the depletion region width in the  $n$ -type region,  $x_n$ . The sum of the two depletion layer widths in each region is the total depletion layer width  $x_d$ , or:

$$x_d = x_n + x_p \quad (2.4.3)$$

Since in thermal equilibrium the electric field in the neutral regions of the semiconductor must be zero, the total negative charge per unit area in the  $p$  side must be precisely equal to the total positive charge per unit area in the  $n$  side. This provides the first relationship between the two unknowns,  $x_p$  and  $x_n$ , namely [11]:

$$N_D x_n = N_A x_p \quad (2.4.4)$$

We can then combine (2.4.3) with (2.4.4) for the total depletion-layer width,  $x_d$ , yielding:

$$x_n = x_d \frac{N_A}{N_A + N_D} \quad (2.4.5)$$

and

$$x_p = x_d \frac{N_D}{N_A + N_D} \quad (2.4.6)$$

The total potential across the semiconductor must equal the difference between the built-in potential and the applied voltage, which provides a second relation between  $x_p$  and  $x_n$ , namely [11]:

$$\phi_i - V_a = \frac{qN_D x_n^2}{2\epsilon_s} + \frac{qN_A x_p^2}{2\epsilon_s} \quad (2.4.7)$$

here  $\epsilon_s$  is the permittivity of the semiconductor.

The depletion layer width is obtained by substituting the expressions for  $x_p$  and  $x_n$ , (2.4.5) and (2.4.6), into the expression for the potential across the depletion region, yielding [11]:

$$x_d = \sqrt{\frac{2\epsilon_s}{q} \left( \frac{1}{N_A} + \frac{1}{N_D} \right) (\phi_i - V_a)} \quad (2.4.8)$$

from which the solutions for the individual depletion layer widths,  $x_p$  and  $x_n$  are obtained:

$$x_n = \sqrt{\frac{2\epsilon_s}{q} \frac{N_A}{N_D} \frac{1}{N_A + N_D} (\phi_i - V_a)} \quad (2.4.9)$$

$$x_p = \sqrt{\frac{2\epsilon_s}{q} \frac{N_D}{N_A} \frac{1}{N_A + N_D} (\phi_i - V_a)} \quad (2.4.10)$$

Any variation of the charge within a p-n diode with an applied voltage variation yields a capacitance, which must be added to the circuit model of a p-n diode. This capacitance related to the depletion layer charge in a p-n diode is called the junction capacitance.

The capacitance versus applied voltage is by definition the change in charge for a change in applied voltage, or:

$$C(V_a) = \left| \frac{dQ(V_a)}{dV_a} \right| \quad (2.4.11)$$

The absolute value sign is added in the definition so that either the positive or the negative charge can be used in the calculation, as they are equal in magnitude. Using  $Q_n = qN_D x_n$  and (2.4.9) one obtains [11]:

$$C_j = \sqrt{\frac{q\epsilon_s}{2(\phi_i - V_a)} \frac{N_A N_D}{N_A + N_D}} \quad (2.4.12)$$

A comparison with (2.4.8), which provides the depletion layer width,  $x_d$ , as a function of voltage, reveals that the expression for the junction capacitance (per unit surface area),  $C_j$ , seems to be identical to that of a parallel plate capacitor, namely:

$$C_j = \frac{\epsilon_s}{x_d} \quad (2.4.13)$$

The difference, however, is that the depletion layer width and hence the capacitance is voltage dependent. The parallel plate expression still applies since charge is only added at the edge of the depletion regions. The distance between the added negative and positive charge equals the depletion layer width,  $x_d$ .

The capacitance of a p-n diode is frequently expressed as a function of the zero bias capacitance,  $C_{j0}$  [11] :

$$\frac{1}{C_j^2} = \frac{2}{q\epsilon_s} \frac{N_A + N_D}{N_A N_D} (\phi_i - V_a) \quad (2.4.14)$$

where

$$\frac{d(\frac{1}{C_j^2})}{dV_a} = -\frac{2}{q\epsilon_s} \frac{N_A + N_D}{N_A N_D} \quad (2.4.15)$$

A capacitance versus voltage measurement (C-V measurement) can be used to obtain the built-in voltage and the doping density of a one-sided p-n diode. When plotting the inverse of the capacitance squared, one expects a linear dependence as expressed by:

$$N_D = -\frac{2}{q\epsilon_s} \frac{1}{\frac{d(1/C^2)}{dV_a}}, \text{ if } N_A \gg N_D \quad (2.4.16)$$

The built-in voltage is obtained at the intersection of the  $1/C^2$  curve and the horizontal axis, while the doping density is obtained from the slope of the curve.

#### 2.4.2 p-i-n junction

A p-i-n junction is similar to a p-n junction, but contains in addition an intrinsic or un-intentionally doped region with thickness,  $d_i$ , between the  $n$ -type and  $p$ -type layer. Such structure is typically used if one wants to increase the width of the depletion region. In the modulator a wide depletion region is required for a large overlap of the optical wave with the controlling electrical field.

The analysis is also similar to that of a p-n diode, although the potential across the undoped region,  $\phi_u$ , must be included in the analysis. (2.4.7) then becomes [11]:

$$\phi_n + \phi_p + \phi_u = \phi_i - V_a \quad (2.4.17)$$

$$\phi_n = \frac{qN_D x_n^2}{2\epsilon_s}, \phi_p = \frac{qN_A x_p^2}{2\epsilon_s}, \text{ and } \phi_u = \frac{qN_A x_p d_i}{\epsilon_s} \quad (2.4.18)$$

while the charge in the  $n$ -type region still equals that in the  $p$ -type region, so that (2.4.4) still holds:

$$qN_D x_n = qN_A x_p \quad (2.4.19)$$

From  $x_n$  and  $x_p$ , all other parameters of the p-i-n junction can be obtained. The total depletion layer width,  $x_d$ , is obtained from [11]:

$$x_d = x_n + x_p + d_i = \sqrt{d_i^2 + \frac{2\epsilon_s}{q} \frac{N_A + N_D}{N_A N_D} (\phi_i - V_a)} \quad (2.4.20)$$

The capacitance of a p-i-n diode equals the series connection of the capacitances of each region, simply by adding both depletion layer widths and the width of the undoped region, and similar to p-n junction, the capacitance is voltage dependent.

## 2.5 METAL-SEMICONDUCTOR CONTACTS

Metal-semiconductor contacts are an obvious component of any semiconductor device. At the same time, such contacts cannot be assumed to have a resistance as low as that of two connected metals. In particular, a large mismatch between the Fermi energy of the metal and semiconductor can result a high-resistance rectifying contact. A proper choice of materials can provide a low resistance Ohmic contact.

In the modulator, the contact between the gold and  $p$ -doped InP is an Ohmic contact. Hence, we focus on Ohmic contact in this section.

### 2.5.1 Ohmic Contact

A metal-semiconductor junction results in an Ohmic contact (i.e. a contact with voltage independent resistance) if the Schottky barrier height is zero or negative. In such case, the carriers are free to flow in or out of the semiconductor so that there is a minimal resistance across the contact. For an  $n$ -type semiconductor, this means that the workfunction of the metal must be close to or smaller than the electron affinity of the semiconductor. For a  $p$ -type semiconductor, it requires that the workfunction of the metal must be close to or larger than the sum of the electron affinity and the bandgap energy.

For an Ohmic contact, the contact resistivity,  $\rho_c$ , is given by [12]

$$\rho_c = \rho_{c0} \cdot e^{K \frac{\phi_B}{\sqrt{N}}} \Omega \cdot \text{cm}^2 \quad (2.5.1)$$

where  $K$  and  $\rho_{c0}$  are constants dependent upon metal and the semiconductor.  $\rho_c$ , primarily depends upon the metal-semiconductor work function,  $\Phi_B$ , and doping density,  $N$ , in the semiconductor.

Since the workfunction of most metals is less than 5 eV and a typical electron affinity is about 4 eV, it can be problematic to find a metal that provides an Ohmic contact to  $p$ -type semiconductors with a large bandgap. An alternate and more practical contact is a tunnel contact. Such contacts do have a positive barrier at the

metal-semiconductor interface, but also have a high enough doping in the semiconductor so that there is only a thin barrier separating the metal from the semiconductor. If the width of the depletion region at the metal-semiconductor interface is very thin, on the order of 3 nm or less, carriers can readily tunnel across such barrier. The required doping density for such contact is  $10^{19} \text{ cm}^{-3}$  or higher.

The fabrication of Ohmic contacts frequently includes a high temperature step so that the deposited metals can either alloy with the semiconductor or the high-temperature anneal reduces the unintentional barrier at the interface.

### 2.5.2 Extracting the Contact Resistance

Although the definition of  $\rho_c$  as (2.5.1) is precise, extracting contact resistance measured in a device or a test structure is not straightforward because of a nonuniform current density. This must be addressed through a transmission line-like approach.

The contact between a metal and a thin semiconductor layer can be described using a 1-D model with the resistive network shown in Fig. 2.11. This equivalent circuit is obtained by slicing the structure into small sections with length  $\Delta x$ , so that for each section the contact resistance,  $R_1$ , and the semiconductor resistance,  $R_2$ , are given by

$$R_1 = \frac{\rho_c}{w_c \cdot \Delta x} \quad \text{and} \quad R_2 = R_{sh} \frac{\Delta x}{w_c} \quad (2.5.2)$$

where  $\rho_c$  is the contact resistivity of the metal-to-semiconductor interface with units of  $\Omega \cdot \text{cm}^2$ ,  $R_{sh}$  is the sheet resistance of the semiconductor layer with units of  $\Omega/$  (ohms per square), and  $w_c$  is the width of the contact (cf. Fig. 2.12(a)).

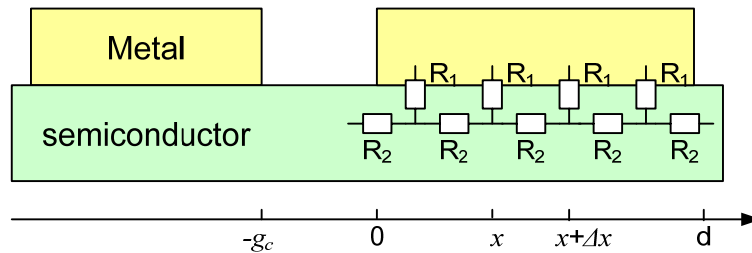


Fig. 2.11 Distributed resistance model of a contact to a thin semiconductor layer

The 1-D analysis gives the following equations [13] for the contact resistance in the structure shown in Fig. 2.11

$$R_c = \frac{\xi \cdot R_{sh}}{w_c} \cdot \coth \frac{d}{\xi} = \frac{\sqrt{\rho_c \cdot R_{sh}}}{w_c} \cdot \coth \frac{d}{\xi} \quad (2.5.3)$$

$$\text{with } \xi = \sqrt{\frac{\rho_c}{R_{sh}}} \quad (2.5.4)$$

$R_c$  is the total resistance of the contact and the parameter  $\xi$  is the characteristic distance over which the current changes under the metal contact and is also referred to as the penetration length. In the limit for an infinitely long contact (or  $d \gg \xi$ ) the contact resistance is given by

$$R_c = \frac{\sqrt{\rho_c \cdot R_{sh}}}{w_c}, \text{ for } d \gg \xi \quad (2.5.5)$$

A measurement of the resistance between a set of contacts with a variable distance  $g_c$  between the contacts (also referred to as a TLM structure, cf. Fig 2.12(a)) can therefore be fitted to the following straight line [13]

$$R = 2 \cdot \frac{\sqrt{\rho_c \cdot R_{sh}}}{w_c} + R_{sh} \cdot \frac{g_c}{w_c} \quad (2.5.6)$$

so that the resistance per square,  $R_{sh}$ , can be obtained from the slope, while the contact resistivity,  $R_c$ , can be obtained from the intersection with the  $y$ -axis. The penetration depth,  $\xi$ , can be obtained from the intersection with the  $x$ -axis. This is illustrated in Fig. 2.12(b).

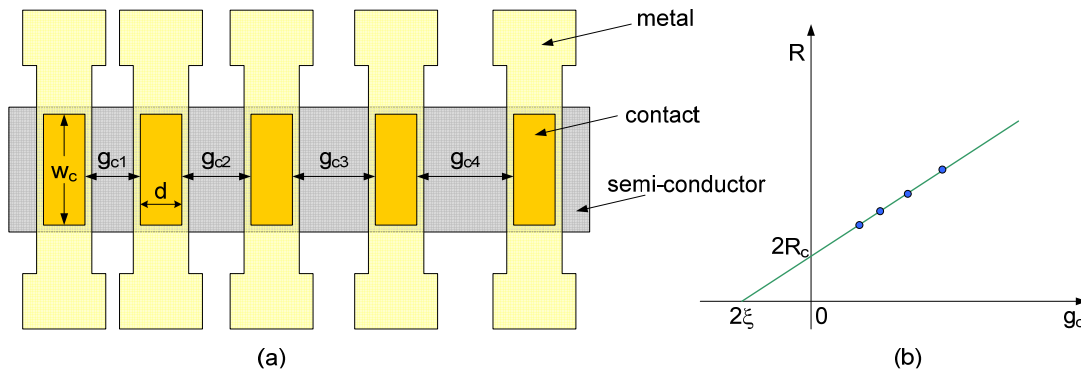


Fig. 2.12 (a) A TLM test structure and (b) contact resistance versus contact spacing

## 2.6 THE ELECTRO-OPTIC COEFFICIENT

According to the quantum theory of solids, the optical dielectric impermeability tensor depends on the distribution of charges in the crystal. The application of an electric field will result in a redistribution of bond charges and possibly a slight deformation of the ion lattice. The net result is a change in the optical impermeability tensor. This is known as the electro-optic (EO) effect [14]

EO effect denotes the change of optical refractive index in nonlinear optical (NLO) crystals due to the presence of an electric field. The index change leads to a change in the optical phase, which can be converted into an intensity modulation in a Mach-Zehnder interferometer (MZI). A convenient way to visualize the EO effect is to use the index ellipsoid of the crystal [14]. The refractive indexes for an optical wave propagating in a crystal can be found from the intersection ellipse between the index ellipsoid and the plane that is normal to the propagation direction and through the center of the ellipsoid, as illustrated in Fig. 2.13. The lengths of the two axes of the intersection ellipse are the refractive indexes ( $n_1$  or  $n_2$ ) for optical waves polarized along these axes.

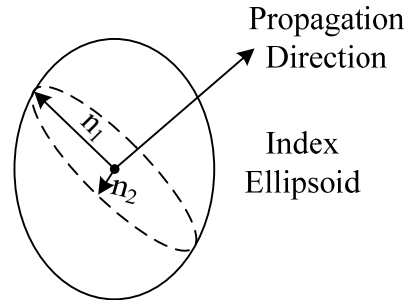


Fig. 2.13 Illustration of index ellipsoid, the dashed ellipse is the intersection of the index ellipsoid with the plane normal to the propagation direction

In the principal coordinate system and in the absence of an electric field, the index ellipsoid can be represented by

$$\frac{x^2}{n_x^2} + \frac{y^2}{n_y^2} + \frac{z^2}{n_z^2} = 1 \quad (2.6.1)$$

where the directions of  $x$ ,  $y$  and  $z$  are the principal dielectric axes with the corresponding refractive indexes  $n_x$ ,  $n_y$  and  $n_z$ . After the electric field is applied, both the size and the orientation of the index ellipsoid are changed. The equation of the index ellipsoid is generally modified to [14]

$$x^2 \frac{1}{n_1^2} + y^2 \frac{1}{n_2^2} + z^2 \frac{1}{n_3^2} + 2yz \frac{1}{n_4^2} + 2zx \frac{1}{n_5^2} + 2xy \frac{1}{n_6^2} = 1 \quad (2.6.2)$$

Comparing (2.6.2) and (2.6.1), it is apparent that, without an applied electric field

$$\frac{1}{n_1^2} = \frac{1}{n_x^2}, \quad \frac{1}{n_2^2} = \frac{1}{n_y^2}, \quad \frac{1}{n_3^2} = \frac{1}{n_z^2}, \quad \frac{1}{n_4^2} = \frac{1}{n_5^2} = \frac{1}{n_6^2} = 0 \quad (2.6.3)$$

After an electric field is applied, the above six terms may be changed. When only the linear EO effect is considered, the change induced by the electric field  $\vec{E} = (E_x, E_y, E_z)$  can be expressed as [14]

$$\begin{bmatrix} \Delta \frac{1}{n_1^2} \\ \Delta \frac{1}{n_2^2} \\ \Delta \frac{1}{n_3^2} \\ \Delta \frac{1}{n_4^2} \\ \Delta \frac{1}{n_5^2} \\ \Delta \frac{1}{n_6^2} \end{bmatrix} = \begin{bmatrix} r_{11} & r_{12} & r_{13} \\ r_{21} & r_{22} & r_{23} \\ r_{31} & r_{32} & r_{33} \\ r_{41} & r_{42} & r_{43} \\ r_{51} & r_{52} & r_{53} \\ r_{61} & r_{62} & r_{63} \end{bmatrix} \begin{bmatrix} E_x \\ E_y \\ E_z \end{bmatrix} \quad (2.6.4)$$

where the  $6 \times 3$  matrix  $[r_{ij}]$  is called the electro-optic tensor, and its elements are called electro-optic coefficients.

The values of index terms in (2.6.2) are now the sum of the original values in (2.6.3) plus the corresponding changes in (2.6.4). For various crystals, due to the crystal symmetry, some of the EO coefficients may be zero, and some of them may be equal in value (or opposite in sign) [14]. With the EO tensor determined, the modified index ellipsoid due to an arbitrary electric field can be found through (2.6.2)-(2.6.4), and the refractive indexes for an arbitrary optical wave can be determined using the index ellipsoid.

III-V semiconductors are Zinc Blende ( $\bar{4}3m$ ) crystals and are not intrinsically birefringent. To consider the EO effect, the principal x, y, and z axes are usually chosen along [100], [010], and [001] crystal orientations, respectively. Due to the symmetry of Zinc Blende crystals, the EO tensor takes the form of [14]

$$\begin{bmatrix} 0 & 0 & 0 \\ 0 & 0 & 0 \\ 0 & 0 & 0 \\ r_{41} & 0 & 0 \\ 0 & r_{41} & 0 \\ 0 & 0 & r_{41} \end{bmatrix} \quad (2.6.5)$$

For InP,  $r_{41}$  is around 1.4 pm/V and  $n_x = n_y = n_z = n_0$ . Combining (2.6.5) with (2.6.1)-(2.6.4), the index ellipsoid for InP with the presence of an electric field is

$$\frac{x^2 + y^2 + z^2}{n_0^2} + 2r_{41}(yzE_x + zxE_y + xyE_z) = 1 \quad (2.6.6)$$

Where  $n_0$  is about 3.2 for InP. Since the crystal growth usually proceeds perpendicular to the (001) surface and along the z-axis direction, it is most convenient to apply an electric field along the z-axis. In the case  $E_x=E_y=0$  then (2.6.6) becomes

$$\frac{x^2 + y^2 + z^2}{n_0^2} + 2r_{41}xyE_z = 1 \quad (2.6.7)$$

Due to the off-diagonal component in (2.6.7), the principal axes in xy plane are rotated 45° in the presence of the electric field  $E_z$ , and they are along [110] ( $x'$ -axis) and  $[\bar{1}10]$  ( $y'$ -axis) directions. Therefore, the index ellipsoid in the new coordinate system can be represented by [15]

$$x'^2 \left( \frac{1}{n_0^2} + r_{41}E_z \right) + y'^2 \left( \frac{1}{n_0^2} - r_{41}E_z \right) + \frac{z^2}{n_0^2} = 1 \quad (2.6.8)$$

(2.6.8) shows that for waveguide designed along [110] ( $x'$ -axis) or  $[\bar{1}10]$  ( $y'$ -axis) direction, the index modulations are [15]

$$n_{y'} = \left( \frac{1}{n_0^2} - r_{41}E_z \right)^{\frac{1}{2}} \approx n_0 + \frac{1}{2} r_{41} n_0^3 E_z \quad (2.6.9)$$

or

$$n_x = \left( \frac{1}{n_0^2} + r_{41} E_z \right)^{\frac{1}{2}} \approx n_0 - \frac{1}{2} r_{41} n_0^3 E_z. \quad (2.6.10)$$

Only the index of the TE mode is modified, while the TM mode (polarized along  $z$ -axis) is not affected [15]. The corresponding index change due to the electric field can be expressed as

$$\Delta n = \pm \frac{1}{2} r_{41} n_0^3 E_z \quad (2.6.11)$$

The waveguide orientation is chosen in such a way that the index change by EO effect will be added to that of the QCSE.

## 2.7 QUANTUM CONFINED STARK EFFECT (QCSE)

If electrons and holes are confined to semiconductor quantum-wells, their energy states transform into discrete energy levels called "subbands" in contrast to the continuous energy bands of bulk semiconductors. In addition, the confined electrons and holes are electrically bound to form so-called excitons, and compared to bulk material they exhibit a much smaller Bohr radius and a much larger binding energy [15]. These specific QW properties cause very different optical properties compared to that in bulk material.

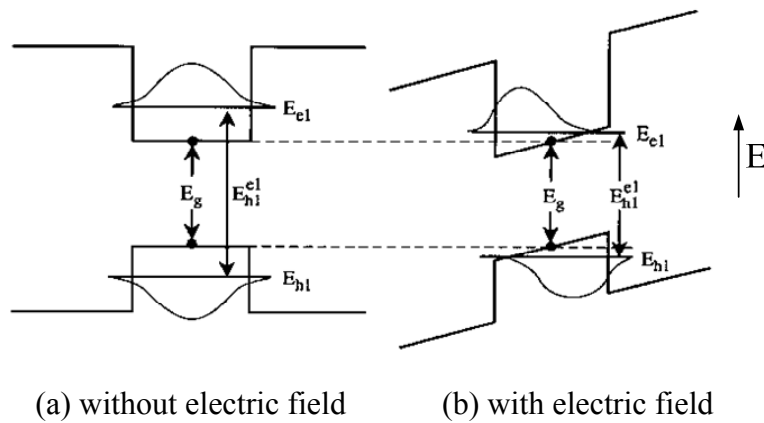


Fig. 2.14 Energy levels of a QW structure without and with applied electric field [16]

Fig. 2.14 shows energy levels of a QW structure without and with applied electric field which is perpendicular to the wells, i.e. along the direction of quantum-well layer growth.  $E_{e1}$  lines represent the 1st electron energy level,  $E_{h1}$  lines represent the 1<sup>st</sup> hole energy level. For the sake of simplicity, we will neglect the degeneracy of the valence band as encountered in III-V semiconductors such as GaAs or InP for example, and we will also neglect the effect of strain although QWs are frequently grown under strain. Even under these simplifying assumptions the main arguments will still remain valid.

Curves in the well represent the envelope wavefunctions for electrons and holes. As illustrated in Fig. 2.14, two main changes occur when an electric field is applied across a QW. First, the energy levels of the electrons  $E_e$  and those of the holes  $E_h$  are lowered, and as a consequence the exciton absorption peak shifts to lower energies (longer wavelengths). Second, due to the tilted band diagram the electrons and the holes get spatially separated which reduces the overlap of the electron and hole wavefunctions. This reduced overlap lowers the exciton binding energy which tends to introduce a blue-shift of the exciton absorption, however, this effect is significantly less pronounced than the red-shift due to the field-induced change of the energy levels (subbands). Furthermore, the exciton linewidth is also broadened due to the presence of the electric field. Altogether, an applied electric field causes a significant shift of the optical absorption to longer wavelengths (compared to the case without applied electric field), and this effect is known as the QCSE.

Due to the strong exciton resonance, QCSE induced absorption change is much larger than that of the Franz-Keldysh effect (FKE).

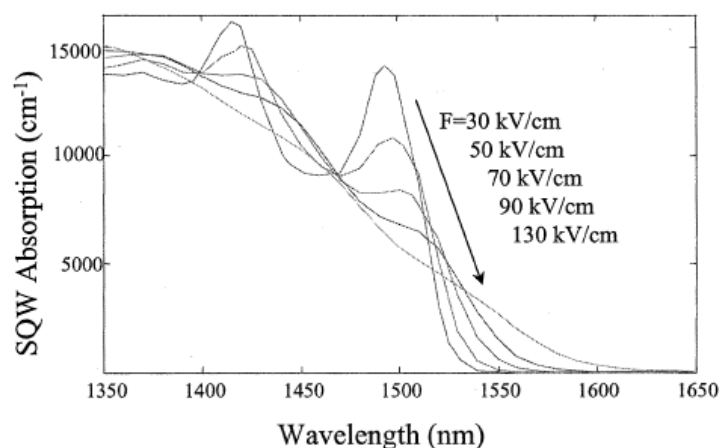


Fig. 2.15 Simulated absorption spectra for a QW under different electric field [15]

According to the Kramers-Kronig relations a shift of the bandgap (and of the absorption) is associated with a modification of the refractive index, and this is the phenomenon which is exploited for the design of electrooptic modulators. For QCSE-based MZM, the detuning energy (i.e. the energy difference between the bandgap of the QWs and the operation wavelength of the modulator) is typically around 60-80 meV. For example, if the QCSE shown in Fig. 2.15 represents that of the QW in MZM waveguides, the optical wavelength for this MZM is in the 1600-1650 nm wavelength range. In this range, the optical absorption is very small, while the electric-field-induced index change can be sufficiently large for efficient phase modulation. In the MZM devices used in this work the photoluminescence of the MQW layer stack is designed at 1420 nm. This is far away from the operating wavelength ( $\lambda=1550$  nm) and leads to low absorption. The ideal QCSE for MZM operation would be a large QCSE red-shift and a sharp and high exciton peak with minimum field-induced broadening. For properly designed MQW structures, the field-induced index change at a small voltage can be larger than  $10^{-3}$ , i.e. it is significantly more pronounced than the index change induced by the linear EO effect [15].

## 2.8 CHIRP ANALYSIS

In general, the intensity modulation is accompanied by an optical phase modulation, which results in optical frequency (wavelength) chirp. This effect is an important concern for digital fiber links which typically use the wavelength of 1.55  $\mu\text{m}$  to minimize optical loss in the long-distance fiber. The frequency chirp may result in increased pulse broadening after propagating through a fiber with nonzero dispersion, and lead to increased bit error rate (BER) [15].

In the direct modulation of a semiconductor laser, the frequency chirp is caused by the refractive index change of the active layer due to the carrier density modulation. External modulators are considered to be alternative candidates in order to eliminate this problem.

In analysis of external optical modulators, if the optical output of a modulator is expressed in the form of [15]

$$A_{out} = A_0(V) \cdot e^{j\phi(V)} \quad (2.8.1)$$

where  $A_0(V) = \sqrt{I}$  ( $I$  is the modulated optical intensity),  $\phi(V)$  is the accompanied phase change, then the  $\alpha$ -parameter for the external modulator can be expressed as (2.8.2) [15].

$$\alpha_{chirp} = -A_0 \frac{\frac{\partial \phi}{\partial V}}{\frac{\partial A_0}{\partial V}} \quad (2.8.2)$$

## REFERENCES

- [1] K. C. Gupta, "Microstrip lines and slotlines", 2<sup>nd</sup> Ed., Artech House: Boston, London (1996)
- [2] W. Hilberg, "From approximations to exact relations for characteristic impedances", IEEE Trans. MTT **17**, 259-265 (1969)
- [3] E. Jahnke, F. Emde, and F. Lösch, "Tables of higher functions", McGraw-Hill, New York (1960)
- [4] M. Riazat, "Propagation modes and dispersion characteristics of coplanar waveguides", IEEE Trans. MTT **38**, 245-251 (1990)
- [5] R. E. Collin, "Foundations for microwave engineering", 2<sup>nd</sup> Ed., McGraw-Hill
- [6] David M. Pozar, "Microwave engineering", 3<sup>rd</sup> Ed., Wiley (2005)
- [7] S. Ramo, J. R. Whinnery and T. Duzer, "Fields and waves in communication electronics", 3<sup>rd</sup> Ed., Wiley, New York (1994)
- [8] S. Adachi, "Physical properties of III-V semiconductor compounds: InP, InAs, GaAs, GaP, InGaAs, and InGaAsP", Wiley (1992)
- [9] G. P. Agrawal and N. K. Dutta, "Semiconductor Lasers", 2<sup>nd</sup> Ed., Van Nostrand Reinhold, New York, (1993)
- [10] B. Saleh and M. Teich, "Fundamental of photonics", Wiley, New York (1991)
- [11] S. M. Sze, "Semiconductor devices", Wiley, New York (1985)
- [12] S. M. Sze, "Physics of semiconductor devices", 2<sup>nd</sup> Ed., Wiley, New York (1981)
- [13] D. K. Schroder, "Semiconductor material and device characterization", 3<sup>rd</sup> Ed., Wiley (2006)
- [14] A. Yariv, "Optical electronics in modern communications", 5<sup>th</sup> Ed. Oxford university press, New York, Oxford (1997)
- [15] K. Chang, "Handbook of optical components and engineering", Wiley, Hoboken, NJ (2003)
- [16] S. L. Chuang, "Physics of optoelectronic devices", Wiley, New York (1995)
- [17] F. Koyama and K. IGA, "Frequency chirping in external modulators", IEEE J. Lightwave Technol. **6**, 87-93 (1988)

## Chapter 3

### Mach-Zehnder Modulator Design

#### 3.1 MACH-ZEHNDER INTERFEROMETER

The Mach-Zehnder interferometer (MZI) is the most popular device for implementing optical intensity modulation using the EO effect. Modulators in this work are also based on the concept of the MZI. Fig. 3.1 is a schematic drawing of such an interferometer.



Fig. 3.1 Schematic of a Mach-Zehnder Interferometer with 2 Y-branch

The operation of a Mach-Zehnder modulator is quite straightforward. An incoming optical wave is split and then fed into two arms. The optical wave in each arm can be phase modulated. The phase of the optical signal in each arm can be manipulated independently. When the two optical signals are combined at the output, constructive interference will occur if the relative phase between the two arms is  $0^\circ$  and the output intensity will ideally be the same as that at the input. Conversely, if the relative phase between the two arms is  $180^\circ$ , destructive interference will occur and the light at the output will be completely extinguished.

Between these two extremes, the output intensity will vary in accordance with the difference in phase between two arms.

The optical field amplitude at the output of the MZI can be generally represented by [1]

$$A_{out} = \frac{\sqrt{2}}{2} (A_1 e^{j\phi_1} + A_2 e^{j\phi_2}) \quad (3.1.1)$$

where  $A_1$  and  $A_2$  represent the optical amplitudes in the two arms, and  $\phi_1$  and  $\phi_2$  represent the optical phase delays. The input optical power is

$$P_{in} = A_1^2 + A_2^2 \quad (3.1.2)$$

And the output optical power is [1]

$$P_{out} = |A_{out}|^2 = \frac{1}{2} [A_1^2 + A_2^2 + 2A_1A_2 \cos(\phi_1 - \phi_2)] \quad (3.1.3)$$

The phase difference  $\phi_1 - \phi_2$  consists of two parts: one is the phase difference  $\phi_0$  at zero applied voltage; the other is the phase difference  $\Delta\phi$  due to the applied voltage. Dividing  $P_{out}$  by the input optical power  $P_{in}$ , the optical intensity transfer function of the MZI can be written in the form of [1]

$$T_{MZI} = \frac{P_{out}}{P_{in}} = \frac{1}{2} [1 + b \cos(\Delta\phi + \phi_0)] \quad (3.1.4)$$

with  $b = \frac{2A_1A_2}{A_1^2 + A_2^2}$

where  $b$  is an optical imbalance factor between two arms. For an ideally balanced symmetric design, which means  $A_1 = A_2$ ,  $b = 1$  and  $\phi_0 = 0$  (3.1.4) can be simplified as (3.1.5). The corresponding transfer curve is shown in Fig. 3.2.

$$T_{MZI} = \frac{1}{2} [1 + \cos(\Delta\phi)] = \cos^2\left(\frac{\Delta\phi}{2}\right) \quad (3.1.5)$$

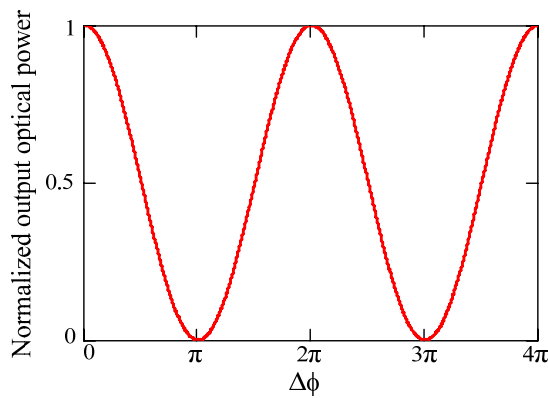


Fig. 3.2 Transfer curve for MZI with 2 Y-branches

Optical loss at the devices facets and during the propagation is ignored in the above derivation. If the optical loss is taken into account and the ideal balance is not achieved (assuming  $b=0.9$ ), the transfer curve will change, as shown in Fig. 3.3 [1].

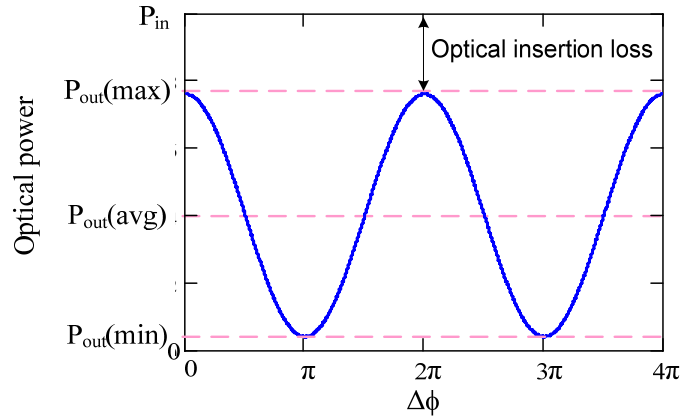


Fig. 3.3 Transfer curve of an MZI with 2 Y-branches with optical loss,  $b=0.9$

### 3.2 ELECTRODE CONSIDERATION

As introduced in Chapter 2, in EO modulators, the EO effect denotes the change of optical refractive index in semiconductor materials due to the presence of an electric field. This index change leads to a change in optical phase, which can be converted into an intensity modulation in a MZI. The electric field is formed by an applied biased electrical modulating signal through the electrode which is deposited over the optical waveguide.

#### 3.2.1 Lumped Electrode

Due to its high EO efficiency, the QCSE-based modulator has a relative short waveguide. Therefore, a simple approach is using a lumped electrode in the MZI (so-called single-arm modulation), which length is small compared to the RF wavelength, as shown in Fig. 3.4. A metal stripe covers one arm of the MZI, usually a p-type Ohmic contact is fabricated directly on top of the optical waveguide (cf. Fig. 3.5). A metal square, serving as wire-bonding pad or probing pad, is fabricated adjacent to the

waveguide and is electrically connected to the middle point of the stripe. This bonding pad contributes parasitic capacitance to the device and causes a reduction of the modulation bandwidth. The cross sectional view of the optical waveguide with covered lumped electrode are shown in Fig. 3.5.

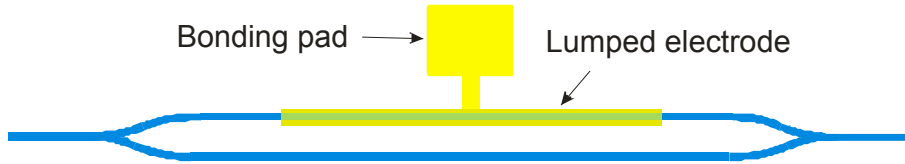


Fig. 3.4 Schematic of a MZM with a lumped electrode

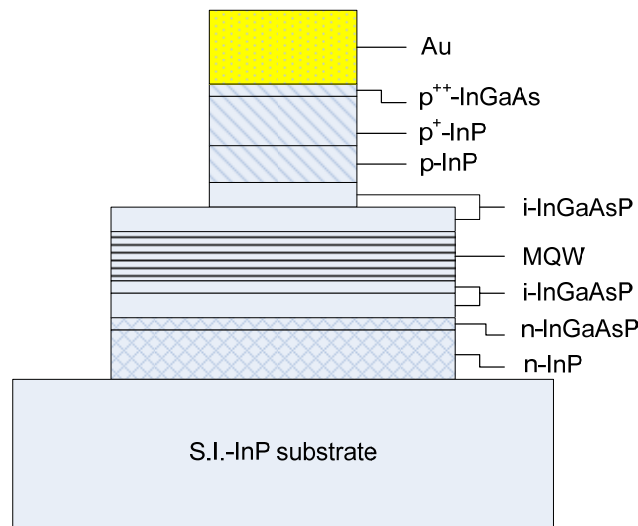


Fig. 3.5 Cross section of the optical waveguide covered with a lumped electrode

The equivalent circuit model for the MZM with a lumped electrode is given as shown in Fig. 3.6. The derived 3 dB cutoff frequency is expressed as (3.2.1) [1].

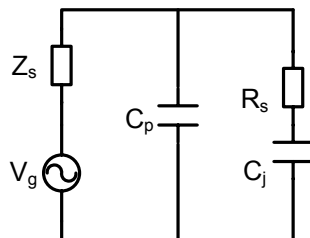


Fig. 3.6 The equivalent circuit model for the MZM with a lumped electrode

$$f_{3dB} = \frac{1}{2 \cdot \pi \cdot R \cdot C_j} \quad (3.2.1)$$

where  $R=Z_s+R_s$  and  $C_p$  is neglected (assuming  $C_j \gg C_p$ ) in the analysis. Taking  $R$  of  $50 \Omega$  and  $C_j$  of  $0.364 \text{ pF}$ , for a modulator with a  $2.8 \mu\text{m}$  wide and  $1 \text{ mm}$  long lumped electrode (the junction capacitance per unit area is  $130 \text{ pF/mm}^2$  with  $-5 \text{ V}$  bias voltage), one gets  $f_{3dB}$  of  $8.75 \text{ GHz}$ , which is too narrow for an application beyond  $40 \text{ Gbit/s}$ .

Moreover, the single-arm modulation has the problem of frequency chirp due to its asymmetric modulation [1]. To improve the chirp parameter for single-arm modulation,  $\pi$ -phase-shifted waveguide design is often used [2,3].

### 3.2.2 Push-Pull Structure

The concept of a push-pull drive applies to two-path interferometric devices in which a common field or voltage is used to phase modulate the two interfering waves in anti-phase, thus doubling the effect and virtually eliminating phase chirp at the output. In a MZI, two arms may be considered as independent capacitive devices and are ideal for a push-pull implementation as shown in Fig. 3.7.

The series push-pull drive, as shown in Fig. 3.8, has an inherent capacity to double the bandwidth of MZM substantially without driving voltage increase because the series connection of two capacitance halves the effective  $C_j$  in equation (3.2.1). Although the series connection divides the modulating voltage between two arms, the effect sums at the output.

Moreover, the built-in back-to-back connection of p-i-n diodes (cf. Fig. 3.8) which constitute the Mach-Zehnder electrodes also makes the series push-pull the most natural to implement in semiconductor based modulators. In addition, due to its symmetric property, zero chirp can be achieved, which is a big advantage of push-pull MZMs [4].

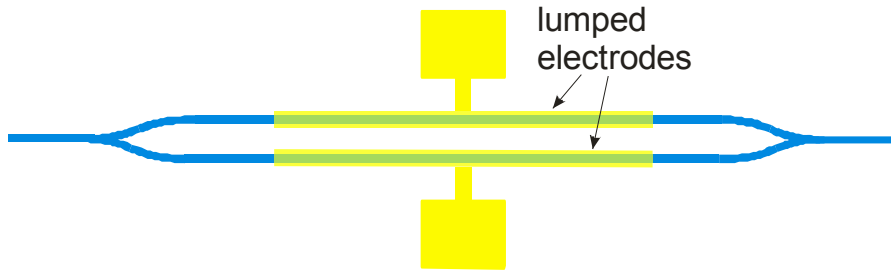


Fig. 3.7 Schematic of a MZM with push-pull lumped electrodes

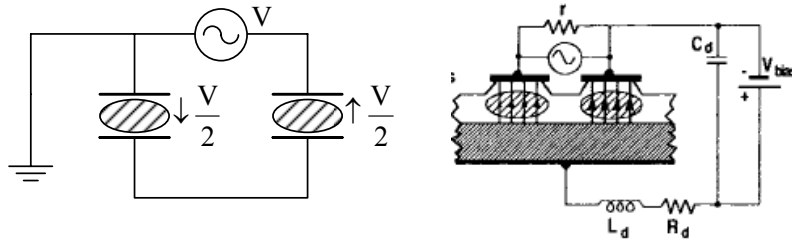


Fig. 3.8 The circuit model for series push-pull [4]

The design of an optical splitter and combiner is very critical to the performance of MZM. It affects both the optical insertion loss and the extinction ratio. Multimode interference (MMI) couplers are regarded as the best structure for these purposes [5]. Properly designed  $2 \times 2$  MMI can work as an excellent optical combiner, with small optical loss and high extinction ratio. It has also much tolerance to fabrication error and wavelength deviation [6]. Most important is that the MZI with a  $2 \times 2$  MMI as a combiner at the end can be biased with a single voltage.

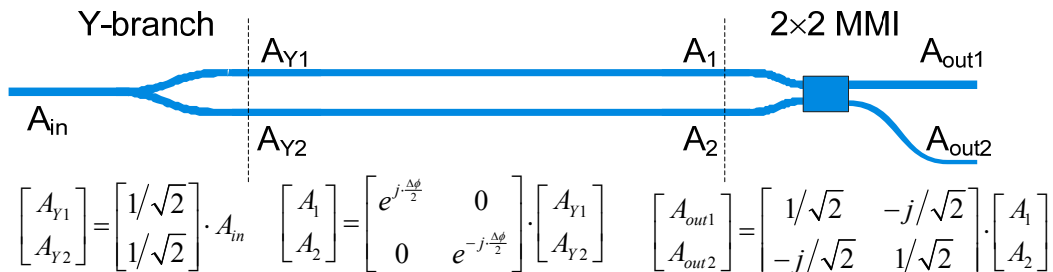


Fig. 3.9 Schematic of a MZI with one Y-branch and a  $2 \times 2$  MMI and the ideal transfer matrix for each section

If the output Y-branch in Fig. 3.1 is replaced by a 2×2 MMI, as shown in Fig. 3.9, the optical power from each arm is coupled into the MMI respectively. Assuming the Y-branch is ideally balanced, the phase difference in each arm of the MZI are equal but has opposite polarity due to the push-pull effect and the MMI is also

ideally balanced, One can use matrices  $\begin{bmatrix} \frac{1}{\sqrt{2}} \\ \frac{1}{\sqrt{2}} \end{bmatrix}$ ,  $\begin{bmatrix} e^{j\frac{\Delta\phi}{2}} & 0 \\ 0 & e^{-j\frac{\Delta\phi}{2}} \end{bmatrix}$  and

$\begin{bmatrix} \frac{1}{\sqrt{2}} & -\frac{j}{\sqrt{2}} \\ -\frac{j}{\sqrt{2}} & \frac{1}{\sqrt{2}} \end{bmatrix}$  to express the transmission property of Y-branch, MZI and MMI,

respectively, as shown in Fig. 3.9. The normalized transmission property of the MZI using the Y-branch as input and the MMI as output can be expressed in form of

$$T_{MZI} = \begin{bmatrix} \frac{1}{\sqrt{2}} & -\frac{j}{\sqrt{2}} \\ -\frac{j}{\sqrt{2}} & \frac{1}{\sqrt{2}} \end{bmatrix} \cdot \begin{bmatrix} e^{j\frac{\Delta\phi}{2}} & 0 \\ 0 & e^{-j\frac{\Delta\phi}{2}} \end{bmatrix} \cdot \begin{bmatrix} \frac{1}{\sqrt{2}} \\ \frac{1}{\sqrt{2}} \end{bmatrix} = \frac{1-j}{2} \cdot \begin{bmatrix} \cos(\frac{\Delta\phi}{2}) - \sin(\frac{\Delta\phi}{2}) \\ \cos(\frac{\Delta\phi}{2}) + \sin(\frac{\Delta\phi}{2}) \end{bmatrix} \quad (3.2.2)$$

And the normalized (set  $P_{in} = 1$ ) optical power outputs of the MMI,  $P_{out1}$  and  $P_{out2}$  are

$$P_{out1} = \left| \frac{1-j}{2} \cdot \left( \cos(\frac{\Delta\phi}{2}) - \sin(\frac{\Delta\phi}{2}) \right) \right|^2 = \frac{1 - \sin \Delta\phi}{2} \quad (3.2.3)$$

$$P_{out2} = \left| \frac{1-j}{2} \cdot \left( \cos(\frac{\Delta\phi}{2}) + \sin(\frac{\Delta\phi}{2}) \right) \right|^2 = \frac{1 + \sin \Delta\phi}{2} \quad (3.2.4)$$

The transfer function for  $P_{out1}$  and  $P_{out2}$  are plotted in Fig. 3.10. The corresponding push-pull intensity modulation schemes are shown in Fig. 3.11.

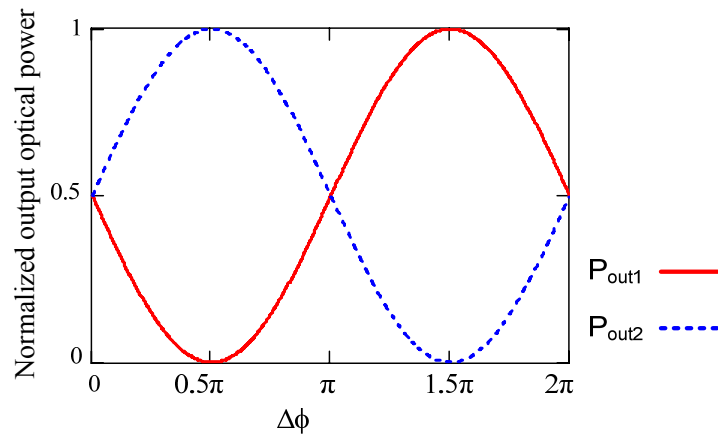


Fig. 3.10 Transmission character of Mach-Zehnder interferometer

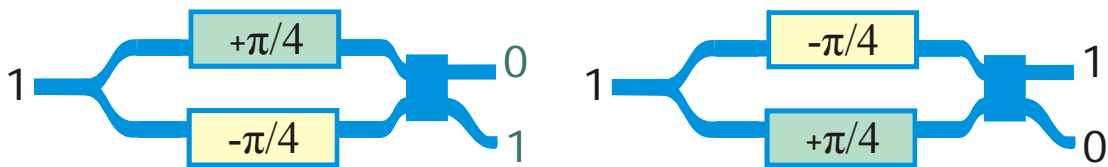


Fig. 3.11 Intensity modulation using push-pull structure

### 3.2.3 Traveling-Wave Electrode

Although the bandwidth of lumped electrode MZM can be broadened by using push-pull structure, it is still difficult to achieve the speed of 40 Gbit/s and above. To resolve this problem, the traveling-wave electrode (TWE) is introduced into the modulator design.

The fundamental idea underlying TWE in contrast to lumped electrodes is the fact that the distributed capacitance does not limit the modulator speed. Proper design enables identical propagation speed of the optical and the modulating electrical signal, permitting the phase modulation to accumulate monotonically irrespective of frequency.

Compare with the lumped electrode, in TWE MZM the inner electrodes used to modulate the optic wave that propagates under them are equally divided into many

small sections. Each of these sections can be taken as a small lumped capacitance, and is connected to the outer TWE periodically.

Fig. 3.12 illustrates the electrodes structure of the TWE MZM in detail. The complete MZI is surrounded by two broad electrodes which compose the CPS with the width of  $w$ , the length of  $l$  and the gap width  $s$ . Additionally a series of lumped phase modulation electrodes are arranged periodically with the period length of  $\Lambda$  along the optical waveguides and are connected with the wide electrode via air-bridges. These inner modulation electrodes of length of  $l_E$  are posited on the p-i-n structures which are appropriately placed as separated diodes to provide the EO interaction as shown in Fig. 3.13.  $l_E$  can expressed by

$$l_E = \Lambda \cdot \eta \quad (3.2.5)$$

where  $\eta$  is the fill factor , it can be varied between 0 and 1. The fill factor is the parameter used for tuning the capacitive load of the CPS.

At the beginning and the end of the CPS, two compensated right-angled bends are used to insert and terminate the electrical signal, so that the optical signal can propagates straight in the modulator. The upper broad electrode with two bends is called “U-electrode” in this dissertation because its shape looks like an upside-down “U”. The lower broad electrode is called “I-electrode” because its shape looks like a lying “I”.

The pin-diodes are all connected via the highly doped common n-layer as shown in the cross-sectional view of Fig. 3.13. DC-pads are connected to the n+ layer and are positioned outside of the interferometer on the MZI-mesa which spreads from one chip end to the other. The wide electrodes are isolated by a groove. The implementation of the single bias is also shown in Fig. 3.13.

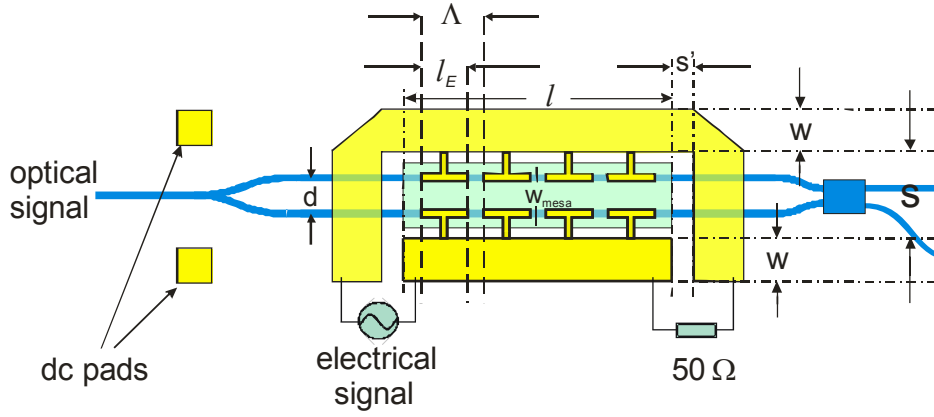


Fig. 3.12 Schematic of a MZM with capacitive loaded segmented traveling-wave electrode

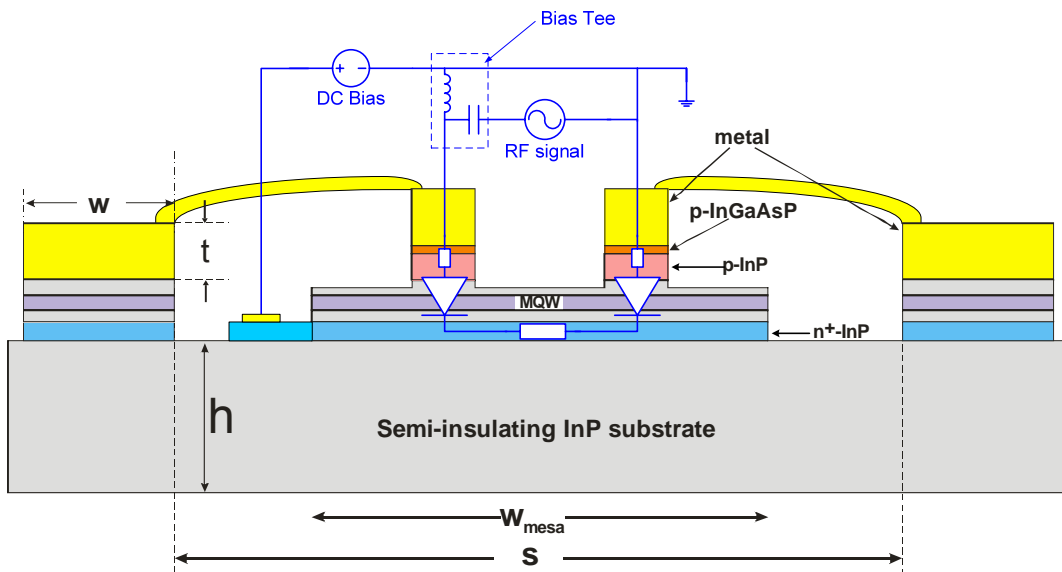


Fig. 3.13 Cross sectional view of a MZM with DC bias and RF circuit diagram

### 3.3 MICROWAVE DESIGN

The microwave design of the TWE MZM can be considered as a loaded transmission line design, while the active electrode in the modulator can be taken as a capacitive load of the segmented transmission line, which has been discussed in the preceding section.

The traveling-wave electrode is here the unloaded transmission line. It can be characterized by a series resistance  $R_0$ , an inductance  $L_0$ , a shunt impedance  $G_0$  and a capacitance  $C_0$  (all per unit length). For the low-loss case, the series resistance  $R_0$  and the shunt impedance  $G_0$  can be neglected. Thus, the characteristic impedance  $Z_0$  and microwave index  $n_\mu$  of unloaded line can be expressed as

$$Z_0 = \sqrt{\frac{L_0}{C_0}} \quad (3.3.1)$$

$$n_\mu = c \cdot \sqrt{L_0 \cdot C_0} \quad (3.3.2)$$

where  $c$  is the light speed in free space.

If the capacitive load (per unit length) is characterized as  $C_L$ , then the characteristic impedance  $Z_m$  and microwave index  $n_\mu'$  of loaded line can be expressed as [4]

$$Z_m = \sqrt{\frac{L_0}{C_0 + C_L}} \quad (3.3.3)$$

$$n_\mu' = c \cdot \sqrt{L_0 \cdot (C_0 + C_L)} \quad (3.3.4)$$

For velocity match  $n_\mu'$  is set equal to  $n_{opt}$ , combine (3.3.3) and (3.3.4), the inductance (per unit length) of unloaded line  $L_0$  can be expressed as

$$L_0 = \frac{n_\mu' \cdot Z_m}{c} = \frac{n_{opt} \cdot Z_m}{c} \quad (3.3.5)$$

Equation (3.3.3) and (3.3.4) also indicate that the capacitance of loaded line should be

$$C_L + C_0 = \frac{n_{\mu}'}{c \cdot Z_m} = \frac{n_{opt}}{c \cdot Z_m} \quad (3.3.6)$$

Further, combining the equations from (3.3.1) to (3.3.4), the capacitance of unloaded line  $C_0$  and the loading capacitance  $C_L$  can be calculated respectively by

$$C_0 = \frac{n_{\mu}^2}{c \cdot Z_m \cdot n_{opt}} \quad (3.3.7)$$

$$C_L = \frac{n_{opt}^2 - n_{\mu}^2}{c \cdot Z_m \cdot n_{opt}} \quad (3.3.8)$$

Another useful equation shows the relationship between  $Z_m, n_{\mu}, Z_0, n_{\mu}'$  is

$$n_{\mu} \cdot Z_0 = n_{\mu}' \cdot Z_m \quad (3.3.9)$$

For impedance match, the  $Z_m$  should be  $50 \Omega$ , taking the optical index  $n_{opt}$  as 3.7 and the microwave index  $n_{\mu}$  of unloaded line as 2.6, using (3.3.8) the loading capacitance  $C_L$  should be 125 pF/m. It follows from (3.3.9), (3.3.5) and (3.3.7) that the unloaded  $Z_0$  should be  $71 \Omega$ , the unloaded capacitance 122 pF/m and the unloaded inductance 617 nH/m. This process is described in Fig. 3.14.

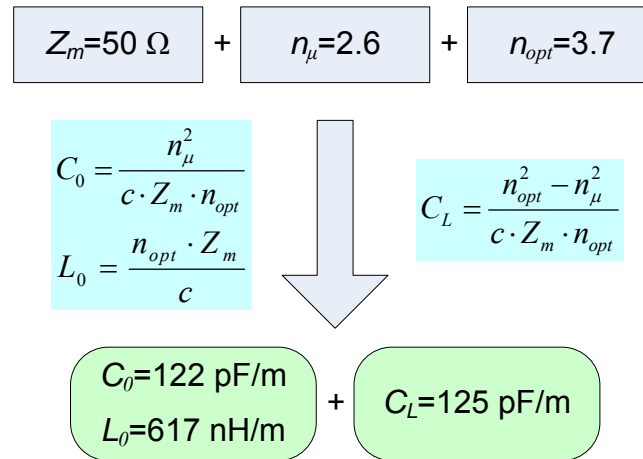


Fig. 3.14 Microwave design of the capacitively loaded TWE MZM

### 3.4 DEFINITION OF ELECTRICAL AND ELECTRO-OPTICAL BANDWIDTH

Bandwidth is one of those important factors which characterize the quality of a modulator.

The electro-optic bandwidth of a TWE MZM is defined as the frequency, for which the optical intensity modulation depth has fallen to 70.7% of the reference level, causing a 3 dB reduction in the received signal [4].

In electro-optic modulators, the amount of phase shift experienced by a photon from entering to exiting the waveguide is directly proportional to the voltage applied across the waveguide with the constant of proportionality containing parameters such as the waveguide dimensions, optical wavelength, index of refraction, overlap between the optical wave and the microwave, and the electro-optic coefficient. Since the applied voltage is of traveling-wave nature, the total amount of phase shift attained by a photon is cumulative of all phase shifts induced by the instantaneous voltage seen by the photon at a particular position on the line.

Fig. 3.15 shows a simplified equivalent circuit for a traveling-wave electrode modulator. In this model, the whole modulator is treated electrically as a transmission line.

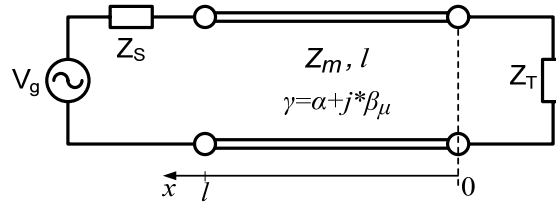


Fig. 3.15 Equivalent circuit of a traveling-wave electrode modulator

In this model, the modulating voltage at position  $x$  is given as [7,8]

$$V(x, \omega_m) = \frac{V_g}{2} \cdot (1 + \rho_1) \cdot e^{j\beta_{opt} \cdot l} \cdot \frac{e^{(\gamma - j\beta_{opt}) \cdot x} + \rho_2 \cdot e^{-(\gamma - j\beta_{opt}) \cdot x}}{e^{\gamma \cdot l} + \rho_1 \cdot \rho_2 \cdot e^{-\gamma \cdot l}} \quad (3.4.1)$$

where

$$\rho_1 = \frac{Z_m - Z_s}{Z_m + Z_s} \quad (3.4.1a)$$

$$\rho_2 = \frac{Z_T - Z_m}{Z_T + Z_m} \quad (3.4.1b)$$

$$\beta_{opt} = \frac{\omega_m}{c} \cdot n_{opt} \quad (3.4.1c)$$

$$\gamma = \alpha + j\beta_\mu \quad (3.4.1d)$$

$$\beta_\mu = \frac{\omega_m}{c} \cdot n_\mu \quad (3.4.1e)$$

The physical meaning of the variables in (3.4.1) is defined as follow

$V_g$  is the amplitude of the driving voltage,

$\omega_m$  is the modulation frequency,

$l$  is the traveling-wave electrode length,

$\rho_1$  is the input electrode structure reflection coefficient,

$\rho_2$  is the output electrode structure reflection coefficient,

$Z_m$  is the characteristic impedance of the modulator,

$Z_s$  is the source impedance, normally is 50  $\Omega$ ,

$Z_T$  is the terminating impedance ,

$\gamma$  is the complex microwave transmission constant,

$\alpha$  is the microwave attenuation constant,

$\beta_\mu$  is the microwave propagation constant of the signal in the electrode,

$\beta_{opt}$  is the optical propagation constant of the signal in the optical waveguide,

$n_\mu$  is the microwave refractive index,

$n_{opt}$  is the optical refractive index,

$c$  is the velocity of light in vacuum.

While under small signal modulation, the modulation depth is proportional to the modulating voltage, the modulation reduction factor  $r(x, \omega_m)$  can be defined as

$$r(x, \omega_m) = \left| \frac{V(x, \omega_m)}{V(l, 0)} \right| \quad (3.4.2)$$

As defined earlier, the electro-optic bandwidth of TWE MZM is the frequency, for which the optical intensity modulation reduction factor has fallen to 70.7% of the reference level. This can be expressed as

$$r(\omega_m) = \frac{1}{\sqrt{2}} \quad (3.4.3)$$

To simplify the analysis, the average voltage  $V_{avg}(\omega_m)$  can be used instead of  $V(x, \omega_m)$ , the modulation reduction factor can be simplified as [9]

$$r(\omega_m) = \left| \frac{V_{avg}(\omega_m)}{V_{avg}(0)} \right| \quad (3.4.4)$$

here  $V_{avg}(\omega_m)$  is the average voltage along a length of  $l$ . It can be expressed as [7,8]:

$$V_{avg}(\omega_m) = \frac{1}{l} \cdot \int_0^l V(x, \omega_m) dx = \frac{V_g \cdot (1 + \rho_1) \cdot e^{j\beta_{opt}l}}{2 \cdot (e^{\gamma l} + \rho_1 \cdot \rho_2 \cdot e^{-\gamma l})} \cdot (V_+ + \rho_2 \cdot V_-) \quad (3.4.5)$$

where

$$V_{\pm} = e^{\pm j\phi_{\pm}} \cdot \frac{\sin \phi_{\pm}}{\phi_{\pm}} \quad (3.4.5a)$$

$$\phi_{\pm} = \frac{(-j \cdot \gamma \mp \beta_{opt}) \cdot l}{2} \quad (3.4.5b)$$

$V_+$  is the single pass average voltage experienced by a photon due to the forward traveling sinusoidal voltage,

$V_-$  is the single pass average voltage experienced by a photon due to the reverse traveling sinusoidal voltage,

$\phi_+$  is the complex phase differential between the microwave and optical signals for a forward traveling sinusoidal voltage after propagating the length of the electrode

$\phi_-$  is the complex phase differential between the microwave and optical signals for a reverse traveling sinusoidal voltage after propagating the length of the electrode.

Inserting (3.4.5) into (3.4.4), we get

$$r(\omega_m) = \left| \frac{1 - \rho_1 \cdot \rho_2}{1 + \rho_2} \cdot \frac{V_+ + \rho_2 \cdot V_-}{e^{\gamma l} - \rho_1 \cdot \rho_2 \cdot e^{-\gamma l}} \right| \quad (3.4.6)$$

Note that, in this equation, the impedance mismatch, microwave loss and the velocity mismatch are all taken into consideration.

### Perfect impedance match

For a perfectly matched line, that is  $Z_m = Z_S = Z_T = 50 \Omega$ ,  $\rho_1$  and  $\rho_2$  are zero, which reduce (3.4.6) to the familiar expression of

$$r(\omega_m) = e^{\frac{-\alpha \cdot l}{2}} \cdot \left| \frac{\sin \phi_+}{\phi_+} \right| \quad (3.4.7)$$

$$\phi_+ = \frac{(-j \cdot \gamma - \beta_{opt}) \cdot l}{2} = \frac{l}{2} \cdot \left[ \frac{\omega_m}{c} (n_\mu - n_{opt}) - j \cdot \alpha \right] = \frac{\pi \cdot f_m \cdot l \cdot (n_\mu - n_{opt})}{c} - j \cdot \frac{\alpha \cdot l}{2} \quad (3.4.7a)$$

### Perfect impedance match + lossless

Further, if there is no microwave loss, that is  $\alpha=0$ , we get from (3.4.7)

$$r(\omega_m) = \left| \frac{\sin \phi_+}{\phi_+} \right| = \left| \frac{\sin \Delta}{\Delta} \right| \quad (3.4.8)$$

$$\Delta = \frac{\pi \cdot f_m \cdot l \cdot (n_\mu - n_{opt})}{c} \quad (3.4.8a)$$

Inserting (3.4.8) into (3.4.3), we get the electro-optic bandwidth

$$f_{3dB_{eo}} = \frac{1.39 \cdot c}{\pi \cdot l \cdot (n_\mu - n_{opt})} \quad (3.4.9)$$

This equation is well known as expressing the relationship between the bandwidth and the velocity mismatch. It is notable that this relationship is based on the premise that the device has a characteristic impedance of  $50 \Omega$  and the microwave loss of the whole device is neglected.

### Perfect impedance match + Perfect velocity match

If the velocities of microwave and optical wave have been perfectly matched, that is  $n_{opt} = n_\mu$ , we get from (3.4.7)

$$r(\omega_m) = e^{\frac{-\alpha \cdot l}{2}} \cdot \left| \frac{\sin\left(\frac{-j \cdot \alpha \cdot l}{2}\right)}{\frac{-j \cdot \alpha \cdot l}{2}} \right| \quad (3.4.10)$$

Using Euler's formula (see details in appendix B), (3.4.10) can be rewritten as

$$r(\omega_m) = \frac{1 - e^{-\alpha l}}{\alpha \cdot l} \quad (3.4.11)$$

Inserting (3.4.11) into (3.4.3), we get that at the frequency, for which the optical intensity modulation depth has fallen to 70.7% of the reference level

$$\alpha \cdot l = 0.7384 \quad (3.4.12)$$

And under this condition the electrical loss is [10]

$$20 \cdot \log |e^{-\gamma l}| = 20 \cdot \log(e^{-\alpha l}) = 20 \cdot \log(e^{-0.7384}) = -6.4 \text{ dB} \quad (3.4.13)$$

Under the condition that the velocity and the impedance are perfectly matched, we can determine the electro-optic 3 dB bandwidth by measuring the electrical loss, i.e.  $S_{21}$ . The frequency, for which the electrical loss of the whole modulator has fallen to -6.4 dB, can be taken as the 3 dB cut-off frequency of the electro-optical response.

### Velocity mismatch + Partly impedance match+ Microwave loss

Actually in a modulator the microwave loss and the velocity mismatch can be optimised but cannot be completely avoided. Consequently, it is necessary to analyse the frequency response of the modulator with both microwave loss and velocity mismatch. Another interesting thing in (3.4.6) is that, if  $\rho_1$  and  $\rho_2$  cannot simultaneously equal to zero, but if we can make  $\rho_2$  equal to zero, that is  $Z_m = Z_T$ , (3.4.7) is still valid. This condition is not so strict as the perfect impedance match, it can be done by terminating the modulator with a proper impedance, which is called "partly impedance match".

The (3.4.7) can be used here, further analysis shows that [10]

$$r(\omega_m) = e^{\frac{-\alpha l}{2}} \cdot \left| \frac{\sin \phi_+}{\phi_+} \right| = \left| e^{\frac{-\alpha l}{2}} \cdot \frac{\sin \phi_+}{\phi_+} \right| = \left| \frac{1 - e^{-(\alpha + j \cdot \beta_{opt}^\mu) l}}{(\alpha + j \cdot \beta_{opt}^\mu) \cdot l} \cdot e^{j \frac{\beta_{opt}^\mu \cdot l}{2}} \right| = \frac{\sqrt{e^{-2\alpha l} - 2 \cdot e^{-\alpha l} \cdot \cos(\beta_{opt}^\mu \cdot l) + 1}}{\sqrt{(\alpha \cdot l)^2 + (\beta_{opt}^\mu \cdot l)^2}} \quad (3.4.14)$$

$$\text{with } \beta_{opt}^\mu = \frac{\omega_m}{c} (n_\mu - n_{opt}) \quad (3.4.14a)$$

From (3.4.14), one can see that, to determine  $r(\omega_m)$ ,  $\alpha \cdot l$  and  $\beta_{opt}^\mu \cdot l$  should be known. As defined in (3.4.1),  $l$  is the TWE length;  $\alpha$  is the microwave attenuation constant, this parameter characterizes the microwave loss of the whole device and is a function of frequency;  $\beta_{opt}^\mu$  is defined in (3.4.14a), it characterizes the velocity mismatch in the modulator. The calculation of  $n_\mu$  and  $n_{opt}$  will be introduced in detail in Chapter 4.

In a TWE MZM, one can take the whole electrodes including outer electrodes and periodic capacitive loading with reverse bias voltage as a transmission line. Using the transmission line model, which has been explained in Chapter 2, the microwave loss coefficient of a modulator,  $\alpha$ , is the attenuation constant of the transmission line, consequently, combined with the scattering matrix of transmission line,  $\alpha$  can be expressed as

$$\exp(-\alpha \cdot l) = |S_{21}| \quad (3.4.15)$$

Inserting (3.4.15) into (3.4.14), it can be rewritten as

$$r(\omega_m) = \frac{\sqrt{|S_{21}|^2 - 2 \cdot |S_{21}| \cdot \cos(\beta_{opt}^\mu \cdot l) + 1}}{\sqrt{(\ln|S_{21}|)^2 + (\beta_{opt}^\mu \cdot l)^2}} \quad (3.4.16)$$

Since the scattering matrix can be obtained either in an EM simulation tool or by direct measurement using a network analyser, (3.4.16) is very useful both in design and in measurement to predict the electro-optic bandwidth of the TWE MZM.

### 3.5 DRIVING VOLTAGE $V_\pi$

The driving voltage,  $V_\pi$ , also called the half wave voltage or the switching voltage, is a very important parameter for an MZM. It is the voltage value at which the voltage-induced phase difference reaches  $\pi$  (or  $180^\circ$ ) in an MZM.

The phase difference  $\phi_1 - \phi_2$  in a MZM consists of two parts: one is the phase difference  $\Phi_0$  at zero applied voltage and the other is the phase difference  $\Delta\phi$  due to the applied voltage. If only one arm is modulated, the phase difference is [1]

$$\Delta\phi(V) = \gamma \cdot \Delta n(V) \cdot \frac{2\pi}{\lambda} \cdot l_{eff} \quad (3.5.1)$$

where  $\Delta n(V)$  is the optical index change in the waveguide active layer;  $\gamma$  is the optical confinement factor, defined as the portion of optical mode that is confined in the active layer,  $l_{eff}$  is the effective modulation length and is defined by

$$l_{eff} = l \cdot \eta \quad (3.5.2)$$

If the modulation is based on the LEO effect,  $\Delta n(V)$  can be described as [1]

$$\Delta n(V) = \frac{1}{2} \cdot n_0^3 \cdot r_{41} \cdot \frac{V}{d_{pin}} \quad (3.5.3)$$

where  $n_0$  is the optical index of the active layer at zero applied voltage;  $r_{41}$  is the relevant InP EO coefficient,  $V$  is the voltage applied vertically across the optical waveguide,  $d_{pin}$  is the depletion layer width of a reverse biased p-i-n junction.

Combining (3.5.1) and (3.5.3), one gets

$$\Delta\phi(V) = \frac{\pi}{\lambda} \cdot n_0^3 \cdot r_{ij} \cdot \frac{\gamma \cdot l_{eff}}{d_{pin}} \cdot V \quad (3.5.4)$$

and

$$V_\pi = \frac{\lambda}{n_0^3 \cdot r_{ij}} \cdot \frac{d_{pin}}{\gamma \cdot l_{eff}} \quad (3.5.5)$$

For MZMs using the QCSE, the relationship between  $\Delta n$  and  $V$  is nonlinear, but  $\Delta n$  is proportional to  $V$ , therefore (3.5.5) can be rewritten as

$$V_\pi \propto \frac{\lambda}{n_0^3 \cdot r_{ij}} \cdot \frac{d_{pin}}{\gamma \cdot l_{eff}} \quad (3.5.6)$$

## REFERENCES

- [1] K. Chang, "Handbook of optical components and engineering", Wiley, Hoboken, NJ (2003)
- [2] J. Yu, C. Rolland, D. Yevick, A. Somani, and S. Bradshaw, "A novel method for improving the performance of InP/InGaAsP multiple-quantum-well Mach-Zehnder modulators by phase shift engineering", Proc. IPRM'96 (Int. Conf. InP and Related Materials), paper 1TuG4-1, 376-379 (1996)
- [3] D. Penninckx and Ph. Delansay, "Comparison of the propagation performance over standard dispersive fiber between InP-based  $\pi$ -phase-shifted and symmetrical Mach-Zehnder modulators," IEEE Photon. Technol. Lett., **9**, 1250-1252 (1997)
- [4] R. G. Walker: "High-Speed III-V Semiconductor Intensity Modulators," IEEE J. Quantum Electron. **27**, 654-667 (1991)
- [5] L. B. Soldano and E. C. M. Pennings, "Optical multi-mode interference devices based on self-imaging: principles and applications", J. Lightwave Technol., **13**, 615-627 (1995)
- [6] C. Rolland, R. S. Moore, F. Shepherd, and G. Hillier, "10 Gbit/s, 1.56  $\mu\text{m}$  multiquantum well InP/InGaAsP Mach-Zehnder optical modulator," Electron. Lett. **29**, 471-472 (1993)
- [7] S. H. Lin and S. Y. Wang, "High throughput GaAs p-i-n electrooptic modulator with a 3dB bandwidth of 9.6 GHz at 1.3  $\mu\text{m}$ ," Appl. Opt. **26**, 1696-1700 (1987)
- [8] S. Y. Wang and S. H. Lin, "High speed III-V electrooptic waveguide modulators at  $\lambda=1.3 \mu\text{m}$ ," IEEE J. Lightwave Technol. **6**, 758-771 (1988)
- [9] I. Kim, M. R. T. Tan and S. Y. Wang, "Analysis of a new microwave low-loss and velocity-matched III-V transmission line for traveling-wave electrooptic modulators," IEEE J. Lightwave Technol. **8**, 728-738 (1990)
- [10] E. Voges and K. Petermann, "Optische kommunikationstechnik", Springer, Berlin (2002)

## Chapter 4

### Optimization towards Higher Speed and Lower Driving Voltage

The driving voltage and the 3 dB<sub>e0</sub> bandwidth are two important parameters for external modulators. It is difficult to achieve both parameters to their optimum. There is some trade-off during the optimization. For example, the 3 dB<sub>e0</sub> bandwidth and the driving voltage are inversely proportional to the effective modulation length and proportional to the i-region thickness when the device speed is limited by sample capacitance. In this Chapter, the simulation methods, tools and three different models as well as optimization strategies towards a low driving voltage 80 Gbit/s modulator will be discussed concretely.

#### 4.1 ELECTROMAGNETIC SIMULATION

The electromagnetic simulation plays an important role in modulator electrode design. Highly accurate design data are necessary for these devices because of the long and costly fabrication process. Hence a rigorous model is needed that includes the main limiting factors: the velocity mismatch between the optical wave and the microwave as well as the microwave loss.

##### 4.1.1 Introduction of High Frequency Structure Simulator

The high frequency structure simulator (HFSS) from Ansoft<sup>®</sup>, as an industry-standard software for S-parameter and full-wave SPICE extraction and for the electromagnetic simulation of high-frequency and high-speed components, is a high-performance full-wave electromagnetic (EM) field simulator for arbitrary three dimensional (3-D) volumetric passive device modeling. It integrates simulation, visualization, solid modeling, and automation in an environment where solutions to the 3-D EM problems are accurately obtained. All of the EM simulations involved in this work were carried out in HFSS (either in HFSS version9 or in HFSS version10).

HFSS employs the finite element method (FEM) and adaptive meshing to give an insight to the 3-D EM problems. The FEM originated as a method for modeling stress in structural mechanics applications, but was adapted to electromagnetics in the 1970s. Today, the FEM as a numerical method is well known in the electromagnetics and microwaves community, it can solve electromagnetic fields in structures with arbitrary boundary shape.

The FEM involves subdividing a large problem into individually simple constituent units which are each solvable via direct analytical methods, then reassembling the solution for the entire problem space as a matrix of simultaneous equations. In HFSS, the finite subsection (finite elements) over which they are defined, are contiguous and of the simplest possible shape. For an arbitrary 3-D problem they are tetrahedral volume elements. In HFSS, the mesh is the mapping of tetrahedral elements to the 3-D geometry for which a solution is desired.

Fig. 4.1 [1] shows the flow chart of the general design process of HFSS. The complete arbitrary 3-D geometry with material properties should be defined as the input for an EM simulation. In addition, boundary conditions specify the field behavior at the edges of the problem region and object interfaces.

To ensure an accurate simulation result as well as an acceptable calculation time, the solution criteria should be defined carefully. The more rigorous the criteria are, the more accurate results will be calculated. However, a considerable quantity of matrices will also be generated to fulfill the criteria due to the sharp increasing number of tetrahedra. This will directly lead to enormous calculations and an unacceptable calculating time, sometimes the relevant calculation can even exceed the capability of the calculating computer.

A normal simulation starts from generating the initial meshing data with respect to the electrical solution wavelength, the so-called lambda refinement results in tetrahedra of about  $\lambda/4$  in free space as the starting value. HFSS solves field equations derived from Maxwell's equations on the existing mesh. However, for many field

behaviors this may not be sufficient mesh density to properly solve for rapid fluctuations or extremely localized effects. Hence an adaptive refinement is followed. HFSS estimates the error in each element in the mesh, and refines those elements having the highest errors till the stopping criteria are met (cf. Fig. 4.2). The maximum delta-S is a frequently used convergence criterion. The delta-S is the magnitude of the change of the S-parameters between two consecutive passes. The value set for maximum delta-S is a stopping criterion for the adaptive solution. If the magnitude of the change of all S-parameters is less than this value from one iteration to the next, the adaptive analysis stops. Otherwise, it continues until the requested number of passes is completed. Here, the number of passes is a useful criterion to prevent the size of matrix used for the calculation exceeding the hardware limit. These two criteria are always used together in HFSS.

After the adaptive refinement, HFSS will use the established mesh data to solve the problem for the whole frequency range that has been defined by the designer. The frequency sweeping method used in the simulation can be chosen from one of three types, namely, discrete sweep, fast sweep or interpolating sweep.

Finally, the simulation results including EM fields and S-parameters as well as Y-matrices and Z-matrices could be plotted or expressed in tables or curves.

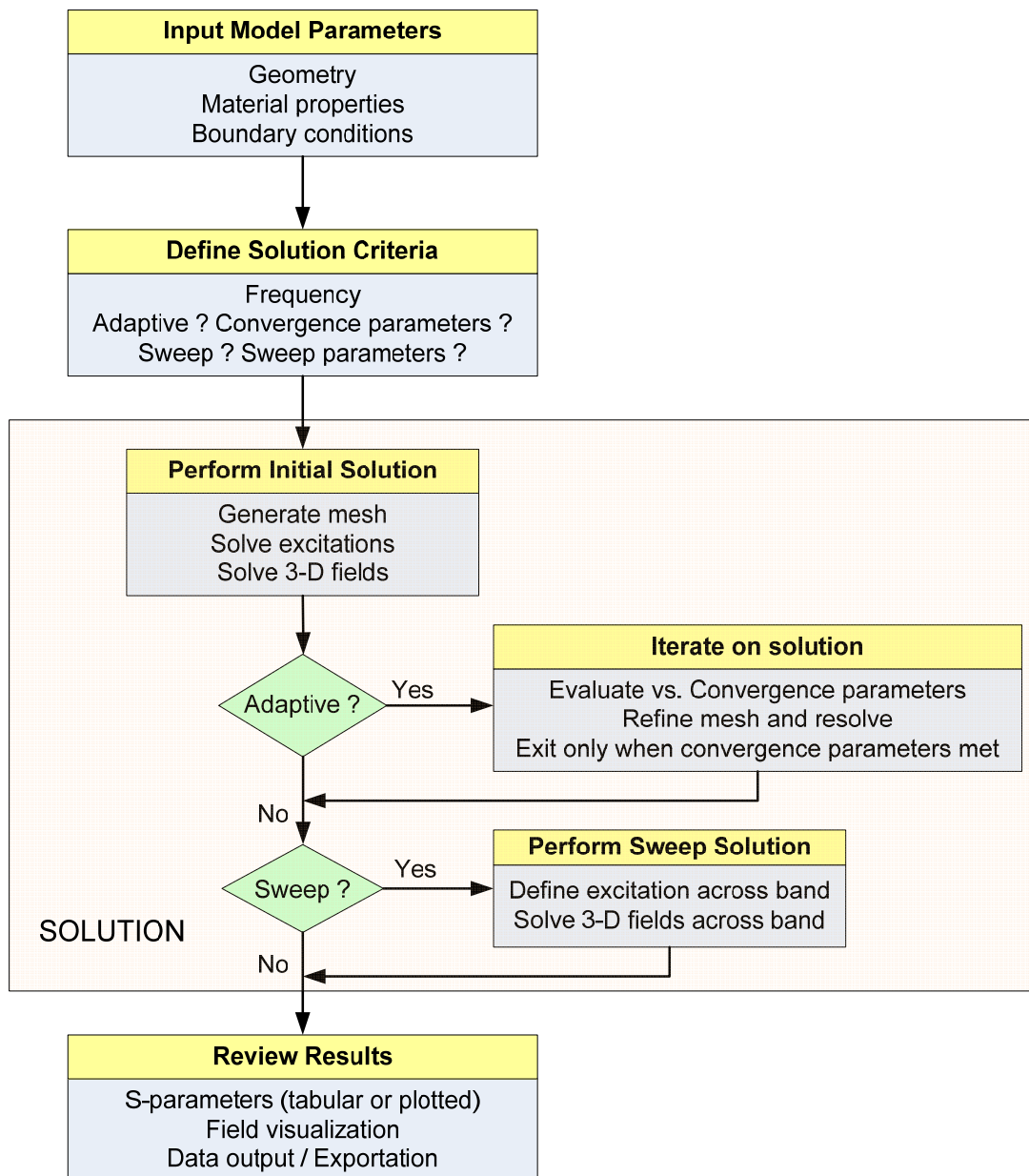


Fig. 4.1 Flow chart of general design process of HFSS

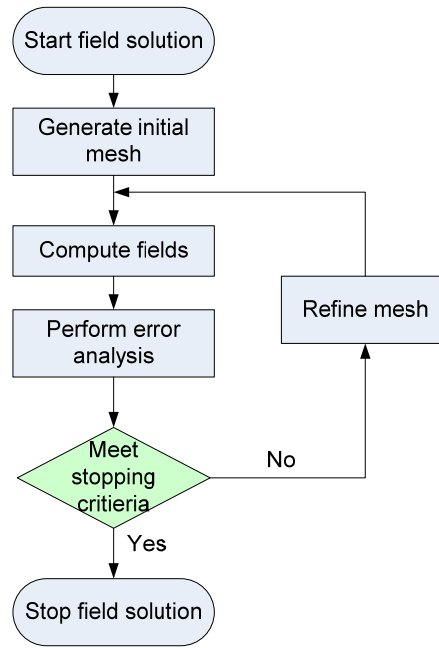


Fig. 4.2 Flow chart of the HFSS adaptive refinement process

#### 4.1.2 Modeling Modulator in HFSS

As shown in Fig. 4.1, the input model parameters include: material properties, geometry and boundary conditions. In this section, the modeling of desired Mach-Zehnder modulator in HFSS will be described in detail.

##### 4.1.2.1 Material Properties

Material properties in HFSS include relative permeability,  $\epsilon_r$ , relative permittivity,  $\mu_r$ , bulk conductivity,  $\sigma$ , dielectric loss tangent and magnetic loss tangent.

In the modulator model, the relative permittivity  $\mu_r$  for all the materials are set to 1, except for air whose  $\mu_r$  is set to 1.0000004 and gold whose  $\mu_r$  is set to 0.99996, both of them are defined by HFSS.

Bulk conductivity  $\sigma$  in HFSS as a bulk material loss factor is very important for semiconductor dielectric materials. In Mach-Zehnder modulators, the microwave losses of the electrodes are strongly dependent on this parameter. Hence this parameter should be carefully calculated for each layer's material in the model.

The conductivity of a material,  $\sigma$ , is defined with the current density  $\bar{J}$  and the applied electric field  $\bar{E}$  as [2]

$$\bar{J} \triangleq \sigma \bar{E} \quad (4.1.1)$$

Since the current density equals the product of the charge of the mobile carriers,  $\sigma$  can be expressed as a function of the electric field using the mobility [2].

$$\sigma = q\mu_e n + q\mu_h p \quad (4.1.2)$$

where  $q$  is the charge of the carrier,  $\mu_e$  and  $\mu_h$  are the electron and hole mobility in the semiconductor, and  $n$  and  $p$  are the electron and hole density, respectively.

Values for  $\mu_e$  and  $\mu_h$  of III-V compound materials such as InP, GaP, InAs and GaAs can be read out from table 4.1.

Table 4.1 Important physical properties of III-V compound materials [3]

III-V materials	InP	GaP	InAs	GaAs
Relative permeability $\varepsilon_r$	12.56	11.11	15.15	13.1
Electron mobility $\left[ \frac{\text{cm}^2}{\text{V} \cdot \text{s}} \right]$	$\mu_{e\_InP}$	$\mu_{e\_GaP}$	$\mu_{e\_InAs}$	$\mu_{e\_GaAs}$
	4600	110	33000	8500
Hole mobility $\left[ \frac{\text{cm}^2}{\text{V} \cdot \text{s}} \right]$	$\mu_{h\_InP}$	$\mu_{h\_GaP}$	$\mu_{h\_InAs}$	$\mu_{h\_GaAs}$
	150	75	460	400
Band gap $E_g$ [eV] @300K	1.344	2.272	0.354	1.424

The  $\mu_e$  and  $\mu_h$  of a quaternary compound  $\text{In}_{1-x}\text{Ga}_x\text{As}_y\text{P}_{1-y}$  can be calculated using (4.1.3) and (4.1.4) [4], respectively. The relation between  $x$  and  $y$  has been described by (2.3.1) in Chapter 2.

$$\mu_e(x, y) = \mu_{e\_InP}(1-x)(1-y) + \mu_{e\_GaP}x(1-y) + \mu_{e\_InAs}(1-x)y + \mu_{e\_GaAs}xy \quad (4.1.3)$$

$$\mu_h(x, y) = \mu_{h\_InP}(1-x)(1-y) + \mu_{h\_GaP}x(1-y) + \mu_{h\_InAs}(1-x)y + \mu_{h\_GaAs}xy \quad (4.1.4)$$

One should note that the electron and hole mobility are dependent on their density in the semiconductor [5, 6]. The  $\mu_e$  and  $\mu_h$  with corresponding  $n$  and  $p$  of each material used in modulator can be corrected using the data from table I in appendix B.

Table 4.2 gives the calculated material properties for modulator modeling by using (4.1.3), (4.1.4) and fundamental material properties in table 4.1.

Table 4.2 Calculated material properties for modulator modeling in HFSS

Materials	Doping type	Doping density	$\mu_h / \mu_e$ [cm <sup>2</sup> /Vs]	$\sigma$ [S/m]	$\epsilon_r$
InGaAs ( $\lambda=1650$ nm)	p	$1 \times 10^{19}$ cm <sup>-3</sup>	432	69183	13.9
InGaAsP ( $\lambda=1300$ nm)	p	$5 \times 10^{18}$ cm <sup>-3</sup>	322	25760	13.3
InP	p	$1 \times 10^{18}$ cm <sup>-3</sup>	150	2403	12.56
InP	p	$5 \times 10^{17}$ cm <sup>-3</sup>	150	1201	12.56
MQW	n.i.d.	-	-	0	12.56
InGaAsP ( $\lambda=1060$ nm)	n.i.d.	$<3 \times 10^{15}$ cm <sup>-3</sup>	-	0	13.0
InGaAsP ( $\lambda=1150$ nm)	n.i.d.	$<3 \times 10^{15}$ cm <sup>-3</sup>	10676	0	12.8
InGaAsP ( $\lambda=1060$ nm)	n	$1 \times 10^{18}$ cm <sup>-3</sup>	13770	220585	13.0
InP	n	$1 \times 10^{18}$ cm <sup>-3</sup>	2570	41120	12.56

In the modulator the p-contact is an Ohmic contact as discussed in section 2.5. Its resistivity is another important loss factor for the modulator and should be built into the modulator model. However, the p-contact is very thin, its thickness is of the order of 3 nm or less (as discussed in section 2.5), hence it is difficult to build the contact as a separate layer. An alternative way is integrating the contact resistance into p-layers, as described in Fig. 4.3. In the figure,  $d_{pi}$  ( $i=1$  to 4) is the thickness of each p-layer,  $d_p$  is the thickness of the whole p-region,  $w_p$  is the width of the p-area, and  $w_c$  is the p-contact's width.  $R_{pi}$  is the resistance of each p-layer and can be calculated by [2]

$$R_{pi} = \frac{d_{pi}}{\sigma_{pi} w_p \Lambda \eta} \quad (i = 1, 2, \dots) \quad (4.1.5)$$

where  $\sigma_{pi}$  is the conductivity for each p-layer, the product of  $\Lambda$  and  $\eta$  is the length of the whole p-region. Using (4.1.5) and (2.5.2), we get the whole p-region's resistance  $R_p$  including p-contact resistance and resistance of each p-layer as

$$R_p = \frac{\rho_c}{w_c \Lambda \eta} + \sum_{i=1}^4 \frac{d_{pi}}{\sigma_{pi} w_p \Lambda \eta} \quad (4.1.6)$$

Thus, the effective conductivity  $\sigma_p$  of the whole p-region can be calculated by

$$\sigma_p = \frac{d_p}{R_p w_p \Lambda \eta} \quad (4.1.7)$$

It serves as input parameter in HFSS. The calculated  $\sigma_p$  of p-region with different p-contact resistivity are listed in table 4.3.

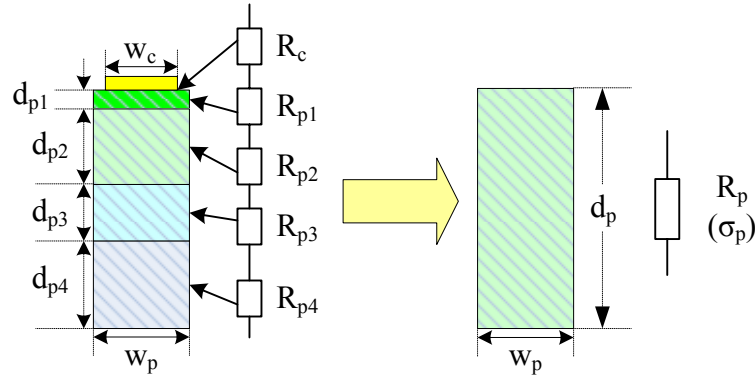


Fig. 4.3 Simplified p-layer in modulator modeling in HFSS

Table 4.3 Material properties of the p-region with different built-in p-contact resistivity

Material	Doping type	p-contact resistivity	$\sigma$ [S/m]	$\epsilon_r$
InP	p	$1 \times 10^{-4} \text{ cm}^2 \cdot \Omega$	75	12.6
	p	$3 \times 10^{-5} \text{ cm}^2 \cdot \Omega$	227	12.6
	p	$1 \times 10^{-5} \text{ cm}^2 \cdot \Omega$	538	12.6
	p	$3 \times 10^{-6} \text{ cm}^2 \cdot \Omega$	1034	12.6
	p	$1 \times 10^{-6} \text{ cm}^2 \cdot \Omega$	1404	12.6
	p	0	1709	12.6

In the modulator, the p-i-n junction is a bias dependent structure (explained in Chapter 2). Hence the bulk conductivity  $\sigma$  and the depletion width in n-region ( $x_n$ ) and p-region ( $x_p$ ) of the p-i-n structure are also bias dependent. The simulation results will be accurate only when  $\sigma$ ,  $x_n$  and  $x_p$  are set to the values which correspond to those in the measurement setup or the system application. The C-V measurement is used to determine the thickness of the intrinsic layer at different bias conditions. The carrier concentration in each layer is determined with the aid of simulation in APSYS. Fig. 4.4 is such a simulation result. Here, to simplify the analysis, a bulk intrinsic layer is used instead of the real MQW structure.

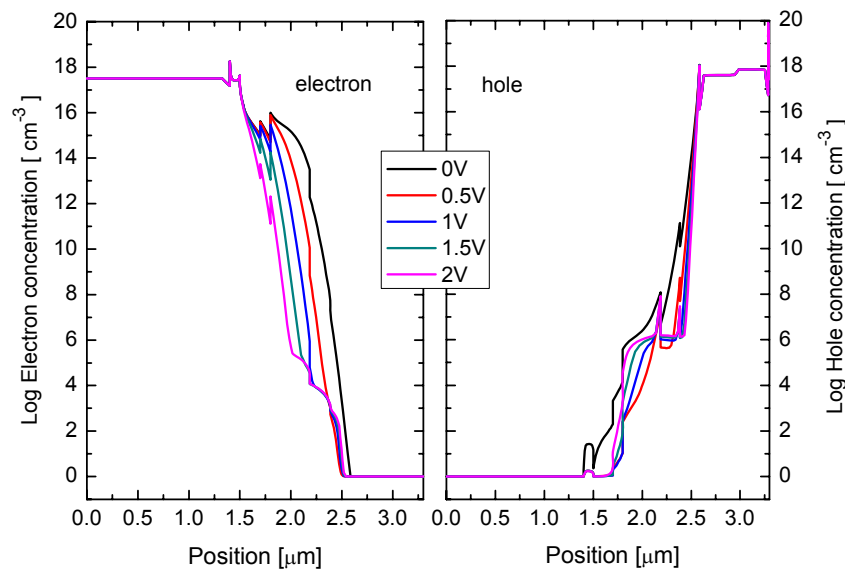


Fig. 4.4 Carrier concentration of different layers in modulator with varied bias [7]

#### 4.1.2.2 Geometry and Corresponding Boundary Conditions

The simplest way of modeling a modulator in HFSS is drawing a 3-D geometry as the real modulator chip (cf. Fig. 4.5). However, due to the geometry size, especially the repetitive inner electrodes and complicated p-i-n structures, the solution time for such a model is always very long.

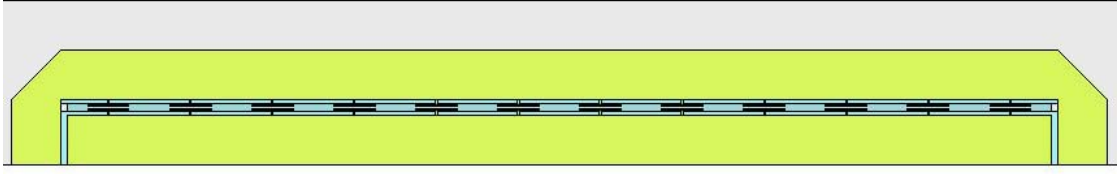


Fig. 4.5 Top-view of a whole chip modulator model with 12 sections in HFSS

Due to its intrinsic periodical property, the whole modulator can be divided into  $N$  sections as shown in Fig. 4.6. In order to shorten the computation time, one can simulate one of these sections in HFSS and utilize the transfer-matrix method to calculate the scattering matrix for the whole device. Because the number of tetrahedra during the simulation is proportional to the number of the sections, simulating only one section means the size of the calculating matrix is much smaller. Thus, one can not only shorten the simulation time but also improve the simulation accuracy without upgrading the hardware of the simulating computer because the simulation accuracy is predominantly limited by available memory and disk space for storage and solution of the problem matrix in HFSS.

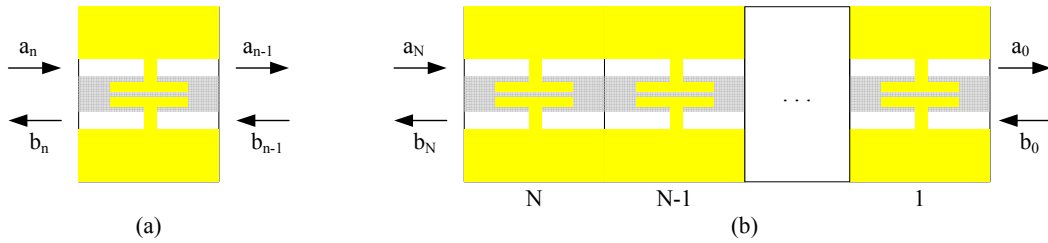


Fig. 4.6 (a) A section of modulator (b) An  $N$ -section segmented modulator

The transfer matrix,  $T$ , for one section is defined as (4.1.8), and for the whole modulator the transfer matrix can be written as (4.1.9).

$$\begin{pmatrix} a_n \\ b_n \end{pmatrix} = T \begin{pmatrix} a_{n-1} \\ b_{n-1} \end{pmatrix} \quad (4.1.8)$$

$$\begin{pmatrix} a_N \\ b_N \end{pmatrix} = \prod_{i=1}^N T \cdot \begin{pmatrix} a_0 \\ b_0 \end{pmatrix} = T^N \cdot \begin{pmatrix} a_0 \\ b_0 \end{pmatrix} \quad (4.1.9)$$

While HFSS can not directly export the T-matrix, one should transform the exported scattering matrix of a modulator section to the T-matrix by using:

$$T = \frac{1}{S_{21}} \begin{bmatrix} 1 & -S_{22} \\ S_{11} & S_{12}S_{21} - S_{11}S_{22} \end{bmatrix} \quad (4.1.10)$$

Finally, one can transform the  $T^N$  back to the scattering matrix using (4.1.11). Because of its symmetry and reciprocity, we have (4.1.12).

$$S_{21}^N = \frac{1}{T_{11}^N}, \quad S_{11}^N = \frac{T_{21}^N}{T_{11}^N} \quad (4.1.11)$$

$$S_{21}^N = S_{12}^N, \quad S_{11}^N = S_{22}^N \quad (4.1.12)$$

This process can also be done by using software Ansoft Designer SV (student version). Fig. 4.7 shows an example, which is a 2-port network with 8 identical cells, and each cell is defined by a touchstone file exported from HFSS. This 2-port network can be easily changed to an N-cell one.

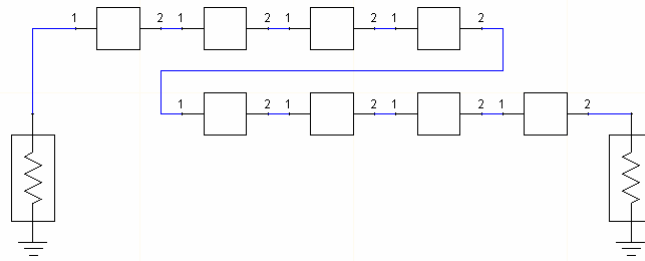


Fig. 4.7 An 8-cell 2-port network in Ansoft Designer

Fig. 4.8 shows the single-section modulator model in HFSS, top-view and side-view, respectively. It can be found that this model is actually only a half part of the Fig. 4.6(a). A symmetric boundary in HFSS enables one to model only a half part of the structure, which reduces the size or complexity of the design, thereby shortening the solution time. Here a “perfect E” boundary is used in the model to represent the odd mode for the traveling-wave electrode as shown in Fig. 4.9.

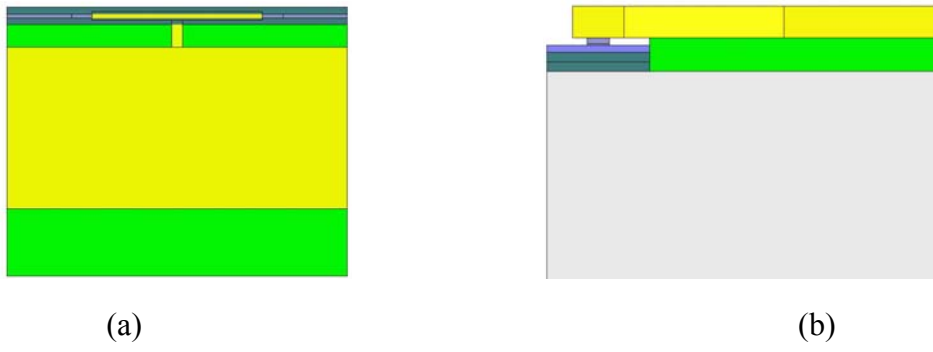


Fig. 4.8 (a) Top-view (b) Side-view of a single-section modulator model in HFSS

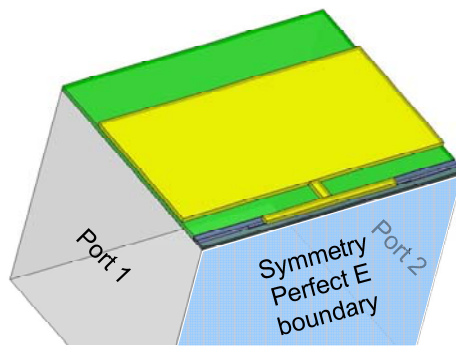


Fig. 4.9 A 3-D view of a single-section modulator model with excitation and boundary condition

### 4.1.3 Simulation Results

Fig. 4.10 shows the simulated insertion loss of a modulator with the following parameters:  $A=250\ \mu\text{m}$ ,  $\eta=0.4$ ,  $\text{bias}=-2\ \text{V}$ . To verify the accuracy of the simulation results, we compare the measured curve (red one in Fig. 4.10) with the simulated one (black one in Fig. 4.10). The frequency sweep in the simulation is from 0.5 GHz to 100 GHz with a step size of 0.5 GHz. The measurement (described in Chapter 6 in detail) is limited to 70 GHz due to the probe head. Obviously, the simulation fits well to the measurement, which confirms the success of modeling in HFSS.

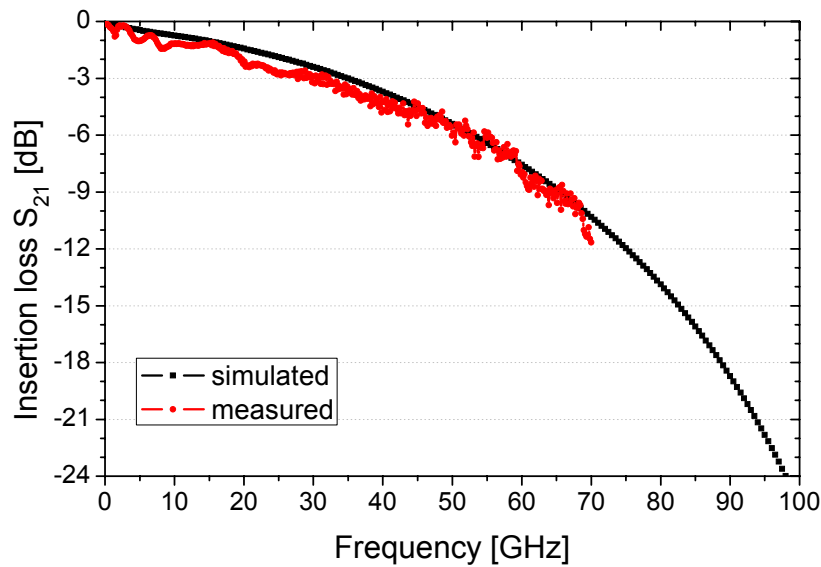


Fig. 4.10 Comparison between measured and simulated electrical insertion loss  $S_{21}$  of the same modulator structure

## 4.2 THE SIMPLE CIRCUIT MODEL FOR THE MODULATOR

The microwave design method that has been introduced in section 3.3 and the analysis of the bandwidth introduced in section 3.4 provides a rough guideline for the capacitively loaded traveling-wave electrode design. The modulation frequency response of such a device is limited not only by the impedance mismatch, the velocity mismatch and the microwave loss, but also by the microwave dispersion, filtering effects due to periodic capacitive loading and various parasitic effects. To analyze the frequency response including all these effects, an electric model is needed.

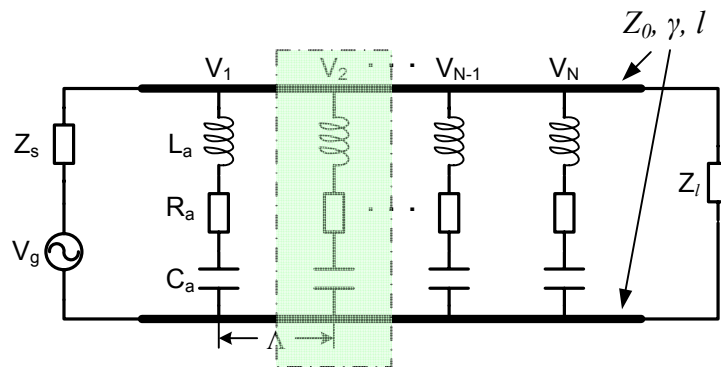


Fig. 4.11 Microwave equivalent model for the TWE MZM

Figure 4.11 shows a model, in which a microwave equivalent circuit model for the active electrodes is combined with a transmission line model. Traveling-wave electrodes are here still characterized by the following parameters: complex propagation parameter  $\gamma$ , characteristic impedance  $Z_0$  and length  $l$  as shown in Fig. 2.6. As the periodic loading of the TWEs, the active electrode with its connection to TWE is characterized by lumped electrical elements: the inductance  $L_a$  is induced by the air-bridge which connects the inner active electrode and outer traveling-wave electrode; the resistance  $R_a$  includes all series parasitic resistances in active electrode; the capacitance  $C_a$  is the junction capacitance of reverse biased p-i-n junction. In a TWE MZM, it is the voltage across the capacitance  $C_a$  that does the actual modulation. The

TWE length between two adjacent bridges is  $\Lambda$ , this is also the period length of a segment of TWE. The microwave source impedance  $Z_s$  and the termination impedance  $Z_l$  are typically  $50 \Omega$ .

If one uses a transmission matrix to describe the cell as shown in Fig. 4.12, this matrix can be expressed as (4.2.1). Further calculation gives the expressions (4.2.2) for each element of the matrix. Since the cell is reciprocal, we have (4.2.3).

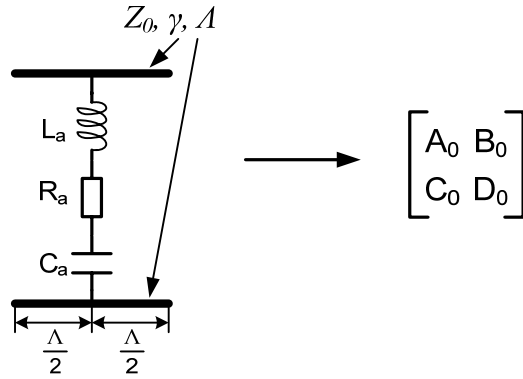


Fig. 4.12 One cell of the modulator and its transmission matrix

$$\begin{bmatrix} A_0 & B_0 \\ C_0 & D_0 \end{bmatrix} = \begin{bmatrix} \cosh\left(\frac{\gamma \cdot \Lambda}{2}\right) & Z_0 \sinh\left(\frac{\gamma \cdot \Lambda}{2}\right) \\ \frac{1}{Z_0} \sinh\left(\frac{\gamma \cdot \Lambda}{2}\right) & \cosh\left(\frac{\gamma \cdot \Lambda}{2}\right) \end{bmatrix} \cdot \begin{bmatrix} 1 & 0 \\ Y & 1 \end{bmatrix} \cdot \begin{bmatrix} \cosh\left(\frac{\gamma \cdot \Lambda}{2}\right) & Z_0 \sinh\left(\frac{\gamma \cdot \Lambda}{2}\right) \\ \frac{1}{Z_0} \sinh\left(\frac{\gamma \cdot \Lambda}{2}\right) & \cosh\left(\frac{\gamma \cdot \Lambda}{2}\right) \end{bmatrix}$$

$$\text{with } Y = \frac{1}{R_a + j \cdot \omega \cdot L_a + \frac{1}{j \cdot \omega \cdot C_a}}$$

(4.2.1)

$$A_0 = D_0 = \cosh(\gamma \cdot \Lambda) + \frac{j \cdot \omega \cdot C_a \cdot Z_0}{2 \cdot (1 + j \cdot \omega \cdot C_a \cdot R_a - \omega^2 \cdot L_a \cdot C_a)} \cdot \sinh(\gamma \cdot \Lambda)$$

$$B_0 = Z_0 \cdot \left[ \left( \frac{j \cdot \omega \cdot C_a \cdot Z_0}{2 \cdot (1 + j \cdot \omega \cdot C_a \cdot R_a - \omega^2 \cdot L_a \cdot C_a)} \right) \cdot (-1 + \cosh \gamma \cdot \Lambda) + \sinh(\gamma \cdot \Lambda) \right] \quad (4.2.2)$$

$$C_0 = \frac{1}{Z_0} \left[ \left( \frac{j \cdot \omega \cdot C_a \cdot Z_0}{2 \cdot (1 + j \cdot \omega \cdot C_a \cdot R_a - \omega^2 \cdot L_a \cdot C_a)} \right) \cdot (1 + \cosh \gamma \cdot \Lambda) + \sinh(\gamma \cdot \Lambda) \right]$$

$$A_0 \cdot D_0 - B_0 \cdot C_0 = 1 \quad (4.2.3)$$

The transmission matrix of the whole modulator as illustrated in Fig. 4.13 can be obtained by multiplying the transmission matrices of all segments as (4.2.4). The calculation of the transmission matrix has already been shown in (2.2.20) and (2.2.21) and will not be repeated here.

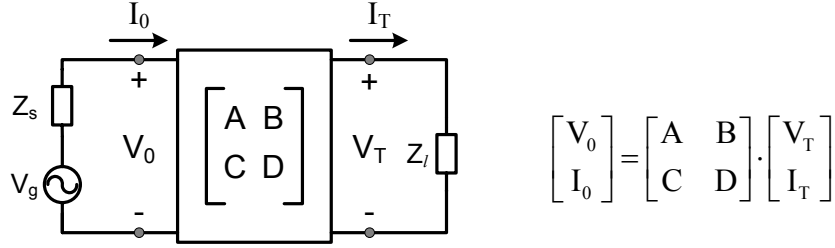


Fig. 4.13 Transmission matrix representation of TWE MZM

$$\begin{bmatrix} A & B \\ C & D \end{bmatrix} = \begin{bmatrix} A_0 & B_0 \\ C_0 & D_0 \end{bmatrix}^N \quad \text{with } N = \frac{l}{\Lambda} \quad (4.2.4)$$

The modulation voltage across the  $n$ th capacitor  $C_a$  is just  $V_n$  multiplied by a factor of  $\frac{1}{R_a + j \cdot \omega \cdot L_a + \frac{1}{j \cdot \omega \cdot C_a}} = \frac{1}{1 - \omega^2 \cdot L_a \cdot C_a + j \cdot \omega \cdot R_a \cdot C_a}$ . The microwave phase factor of at the  $n^{\text{th}}$  segment due to the traveling time of the modulated optical wave packet is  $e^{j \cdot \omega \cdot \frac{(0.5+n) \cdot \Lambda}{v_{opt}}}$ . In order to normalize the frequency response, we consider the ideal case when all the modulation voltages are equal to the input microwave voltage  $\frac{V_g}{2}$ . Taking  $\frac{N \cdot V_g}{2}$  as the normalization constant for the summation of the voltage, the normalized frequency response of the segmented TWE MZM can be expressed as [8]

$$M(\omega) = \left| \frac{2}{N \cdot V_g} \cdot \sum_{n=1}^N V_n \cdot e^{j \cdot \omega \cdot \frac{(0.5+n) \cdot \Lambda}{v_{opt}}} \cdot \frac{1}{1 - \omega^2 \cdot L_a \cdot C_a + j \cdot \omega \cdot R_a \cdot C_a} \right|^2 \quad (4.2.5)$$

where  $V_n$  ( $n = 1$  to  $N$ ) is the voltage across the loading segments as illustrated in Fig. 4.11 and can be easily calculated using transmission matrix method. Note that, (4.2.5) is straightforward and can be calculated by computer aided mathematical tools.

### 4.3 DETERMINING THE PARAMETERS FOR THE CIRCUIT MODEL

In the last section, a microwave equivalent circuit model for the modulator has been developed. To use this circuit model, one should determine each parameter. This section will explain how to extract each parameter of the modulator by measurements or simulations.

#### 4.3.1 $L_0$ and $C_0$ of the CPS

As explained in section 2.2,  $L_0$  and  $C_0$  are per unit length quantities of series inductance and shunt capacitance for CPS, respectively. They can be calculated by (2.2.16), while propagation parameter  $\gamma$  and the characteristic impedance  $Z_0$  can be obtained directly from HFSS as standard outputs for a 3-D structure. Fig. 4.14 shows the calculated  $L_0$  and  $C_0$  for an unloaded CPS with  $w=120 \mu\text{m}$  and  $s=60 \mu\text{m}$  ( $w$  and  $s$  are defined in Fig. 2.2).

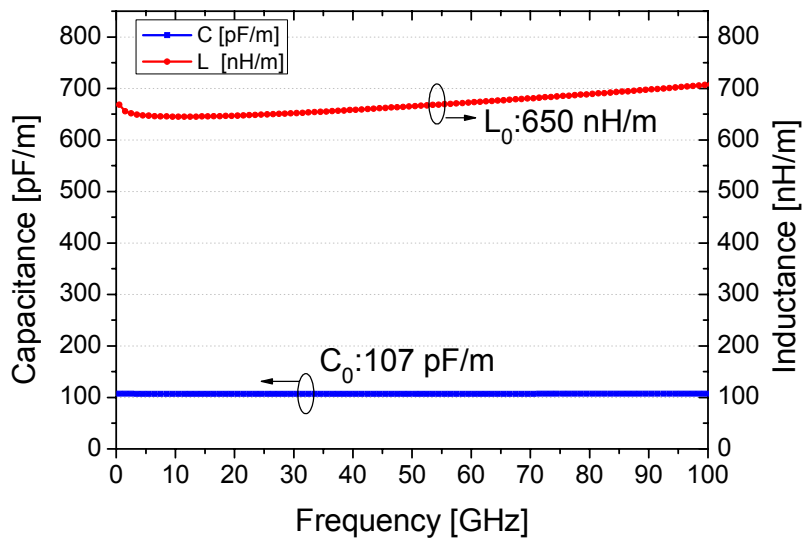


Fig. 4.14 Calculated  $L_0$  and  $C_0$  for an unloaded CPS

### 4.3.2 Capacitance of the p-i-n Diode $C_{pin}$

The capacitance of the p-i-n diode is an important parameter in modulator design, and its value can be acquired directly by C-V measurement (details in Section 6.1). In order to avoid the influence of parasitic capacitances in the modulator, a series of extra circular test p-i-n diodes with different diameters are made on the modulator wafer.

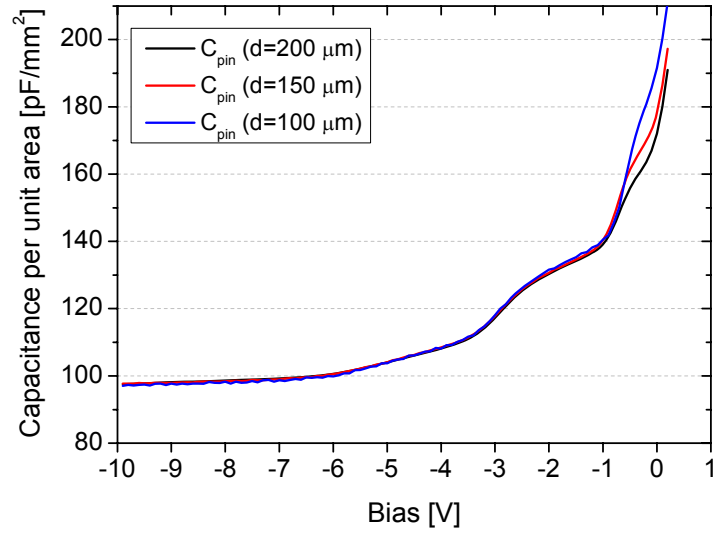


Fig. 4.15 Measured bias dependent capacitance of circular p-i-n diodes

Fig. 4.15 shows the measured capacitance of circular test p-i-n diodes. The curves become flat when the bias is smaller than -6 V.  $C_{pin}$  is about 100 pF/mm<sup>2</sup> with the bias of -6 V.

### 4.3.3 The Inductance of the Air Bridge in the Modulator

The air bridges in the modulator connect the outer traveling-wave electrode and the inner segmented electrodes. It is impossible to measure their value for such a short metal. For an air-bridge length of  $l_b$ , diameter  $d_b$ , the air-bridge's inductance is given by [9]

$$L_b = \frac{\mu_0 l_b}{2\pi} \left\{ \ln \left[ \left( \frac{2l_b}{d_b} \right) + \sqrt{1 + \left( \frac{2l_b}{d_b} \right)^2} \right] + \frac{d_b}{2l_b} - \sqrt{1 + \left( \frac{d_b}{2l_b} \right)^2} + \mu_r \delta \right\} \quad (4.3.1)$$

here  $\delta$  is the skin effect factor and is a function of wire diameter and frequency. A close approximation of  $\delta$  is given by [9]

$$\delta = 0.25 \tanh\left(\frac{4d_s}{d_b}\right) \quad (4.3.2)$$

here  $d_s$  is the skin depth of the air bridge's material and is defined by [10]

$$d_s = \sqrt{\frac{\rho}{\pi f \mu_0 \mu_r}} \quad (4.3.3)$$

Calculated air-bridge's inductance  $L_b$  is about 0.01 nH, with  $l_b=24 \mu\text{m}$  and  $d_b=5 \mu\text{m}$ .

#### 4.3.4 Parasitic Capacitance in the Modulator

The parasitic capacitance in the modulator cannot be neglected, especially in the active area. Fig. 4.16 shows a SEM (Scanning electron microscope) photo of inner electrodes in the active area. From the photo, one can find that the inner electrode's width  $w_e$  is not equal to the optical waveguide's width  $w_{wg}$  as the design. Actually, the inner electrode is wider than the optical waveguide, that is,  $w_e > w_{wg}$ . This causes the parasitic capacitance  $C_{s1}$  and the fringing capacitance  $C_{s2}$ , as shown in Fig. 4.17.

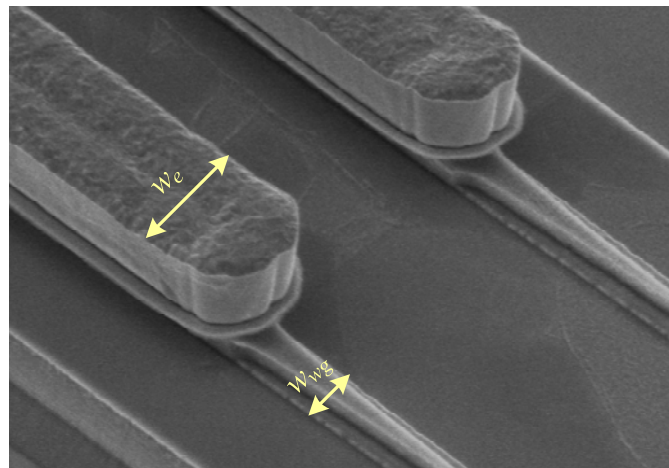


Fig. 4.16 SEM photo of inner electrodes of the modulator

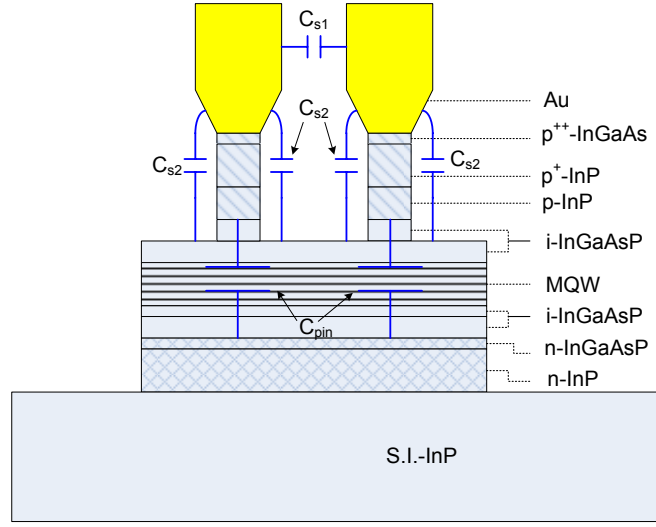


Fig. 4.17 Parasitic capacitance in the active area of a modulator

It is difficult to determine the value of each parasitic capacitance, however, if we define the loading capacitance per unit length of the CPS,  $C_L$ , as

$$C_L = \frac{\eta}{2} \cdot (C_{pin} \cdot w_{wg} + C_s) \quad (4.3.4)$$

then the parasitic capacitance per unit length,  $C_s$ , is

$$C_s = \frac{2 \cdot C_L}{\eta} - C_{pin} \cdot w_{wg} \quad (4.3.5)$$

$C_{pin}$  can be obtained by measurement, and its value is around 100 pF/mm<sup>2</sup> at -6V bias as explained in the former section. Fill factor  $\eta$  is an appointed design parameter. The loading capacitance of the CPS  $C_L$  can be calculated by

$$C_L = \left[ \left( \frac{n'_\mu}{n_\mu} \right)^2 - 1 \right] \cdot C_0 \quad (4.3.6)$$

From the measured S-parameters of the test CPS structure, we have  $L_0 = 650$  nH/m  $C_0 = 107$  pF/m  $n_\mu = 2.5$  .

From the measured S-parameters of a modulator chip of  $\Lambda = 250$   $\mu\text{m}$  ,  $\eta = 0.4$  , and  $w_{wg} = 2.8$   $\mu\text{m}$  with a -6 V bias voltage, we have  $n'_\mu = 3.6$  . And taking the measured capacitance of the reverse biased p-i-n structure  $C_{pin} = 100$  pF/mm<sup>2</sup> , we get  $C_s = 294$  pF/m .

### 4.3.5 The Resistances in the Active Area of a Modulator

As shown in Fig. 4.18, in the active area of a modulator, there are p-contact resistance, bulk resistance of p-doped layers and bulk resistance of n-doped layer. Note that the current direction of the n-doped layer is different from that of the p-doped layer. The calculation of the bulk resistance of the p-layer has been introduced in section 4.1. The bulk resistance of the n-layer can be calculated by

$$R_n = \frac{d}{\sigma_n \cdot d_n \cdot \Lambda \cdot \eta} \quad (4.3.7)$$

where  $d$  is the center to center distance between the two inner electrodes,  $d_n$  is the thickness of the n-layer. The resistance of the p-contact can be calculated only when contact resistivity  $\rho_c$  is known. Here,  $\rho_c = 3 \times 10^{-5} \Omega \cdot \text{cm}^2$ . The measurement of the contact resistivity will be introduced in section 6.2. The calculated resistances in the active area of the modulator with  $\Lambda$  of  $250 \mu\text{m}$  and  $\eta$  of 0.4 are listed in table 4.4.

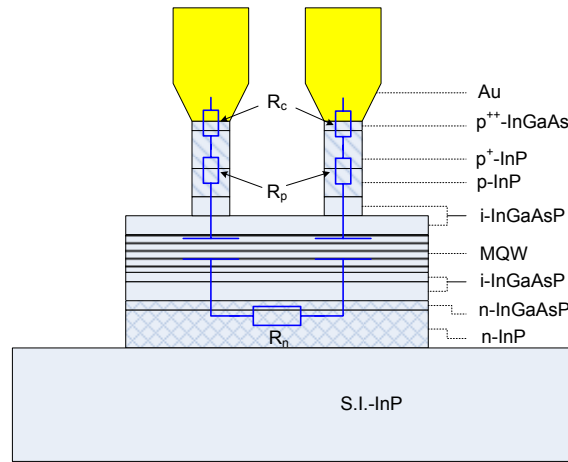


Fig. 4.18 The resistances in the active area of a modulator

Table 4.4 Calculated resistances in the active area of the modulator

	$R_c$	$R_{p1}$	$R_{p2}$	$R_{p3}$	$R_{p4}$	$R_n$
Resistance ( $\Omega$ )	10.714*	$4.13 \times 10^{-4}$	$6.93 \times 10^{-4}$	0.446	1.189	13.548

\* The corresponding p-contact resistivity  $\rho_c$  is  $3 \times 10^{-5} \Omega \cdot \text{cm}^2$ .

#### 4.4 DETAILED CIRCUIT MODEL AND SIMULATION RESULTS

The modeling of the traveling-wave modulator's frequency response introduced in section 4.2 is simple and straightforward. However, the model is too simple if one wants to analyze the modulator in detail. To resolve this problem, a detailed model will be given in this section. Almost all the microwave loss factors in the modulator are taken into account in this new detailed model and can be tuned individually.

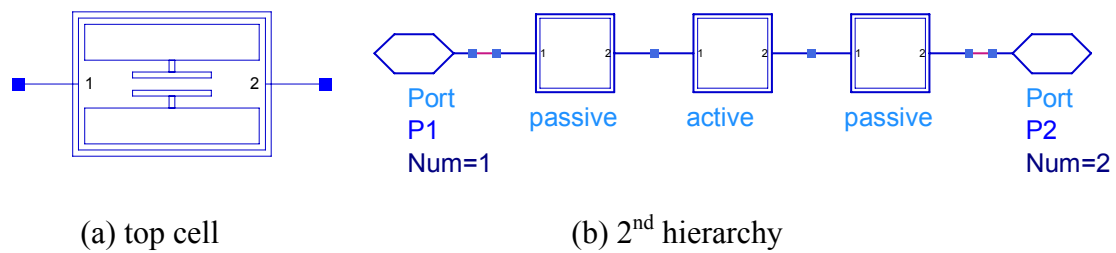


Fig. 4.19 The hierarchical model for one section of a modulator in an EDA tool

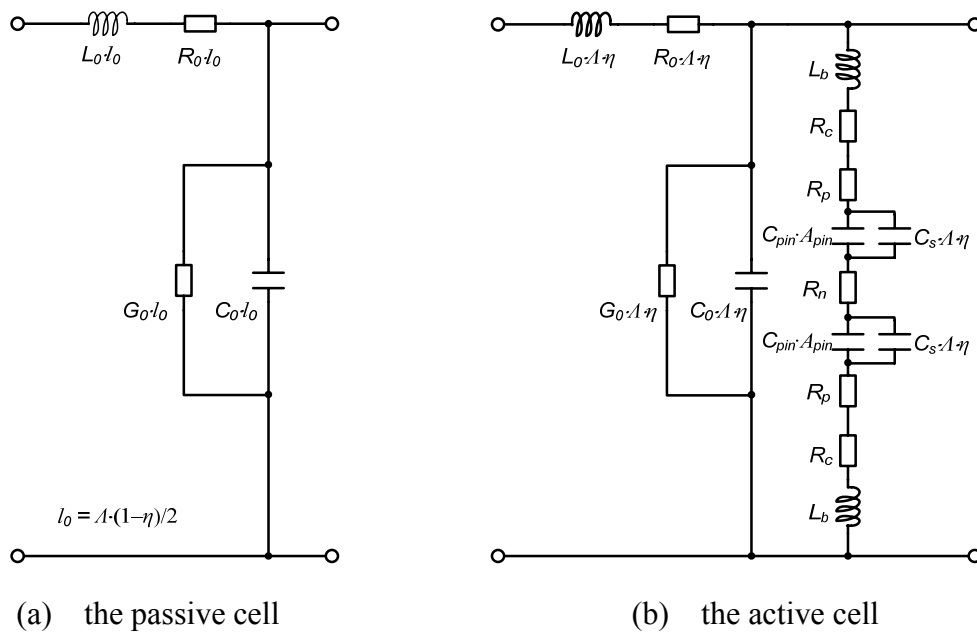


Fig. 4.20 Circuit models of passive part and active part in a section of the modulator

As shown in Fig. 4.19, in the new detailed model, every section of the modulator is divided into three circuit cells, two of them are identical passive cells and

one is the active cell. The passive cell is actually the lumped circuit of a transmission line as shown in Fig. 4.20(a). It describes the beginning and the end part of a section, where the CPS has no load. The active cell (cf. Fig. 4.20(b)) describes the part where the CPS has the lossy capacitive load. The values of the parameters used in the model have all been calculated in the previous section.

The circuit model is inserted hierarchically in a simulation tool called ADS. Fig. 4.21 is a 12-section TWE MZM circuit in ADS. The S-parameter analysis is made up to 70 GHz with a stepwidth of 0.05 GHz. As shown in Fig. 4.22 and Fig. 4.23, the simulation results fit well to the experimental results. Fig. 4.22(a) shows the simulation result of the modulator with following parameters:  $l=3\text{mm}$ ,  $A=250\mu\text{m}$ ,  $\eta=0.4$ . The corresponding experimental result is the measured  $S_{21}$  of chip C61 from our wafer #45. Fig. 4.22(b) shows the simulation result of the modulator with the same parameters except  $\eta = 0.5$ . The corresponding experimental result is from C63 of our wafer #45.

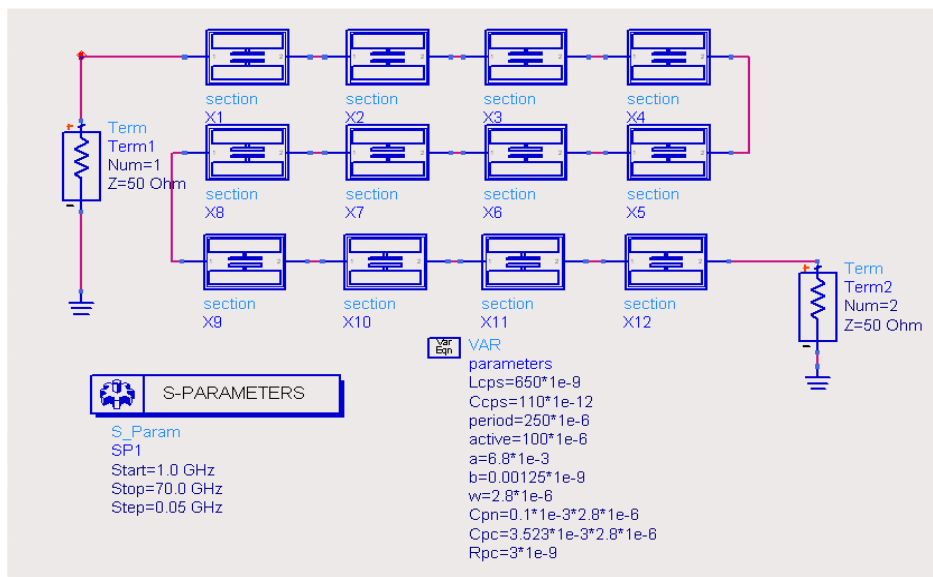
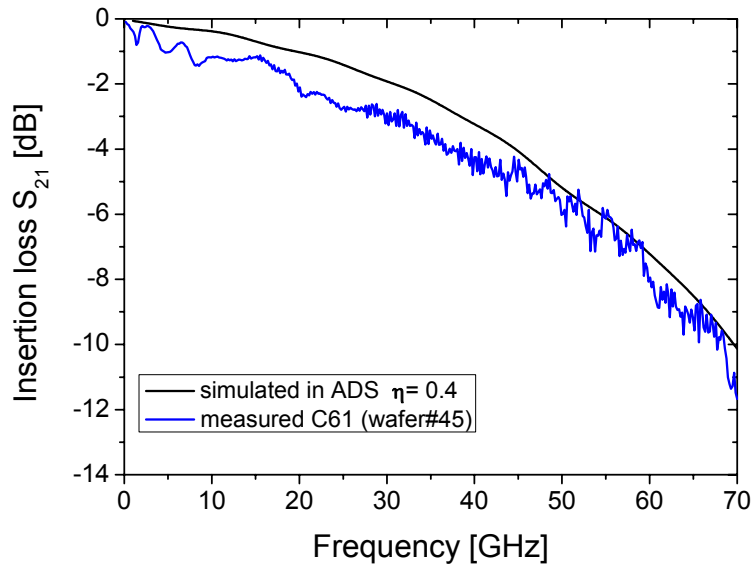
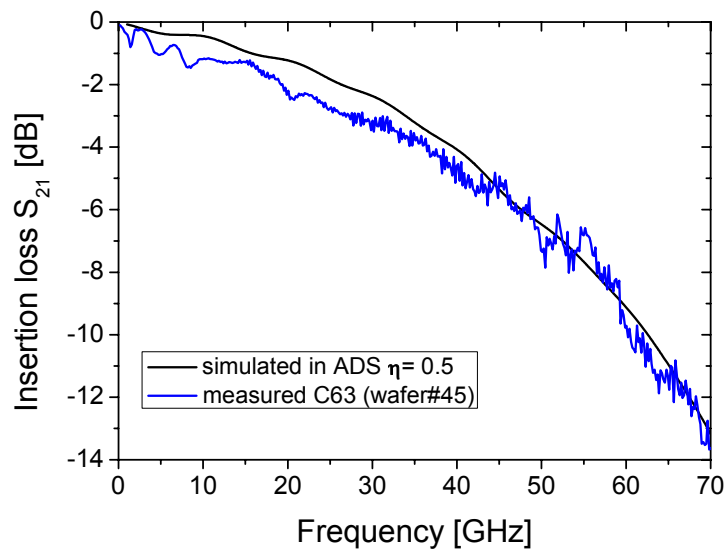


Fig. 4.21 12-section TWE MZM model in ADS



(a) Simulation result vs. experimental result (#45C61)



(b) Simulation result vs. experimental result (#45C63)

Fig. 4.22 Simulation results using the detailed model

#### 4.5 BRAGG FREQUENCY

The periodic structure of capacitive loads constitutes a Bragg grating which gives an upper limit for the modulator bandwidth [11, 12]

$$f_{Bragg} = \frac{1}{\pi \cdot \Lambda \cdot \sqrt{L_0 \cdot (C_0 + C_L)}} \quad (4.5.1)$$

Combining (4.5.1) and (4.3.4), we get

$$f_{Bragg} = \frac{1}{\pi \cdot \Lambda \cdot \sqrt{L_0 \cdot \left[ C_0 + \frac{\eta}{2} \cdot (C_{pin} \cdot w_{wg} + C_s) \right]}} \quad (4.5.2)$$

Values for the unloaded TWEs derived from test structures are  $L_0=650$  nH/m and  $C_0=107$  pF/m.  $C_{pin}=100$  pF/mm<sup>2</sup> at -6 V bias voltage, the calculated  $C_s = 294$  pF/m. The designed value of  $w_{wg}$  is  $2.8$   $\mu$ m. Using (4.5.2) we get  $f_{Bragg}=59$  GHz for a device with  $\Lambda=500$   $\mu$ m and  $\eta=0.4$ . This value fits well to the measured S-parameters (cf. Fig. 4.23). It suggests that a period length of  $500$   $\mu$ m is an upper acceptable limit for  $40$  GHz modulation bandwidth.

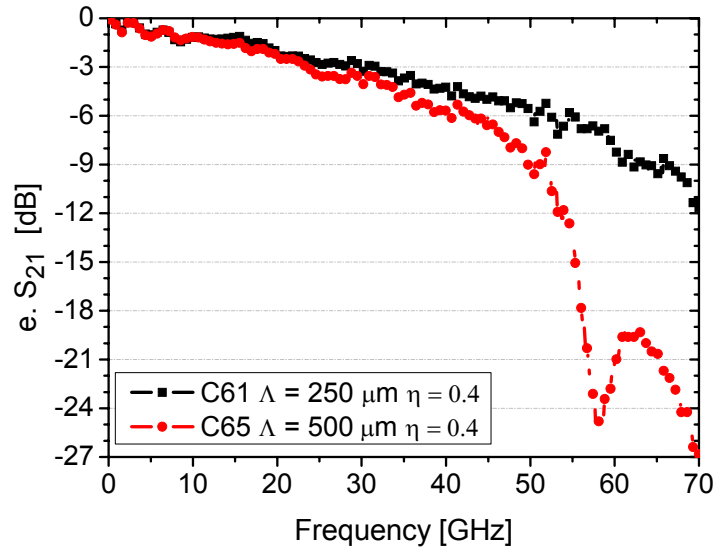


Fig. 4.23 Measured  $S_{21}$  parameters of two modulators ( $l=3$  mm,  $\eta=0.4$ ) with  $250$   $\mu$ m and  $500$   $\mu$ m period length, respectively

Taking (3.3.4) into (4.5.1), we get

$$f_{Bragg} = \frac{c}{\pi \cdot \Lambda \cdot n_{\mu}}, \quad (4.5.3)$$

This means the Bragg frequency can be calculated with the following parameters: the period length and the microwave index of the modulator. As the design target, the microwave index should equal the optical index in a modulator. So, we can calculate the maximum period length using (4.5.4) under the condition that the Bragg frequency should be kept far away from the modulation frequency range, or in other words, the operation speed of the modulator should not be limited by the Bragg frequency in the frequency range of interest.

$$\Lambda \leq \frac{c}{\pi \cdot f \cdot n_{opt}} \quad (4.5.4)$$

Taking  $n_{opt} = 3.7$ , we get  $\Lambda \leq 323 \mu\text{m}$  and  $\Lambda \leq 252 \mu\text{m}$  for  $f = 80 \text{ GHz}$  and  $f = 100 \text{ GHz}$ , respectively. Hence, we choose  $250 \mu\text{m}$  as well as  $125 \mu\text{m}$  as period length for the modulators which are designed to work up to  $80 \text{ Gbit/s}$  or a higher speed.

#### 4.6 TOWARDS VELOCITY MATCH

As discussed in Chapter 3, the aim in traveling-wave design is to achieve a modulating voltage wave which propagates at exclusively the same speed as the the optical wave, permitting the phase modulation to accumulate monotonically irrespective of frequency. Velocity mismatch (cf. Fig. 4.24) causes phase walkoff between the two waves resulting, with increasing frequency and distance, in the cancellation of initial modulation by subsequent antiphase modulation [13].

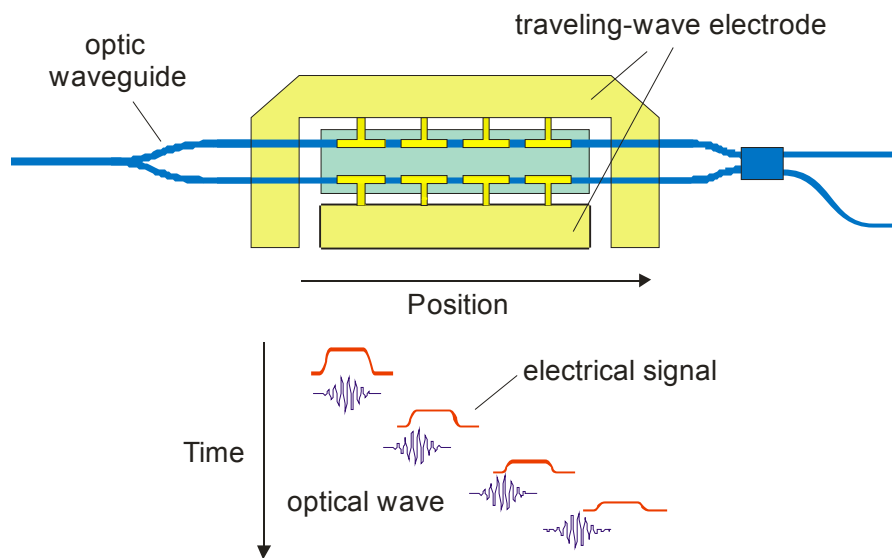


Fig. 4.24 The propagation of optical and electrical signals in the modulator [14]

The relationship between the bandwidth and the velocity match of an idealized traveling-wave modulator (without microwave loss) which is already illustrated in equation (3.4.9) can be rewritten as

$$f_0 = \frac{1.39}{\pi \cdot \left| \frac{1}{v_{opt}} - \frac{1}{v_{\mu}} \right| \cdot l} \quad (4.6.1)$$

where  $v_{opt}$  and  $v_{\mu}$  are the optical and microwave velocity respectively,  $l$  is the electrode length. To increase the 3 dB optical bandwidth  $f_{3dB_{eo}}$ , the microwave velocity  $v_{\mu}$  and the optical velocity  $v_{opt}$  should be as close as possible.

To achieve velocity match, one should know the values of the two velocities. However, the velocity that needs to be matched presents a choice. It can be either the phase velocity or the group velocity.

The phase velocity is defined as the rate at which the crests of the waveform propagate; that is, the rate at which the phase of the waveform is moving. The group velocity is the rate that the envelope of the waveform is propagating; that is, the rate of variation of the amplitude of the waveform. It is the group velocity that (almost always) represents the rate that information (and energy) may be transmitted by the wave, for example the velocity at which a pulse of light travels down an optical fiber.

For a single frequency waveform, the phase velocity is the same as the group velocity. But it reveals that once the optical signal starts to interact with the electrical signal it is no longer a single frequency waveform. It is clearly phase modulated and the center of gravity of this phase modulated waveform travels with the group velocity. This velocity should be the same as the group velocity of the electrical waveform so that they keep interacting and the phase modulation accumulates. Therefore group velocities should match [15].

#### 4.6.1 Optical Group Index ( $n_{opt}$ )

The optical group index is defined here as

$$n_{opt} = \frac{c}{v_{gr-o}} \quad (4.6.2)$$

where  $v_{gr-o}$  is the group velocity of the optical signal. It depends on light wavelength, crystal composition, lattice mismatch, doping level and carrier density.

The optical group index  $n_{opt}$  is primarily determined by fundamental material parameters and can consequently hardly be changed. Its value can be derived experimentally using the Fabry-Perot method.

$$n_{opt} = \frac{\lambda^2}{2 \cdot l \cdot \Delta\lambda} \quad (4.6.3)$$

where  $\lambda$  is the wavelength of the optical signal,  $l$  is the length of waveguide, and  $\Delta\lambda$  is the wavelength difference between two adjacent maximum points.

To determine the group velocity in optical waveguides, a few separate optical waveguides are fabricated on the same wafer as the modulator. Fig. 4.25 shows a curve measured by using the Fabry-Perot method. The test-structure has an optical waveguide with length of 12.2 mm. The wavelength of optical signal,  $\lambda$ , is 1550 nm. The calculated optical effective refractive index  $n_{opt}$  is 3.7.

The simulation in FIMMWAVE with the same structure provided the same value of the optical group index of 3.73 by the first mode of optical signal in the waveguide.

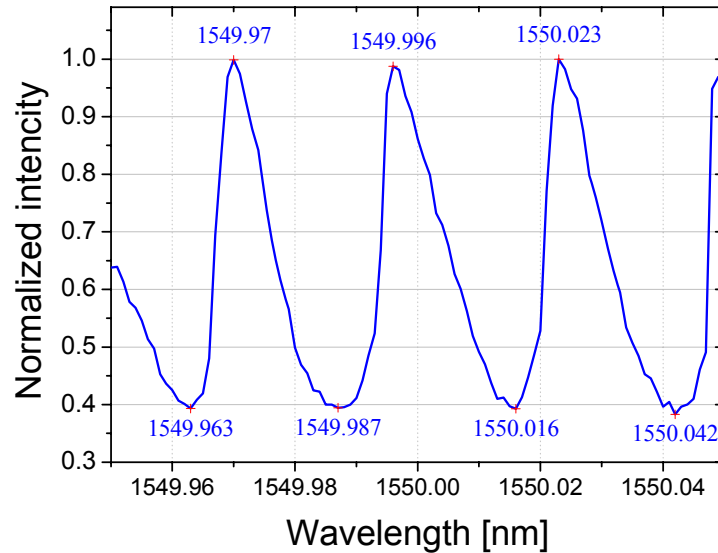


Fig. 4.25 Measured data of a 12.2 mm long waveguide by the Fabry-Perot method

#### 4.6.2 Microwave Effective Refractive Index ( $n_\mu$ )

In TWE MZMs, CPS is used for transmitting the microwave signal into the inner active electrode to execute the push-pull operation. As a normal CPS structure, which is placed on the InP substrate, the value of  $n_\mu$  is close to  $\sqrt{\frac{\epsilon_r + 1}{2}}$ , where  $\epsilon_r$  is the dielectric constant of the substrate, here it has a value of 12.56 for semi-isolating InP,

so  $n_\mu$  is close to 2.6, compared to an optical index of 3.7. But actually the electrodes studied here consist of CPS periodically loaded with capacitive elements. The loading results in a higher effective index for the microwave, and a lower characteristic impedance for the transmission line.

The amount of slowing depends on numerous parameters; nonetheless, it is possible to achieve an  $n_\mu$  nearly equal to  $n_{opt}$ .

To optimize the electrode design, it is important to calculate and compare  $n_\mu$  both in simulation and in the measurement. To calculate  $n_\mu$  of the device, there are two methods, both using measured or calculated S-parameters.

$n_\mu$  can simply be calculated using the resonance peaks by measuring the frequency separation between them. The microwave index is given by

$$n_\mu = \frac{c}{2 \cdot l} \cdot \frac{1}{\Delta f} \quad (4.6.4)$$

where  $\Delta f$  is the frequency spacing between two adjacent minima of  $S_{11}$ , and  $l$  is the length of the electrode. This corresponds to a ‘‘Fabry-Perot method’’ in the electrical domain. Fig. 4.26 shows the calculated microwave index and the measured  $S_{11}$  curve of the modulator with  $l = 3$  mm.

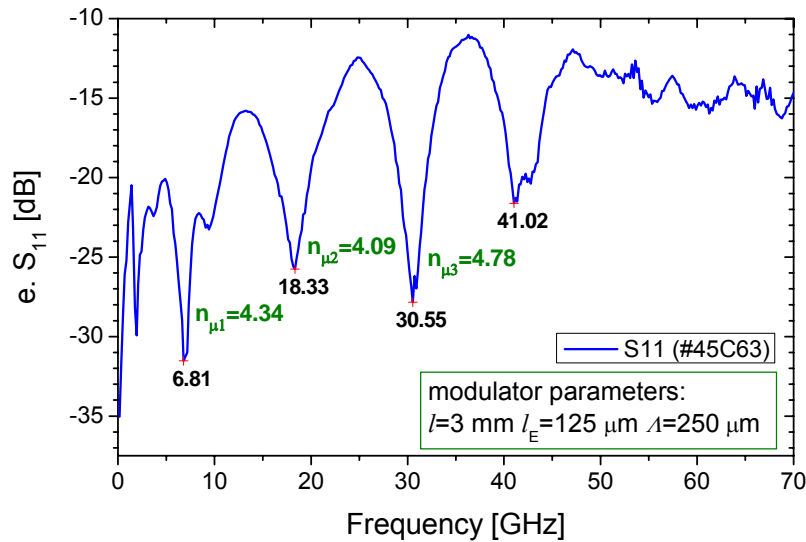


Fig. 4.26 Measured  $S_{11}$  and converted corresponding  $n_\mu$  of a modulator (#45C63)

However,  $n_\mu$  is not a constant for the whole frequency range (cf. Fig. 4.27b). The method introduced above cannot express the difference of  $n_\mu$  in different frequency areas and the calculated  $n_\mu$  is also influenced strongly by  $\Delta f$ , which is limited by the inaccuracy of measurement (cf. Fig. 4.26). It can be seen that the calculated  $n_\mu$  in Fig. 4.26 changes between 4.09 and 4.78.

The microwave effective refractive index  $n_\mu$  can also be derived using the phase part of  $S_{21}$  parameters according to

$$n_\mu(f) = \frac{\phi(f) \cdot c}{2 \cdot \pi \cdot f \cdot l} \quad (4.6.5)$$

where  $\phi(f)$  is converted accumulated phase delay of  $S_{21}$  in rad. Using this method one can get a precise curve describing  $n_\mu$  as a function of frequency.

To compare the difference of the two methods, the same modulator's measured data are used for the calculation again. Fig. 4.27(a) shows the phase part of the measured  $S_{21}$  of the modulator. These phases are converted into accumulated phase delay as its zero point is set by frequency of 0. In Fig. 4.27(b) the blue curve represents the phase delay in unit of radian, the black one is the corresponding curve of the calculated microwave index using (4.6.5). The calculated microwave index is ascending as the frequency increases, because the parasitic capacitance in the active area of a modulator is increasing as the working frequency ascends.

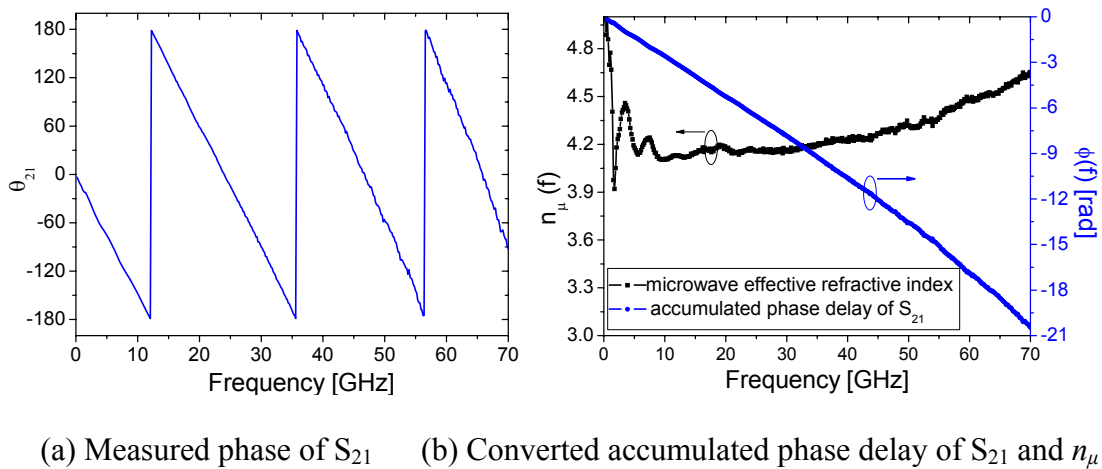


Fig. 4.27 Measured phase and converted corresponding  $n_\mu$  of a modulator (#45C63)

### 4.6.3 The Strategy Towards Velocity Match

Since the experimentally determined optical group index  $n_{opt} \approx 3.7$  can hardly be changed, the microwave refractive index  $n_\mu$  has to be adjusted to this value.

Fig. 4.28 shows  $n_\mu$  and  $n_{opt}$  of two devices which are acceptable for 40 Gbit/s operation.  $n_\mu$  is calculated according to the measured S-parameters of the modulator. Obviously,  $n_\mu$  is larger than  $n_{opt}$ . The figure suggests that a good velocity match is expected for  $\eta \approx 0.2 \sim 0.3$ . However, the driving voltage would increase above 6 V. Therefore, an approach other than reducing  $\eta$  is required.

An alternative way to speed up the electric signal is to reduce the relevant dielectric constant ( $\epsilon_r$ ) of the structure by inserting a low- $\epsilon_r$  material between the InP substrate and the electrodes. In this way, the fill factor and the electro-optic efficiency can be kept. Benzocyclobuten (BCB) is such a low- $\epsilon_r$  material and has the required material property:  $\epsilon_r = 2.6$ .

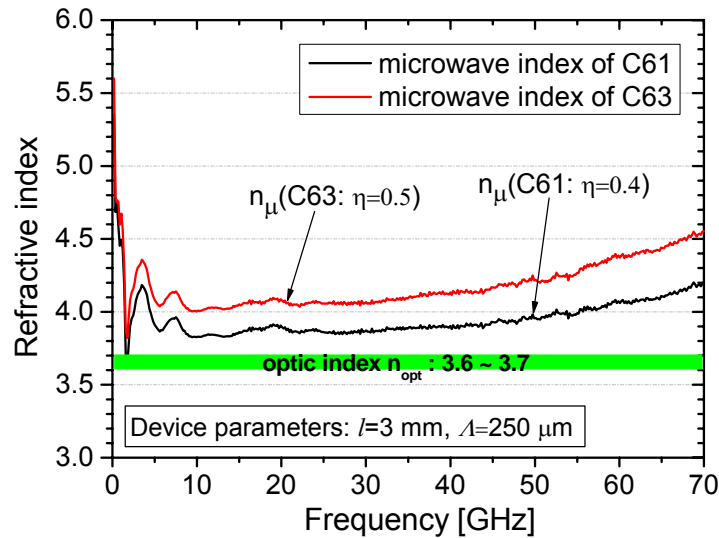
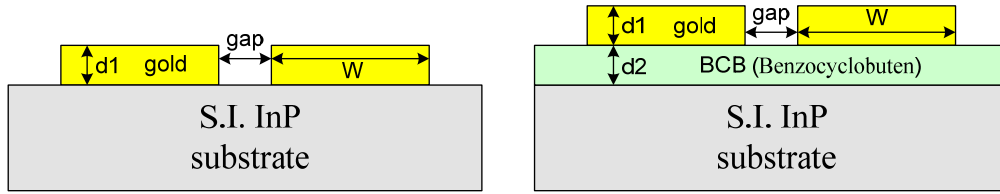


Fig. 4.28 Microwave index and the optic index of two modulators

To determine the BCB's influence to the microwave index of the device two types of test coplanar strips have been fabricated, as shown in Fig. 4.29; one directly on the InP substrate (cf. Fig. 4.29(a)) and one with a 3.5  $\mu\text{m}$  thick BCB layer inserted between the electrodes and the InP substrate (cf. Fig. 4.29(b)). The experimental

results (cf. Fig. 4.30) show that the integrated BCB layer reduces  $n_{\mu}$  of the unloaded TWE structure by about 0.3.



(a) Electrodes deposited on substrate (b) Sandwich BCB between the electrodes and the substrate

Fig. 4.29 Cross-sectional view of CPS test structures

Fig. 4.31 shows the experimental electro-optical responses of two modulators selected from the same wafer, which have the same parameters except that one using the BCB as buffer layer between electrodes and the substrate. After using BCB, the electrical velocity matches better than before, and the 3 dB bandwidth of the modulator increases correspondingly from 33 GHz to 43 GHz.

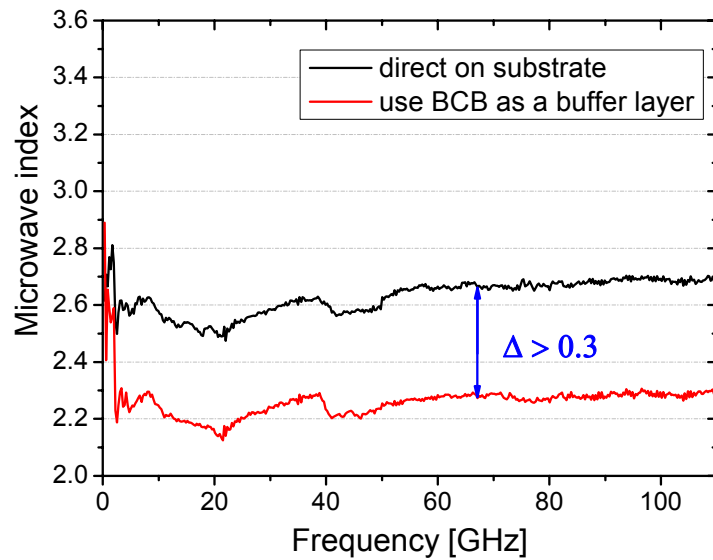


Fig. 4.30 Microwave indices of unloaded TWE test structures

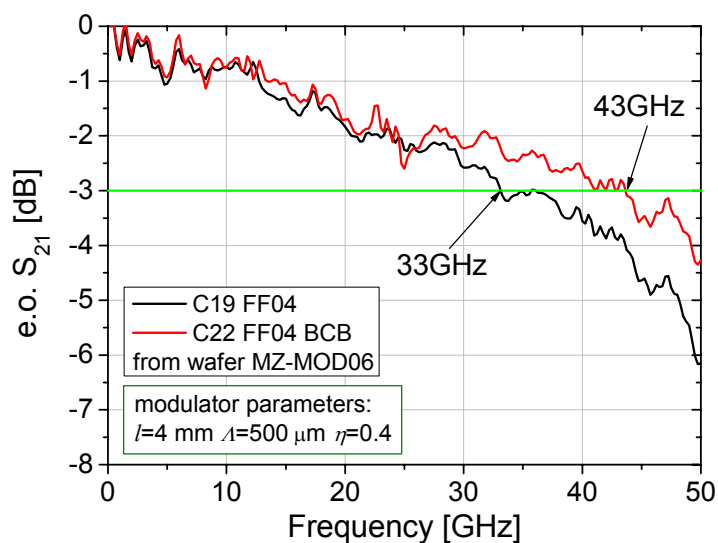


Fig. 4.31 Electro-optical response of the modulators with and without BCB layer

#### 4.6.4 Co- and Counter-propagation

In the preceding section, the optical and electrical waves are propagating in the same direction. This is known as co-propagation. As discussed above, co-propagation and velocity match ensure the maximum modulation efficiency and bandwidth. However, it is instructive to consider what happens when electrical and optical waves propagate in opposite directions, a condition known as counter-propagation.

Fig. 4.32 shows the experimental electro-optical responses of the same modulator under co-propagation and counter-propagation conditions, respectively. The modulator achieves 3-dB bandwidth of 45 GHz when the electrical signal co-propagates with the optical wave. Under counter-propagation condition, the bandwidth is only 3.5 GHz. This indicates that the reflected HF signal can cause an unwanted destructive effect if the modulator is not terminated with proper impedance.

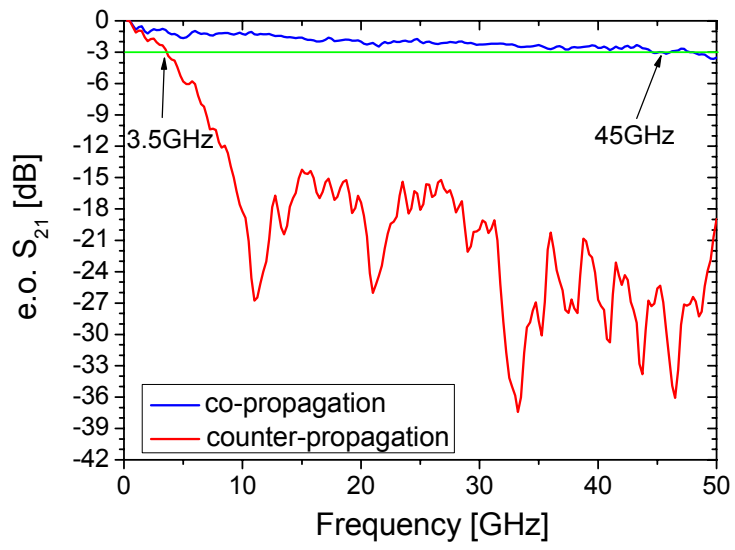


Fig. 4.32 The electro-optical responses of a modulation under co- and counter-propagation conditions, respectively

## 4.7 MINIMIZATION THE MICROWAVE LOSS IN THE MODULATOR

Although during modeling and the simulation the microwave loss in a modulator can be expressed as a parameter  $\alpha$ , actually it is a combination of many different factors. The microwave loss in a TWE MZM exists not only in coplanar strips but also in the active area. They will be deeply discussed in this section.

### 4.7.1 The Microwave Loss in the Traveling-Wave Electrode

As introduced before, CPS is chosen as traveling-wave electrodes for a modulator in this work. Compared with the normal CPS, the CPS in the modulator has an extra strip between two metal strips. The microwave loss in the normal CPS and its variant will be discussed separately in this section.

#### 4.7.1.1 *The Microwave Loss in the Normal CPS*

In order to study their microwave loss, three different straight CPS (without the loaded modulation elements) are simulated up to 100 GHz in HFSS. As shown in Fig. 4.33, these three CPS have the same geometry parameters ( $l=1$  mm,  $w=120$   $\mu\text{m}$ ,  $s=60$   $\mu\text{m}$ ), but are deposited on different materials. One is deposited on the intrinsic layer (i-layer), under which is the n-doped layer (cf. Fig. 4.33(b)), one is deposited directly on the substrate (cf. Fig. 4.33(c)), and one is deposited on the BCB (benzocyclobuten) layer (cf. Fig. 4.33(d)).

The simulation results as shown in Fig. 4.34 are as follows: the microwave loss of CPS which is located directly on the substrate, is low enough even up to 100 GHz ( $<0.11$  dB/mm@100 GHz). However, the loss (0.19 dB/mm@100 GHz) nearly doubles if CPS is deposited on the i-layer, under which is the n-doped layer. Because the i-layer has been defined as the same as the substrate in HFSS, it can be concluded that the extra microwave loss is caused by the n-doped layer. Thus, in order to decrease the microwave loss in CPS, the n-doped semiconductor layers under the coplanar-line should be removed.

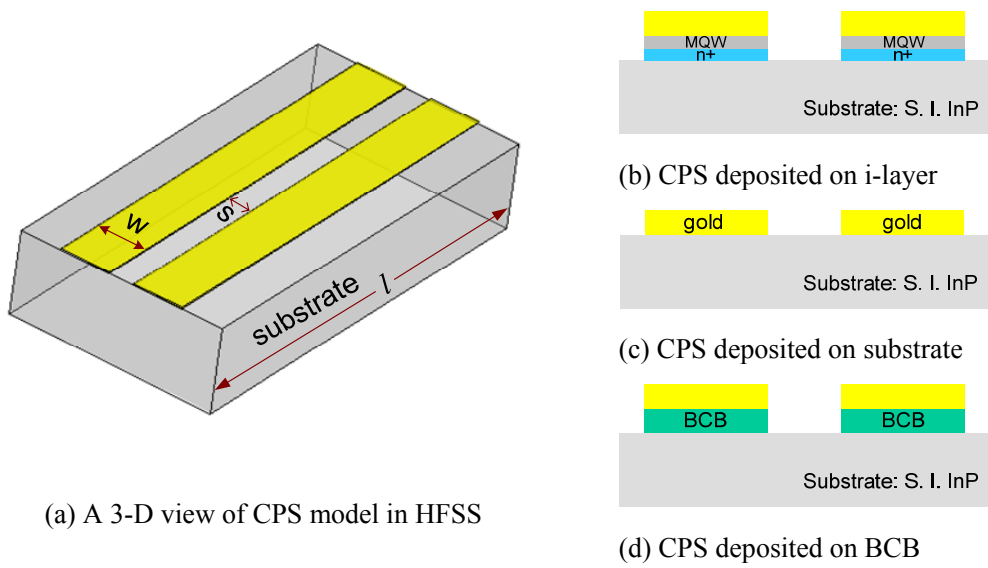


Fig. 4.33 The CPS structures simulated in HFSS

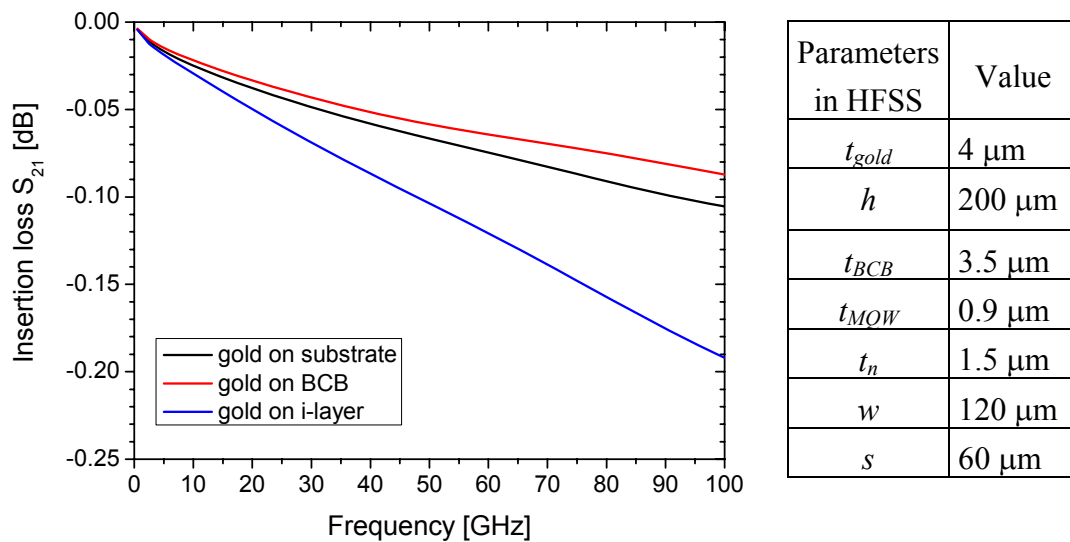


Fig. 4.34 Simulated insertion loss of 1 mm CPS

However, there is a technological problem, since the TWE connect the inner electrodes through air-bridges, and between the inner electrodes and substrate there are p-i-n structures whose height is about 3.5  $\mu\text{m}$ . This means, if the CPS is deposited directly on the substrate, the air-bridges should cover the drop height of 3.5  $\mu\text{m}$ , which is technologically difficult. One solution is to use a dielectric material to block up the CPS. Benzocyclobuten (BCB) is such a dielectric material, which is often used in

optoelectronic devices. In Fig. 4.34, the red curve shows the microwave loss of the CPS, which uses 3.5  $\mu\text{m}$  thick BCB as a buffer layer between the electrodes and the substrate. The loss is only about 0.09 dB/mm@100 GHz, even less than the loss of the CPS whose electrodes are deposited directly on the substrate. Since the position of the electric field between the two electrodes after using 3.5  $\mu\text{m}$  thick BCB is higher, the field which is buried in the substrate is correspondingly smaller, so the dielectric loss of the CPS is less than in the case without BCB layer.

#### 4.7.1.2 The Microwave Loss in the CPS with Mesa

Unlike the CPS which is shown in Fig. 4.34, there is a layer stack between two metal strips of the CPS in the modulator (cf. Fig. 4.35). This layer stack is called mesa and consists of a MQW structure and an n-doped layer. As discussed in section 4.7.1.1, the n-doped layer can induce extra microwave loss. Because of the background doping, the MQW layers are also lossy. But this time, those lossy layers cannot easily be removed as before, because they are essential for the EO effect.

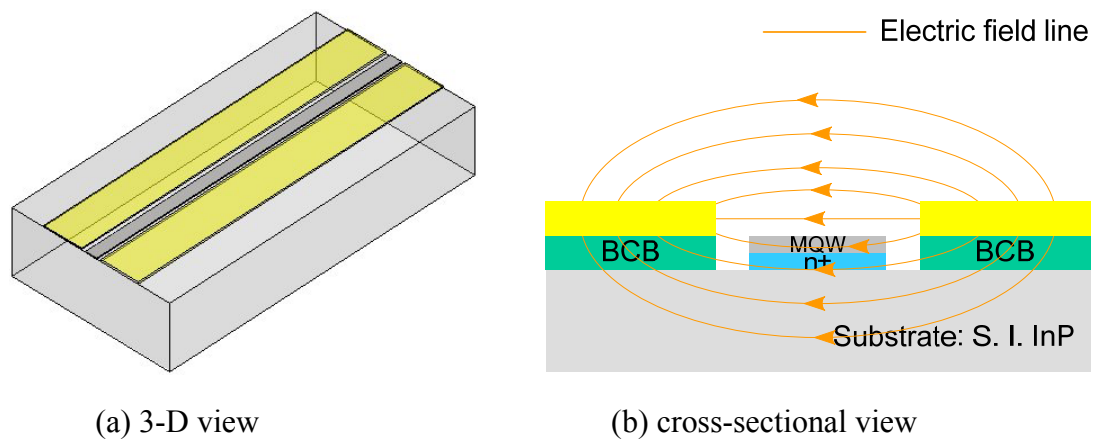


Fig. 4.35 CPS with mesa

To study the impact of the mesa on the microwave loss, three CPS with mesa, whose structures are shown in Fig. 4.35, are simulated in HFSS. The CPS is deposited on the BCB layer to achieve a minimum loss and has the same geometry parameters as the CPS simulated in section 4.7.1 ( $l=1$  mm,  $w=120$   $\mu\text{m}$ ,  $s=60$   $\mu\text{m}$ ). To ensure the EO

effect in the optical waveguide, the width of the mesa is set to 16  $\mu\text{m}$ , 26  $\mu\text{m}$  and 36  $\mu\text{m}$ , respectively. The simulations run also up to 100 GHz and the results are shown in Fig. 4.36. The insertion loss of the CPS without mesa is also shown in the figure. Comparing the four curves in the figure, one can conclude that the wider the mesa is, the more microwave loss will be induced. This can be explained by the Fig. 4.35(b), the lower part of the electric field between the two electrodes of the CPS passes through the lossy mesa and the substrate. The part of the electric field that passes through the mesa decreases if the mesa's width gets smaller. Consequently, the microwave loss induced by the lossy mesa will also decrease. The curves in the figure illustrate that the insertion loss of the CPS with the mesa whose width is 16  $\mu\text{m}$  is almost the same as that of the CPS without mesa up to 50 GHz. At the same time 16  $\mu\text{m}$  is also technologically the minimum width to guarantee the EO effect.

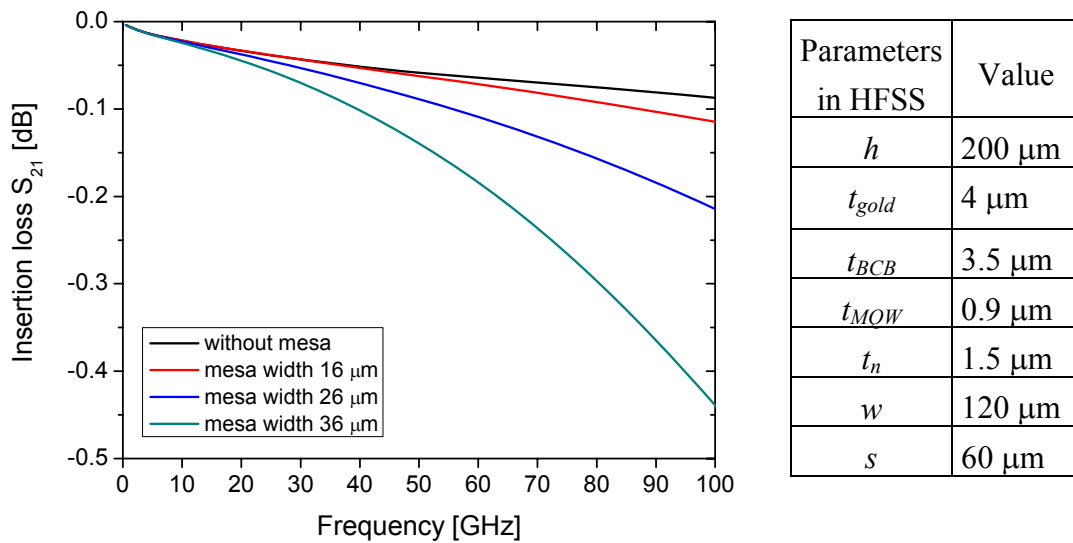


Fig. 4.36 The impact of mesa width on the insertion loss of the CPS

#### 4.7.2 The Microwave Loss in the Active Area

The analysis in the preceding section suggests that the microwave loss in the CPS with mesa is possible to be controlled within 0.1 dB/mm@50 GHz. However,

according to the experimental results (cf. Fig. 4.10), the microwave loss in the modulator is higher than 2 dB/mm@50 GHz, i.e., it is significantly higher. As will be shown in this section, the major part of the actually observed microwave loss of a modulator exists in the active modulation area, where the EO effect takes places.

#### 4.7.2.1 Series Resistance Analysis

The microwave loss in the active area of a modulator is mainly due to the series resistances of two p-type ridges and the underlying n-layer of the mesa, and as described in Fig. 4.18 and Fig. 4.20(b), these resistances consist of the bulk resistance of p-doped layers ( $R_p$ ), p-contact resistances ( $R_c$ ) and the bulk resistance of the n-doped layer ( $R_n$ ). The latter two appear even twice in the active area because of the push-pull structure. Table 4.4 in section 4.3.5 illustrates the value of those impedances in a modulator. It is obvious that the p-contact resistance and the bulk resistance of the n-doped layer are much more than the bulk resistances of p-doped layers.

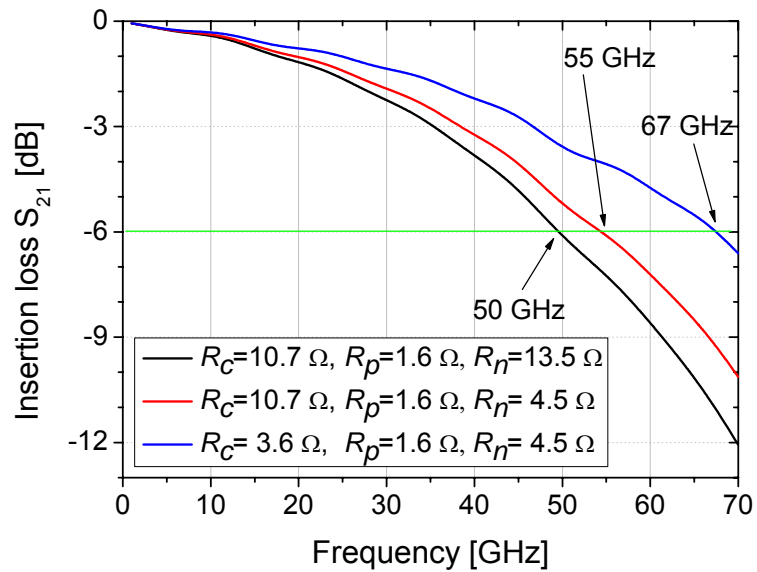


Fig. 4.37 The impact of the series resistance in the active area on the insertion loss of the modulator ( for  $R_c=10.7 \Omega$ , the corresponding  $\rho_c$  is  $3 \times 10^{-5} \text{ cm}^2 \cdot \Omega$  )

The electrical insertion loss is simulated with different values of the series resistance using the detailed circuit model introduced in section 4.4. The other device

parameters are the same as the modulator simulated in Fig. 4.22(a), i.e.  $l=3$  mm,  $\Lambda=250$   $\mu\text{m}$ ,  $\eta=0.4$ . The simulation results are shown in Fig. 4.37. The figure shows: when  $R_n$  decreases to one third of its initial value, the electrical bandwidth expands from 50 GHz to 55 GHz; on this condition, if  $R_c$  decreases also to one third of its initial value, the bandwidth will expand further to 67 GHz. Therefore, it can be concluded these series resistances are the dominant factor of the microwave loss in a modulator. On the premise that the EO effect in the modulator is guaranteed, minimizing these impedance is the most efficient way to expand the working bandwidth of the modulator.

After analyzing each parameter in the expression (4.3.7), we find it is possible to decrease  $R_n$  to one third. Mathematically, to decrease  $R_n$ , one can either decrease  $d$  or increase  $\sigma_n$ ,  $\eta$ ,  $\Lambda$  or  $d_n$ . However, changing one or some of these parameters can cause other problems. The center to center distance between the two inner electrodes,  $d$ , is also the distance between two optical waveguides, which is an important parameter for the Y-branch and MMI design. The Y-branch and MMI need redesign if  $d$  changes. The value of the conductivity of the n-layer,  $\sigma_p$ , is proportional to the doping density of the n-layer which involves the EO effect. Bigger  $\sigma_n$  means higher doping density, which is technologically difficult to achieve. The fill factor  $\eta$  involves the driving voltage and velocity match and is consequently fixed for the best velocity match. The period length  $\Lambda$  is tunable, but its maximum is limited by the Bragg frequency. However it indicates the period length should be designed as long as possible to achieve a possible small  $R_n$ . The thickness of the n-layer  $d_n$ , is also a tunable parameter. There is no foreseeable destructive effect after increasing its value if BCB layer is used as buffer layer instead of n-layer and i-layer for the CPS. Therefore we increase  $d_n$  from 0.5  $\mu\text{m}$  to 1.5  $\mu\text{m}$  to decrease  $R_n$  to one third.

The p-contact resistance,  $R_c$ , can also be reduced and will be discussed separately in the next section.

#### 4.7.2.2 Optimizing the p-Contact Resistivity

The former analysis shows that the p-contact resistance,  $R_c$ , is one of those elements which determine the high frequency electric loss of the modulator.  $R_c$  can be calculated by

$$R_c = \frac{\rho_c}{w_c \cdot \Lambda \cdot \eta} \quad (4.7.1)$$

As discussed before,  $\eta$  is almost fixed for perfectly velocity match and  $\Lambda$  should be set to its upper limit to decrease  $R_c$ .  $w_c$  is the width of the contact area and is normally dependent on the width of the optical waveguide. The p-contact resistivity,  $\rho_c$ , is an important parameter for  $R_c$ . To determine the impact of  $\rho_c$  on the electrical insertion loss of modulator, modulators with different value of  $\rho_c$  are simulated in HFSS. The modulator is 3 mm long and has a period length of 250  $\mu\text{m}$  and a fill factor of 0.4. The corresponding material property of the p-layer has been calculated and is listed in table 4.3. The simulation results are shown in Fig. 4.38 which indicates that the electrical bandwidth,  $f_{6dB_e}$ , can be extended to 80 GHz if  $\rho_c$  can be reduced to  $1 \times 10^{-6} \text{ cm}^2 \cdot \Omega$ .

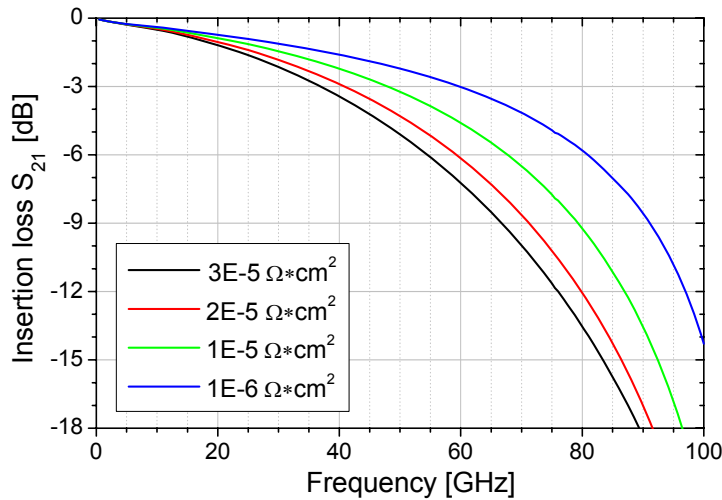


Fig. 4.38 Simulated insertion loss of modulators with different  $\rho_c$  using HFSS

Since  $\rho_c$  cannot be measured directly using a complete modulator structure, test structures for the p-contact resistance are designed as described in Fig. 2.16 in

section 2.5 and fabricated on the same wafer with modulators to monitor the p-contact resistivity in the device.

To achieve a small  $\rho_c$ , the top p-layer in the modulator has been heavily doped, the doping density is  $1 \times 10^{19} \text{ cm}^{-3}$ . The Ti-Pt-Au alloy has also been used to decrease  $\rho_c$ . Nevertheless, the measurement shows the p-contact resistivity is around  $3 \times 10^{-5} \Omega \cdot \text{cm}^2$  in the modulator.

The study indicates one can improve  $\rho_c$  by using the post-doping process, by which the doping density of the top p-layer can be further increased. Our measured data show that  $\rho_c$  can be improved to  $5 \times 10^{-6} \text{ cm}^2 \cdot \Omega$  in the test structure.

#### 4.7.3 Simulation Results of Optimized Modulator

As discussed above, to minimize the microwave loss in the modulator, the CPS electrodes should be deposited on the BCB layer, the width of the mesa should shrink, post Zn-doping process should be used for achieving a smaller p-contact resistivity, the n-doped layer should be designed thicker and the center-to-center distance between two ridges should be as short as possible.

To study the effect of those parameters on the electro-optical response, three groups of modulators are simulated in HFSS. All of those modulators use the BCB layer as a buffer layer between the CPS electrodes and the substrate. The TWE length of all modulators is 3 mm. For each group of modulator, the fill factor increases from 0.2 to 0.7 linearly. All of the simulated electrical insertion loss are further converted into electro-optical response using (3.4.16). The  $n_{opt}$  used in the calculation is set as 3.7. The modulators of group one have the p-contact resistivity ( $\rho_c$ ) of  $2 \times 10^{-5} \Omega \cdot \text{cm}^2$ , the mesa width ( $w_{mesa}$ ) of 26  $\mu\text{m}$ , the center-to-center distance between two ridges ( $d$ ) of 13  $\mu\text{m}$ , the ridge width ( $w_{wg}$ ) of 2.8  $\mu\text{m}$  (These parameters are shown in Fig. 3.13). The modulators of group two have the same parameters as the group one except a better p-contact resistivity ( $\rho_c$ ) of  $5 \times 10^{-6} \Omega \cdot \text{cm}^2$ . The modulators of group three have also a better p-contact resistivity of  $5 \times 10^{-6} \Omega \cdot \text{cm}^2$ , the same as that of type two, but the

mesa width ( $w_{mesa}$ ) of 16  $\mu\text{m}$ , the center-to-center distance ( $d$ ) between two ridges of 10  $\mu\text{m}$  and the ridge width ( $w_{wg}$ ) of 2.2  $\mu\text{m}$ , i.e. the group three has an optimized active area. The calculated results are shown in Fig. 4.39. Table 4.5 gives the comparison of parameters for these three groups. It is clear that after using BCB layer, the velocity match achieves by  $\eta=0.4$  (without the BCB layer, it was expected velocity achieves by  $\eta$  of 0.3 or less). Improving the p-contact resistance extends the  $f_{3dB_{eo}}$  from 61 GHz to 77 GHz. After optimizing the active area, the velocity match is achieved by  $\eta = 0.5$ , and  $f_{3dB_{eo}}$  extends further to 83 GHz.

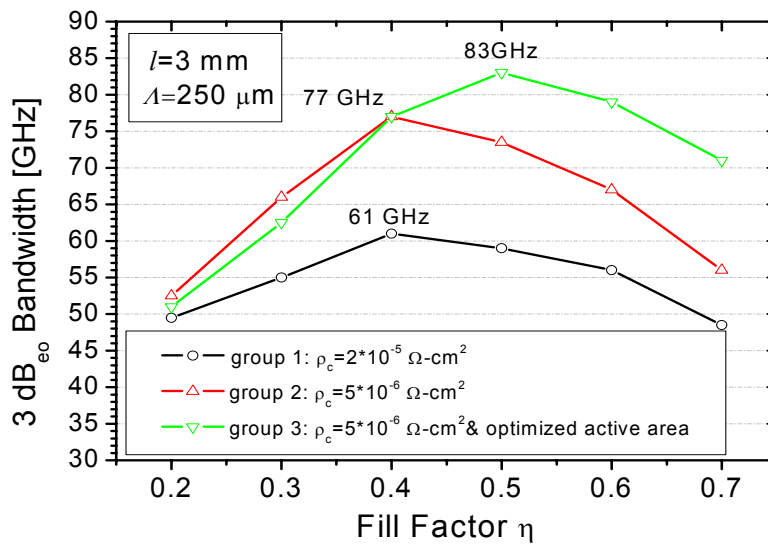


Fig. 4.39 Simulation results of optimized modulator with different fill factors

Table 4.5 Comparison of parameters before and after optimizing

	Group 1	Group 2	Group 3
$\rho_c$	$2 \times 10^{-5} \Omega\text{-cm}^2$	$5 \times 10^{-6} \Omega\text{-cm}^2$	$5 \times 10^{-6} \Omega\text{-cm}^2$
$w_{wg}$	2.8 $\mu\text{m}$	2.8 $\mu\text{m}$	2.2 $\mu\text{m}$
$d$	13 $\mu\text{m}$	13 $\mu\text{m}$	10 $\mu\text{m}$
$w_{mesa}$	26 $\mu\text{m}$	26 $\mu\text{m}$	16 $\mu\text{m}$

#### 4.8 OPTIMIZATION TOWARDS LOWER DRIVING VOLTAGE

In an ETDM transmitter (cf. Fig. 1.1), an electrical amplifier is normally used to amplify the modulating signal before it enters the optical modulator. Hence  $V_\pi$  of the modulator should not be larger than the maximum output voltage of the amplifier, otherwise it is unachievable in the system. In other words, the modulator whose  $V_\pi$  is larger than the maximum output voltage of available amplifiers will be very difficult to be employed in a system. The studies [16,17] show that parameter sets allowing for 80 Gbit/s modulation are only acceptable when  $V_\pi$  is lower than 4 V [16], and for 40 Gbit/s modulation the  $V_\pi$  should be lower than 5.6 V [17]. On these premise, the smaller  $V_\pi$  a modulator has, the easier application could be achieved. Because of their lower costs, the amplifiers with lower gain are more favorable for a transmitter product.

As discussed in section 3.5,  $V_\pi$  is inversely proportional to the effective modulation length,  $l_{eff}$ , so it can be pulled down by extending the effective modulation length of the modulator. In a modulator, to extend the modulation length one can either increase the number of sections or enlarge the fill factor, or use both methods at the same time. However, as discussed before the microwave loss in the modulator is proportional to the modulation length, that is, extending the modulation length can lead to a narrower modulation bandwidth. Moreover, enlarging the fill factor can induce the velocity mismatch, which will also affect the electro-optical response of the modulator. In brief,  $V_\pi$  could be pulled down at the expense of the bandwidth by extending  $l_{eff}$ .

To study the relationship between the 3 dB<sub>eo</sub> modulation bandwidth,  $f_{3dB_{eo}}$ , the effective modulation length,  $l_{eff}$ , and the driving voltage,  $V_\pi$ , a series of modulators are simulated in HFSS and the electro-optical response are calculated using (3.4.16). In order to present the relationship between  $V_\pi$  and  $f_{3dB_{eo}}$ , we assume an electro-optic efficiency of  $V_\pi \cdot l_{eff} = 6$  Vmm (The best value of this product experimentally achieved

is 5.2 Vmm). On that condition, the TWE length  $l$  and the fill factor  $\eta$  as input values for the simulation (due to  $l_{eff} = l \cdot \eta$ ) will be converted into a driving voltage. All the modulators have the same period length of 250  $\mu\text{m}$ . The electrode length differs from 2 mm to 5 mm with a step width of 1 mm. The fill factor for each electrode length differs from 0.2 to 0.8 with step width of 0.1. The simulation results are shown in Fig. 4.40. Modulators with the same length are arranged in groups. Obviously within such groups the modulator with a lower  $\eta$  requires a higher  $V_\pi$ , because its  $l_{eff}$  is shorter. Curves in the figure show that the modulator with shorter electrode length has a wider bandwidth but also a higher  $V_\pi$ . For example, although the bandwidth of the modulator which has the electrode of 2 mm and the fill factor of 0.3 achieves 88 GHz, its  $V_\pi$  is as high as 10 V, which is technologically unpractical. Among those modulators whose  $V_\pi$  is equal to or small than the practical maximum of 4 V, the modulator with 3 mm electrode and the fill factor of 0.5 has the widest bandwidth of 68 GHz.

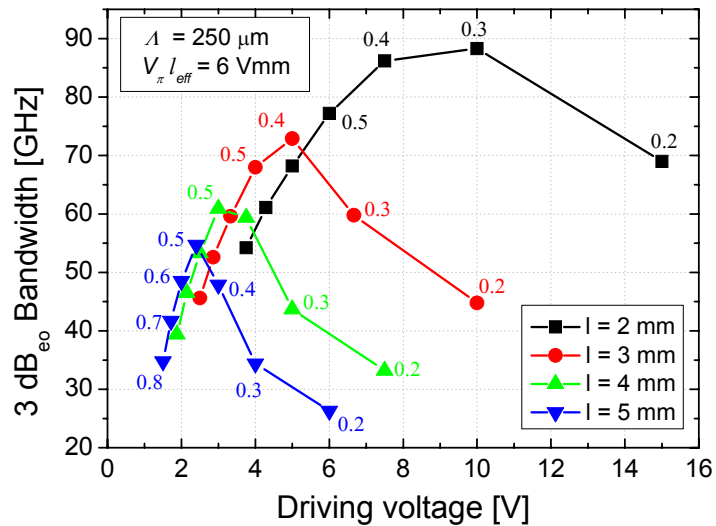


Fig. 4.40 The relationship between the 3 dB<sub>eo</sub> bandwidth, the driving voltage and the fill factor of a modulator

As described in (3.5.6),  $V_\pi$  is proportional to  $d_{pin}$ , the depletion width of the pin diode in a modulator. Therefore, it is possible to reduce  $V_\pi$  through optimizing  $d_{pin}$ .

The analysis in section 2.4.2 shows that  $d_{pin}$  is the sum of the depletion layer width of p-type region,  $x_p$ , the depletion layer width of n-type region,  $x_n$ , and the thickness of the i-region,  $d_i$ . Among them,  $d_i$  gives the major contribution. Therefore, if  $d_i$  can be reduced,  $V_\pi$  will decrease correspondingly. After analyzing the process of epitaxy, we find that the thickness cladding layer could be reduced.

Fig 4.41 shows the measured C-V curves of circular pin diodes (will be discussed in Chapter 6) from wafer MZ-MOD03 and wafer MZ-MOD06. The layer stack of the wafer MZ-MOD06 has been optimized and the thickness of the i-layer is 250 nm less than that of the wafer MZ-MOD03. The experimental results show that  $C_{pin}$  of optimized wafer is 25% more than before and the calculated (using (2.4.13))  $d_{pin}$  is 250 nm less than before. Fig 4.42 shows the measured  $V_\pi$  of the same modulator structure ( $l=3$  mm,  $\Lambda=0.4$ ) from two wafers. The measured  $V_\pi$  decreases from 7 V to 5.6 V.

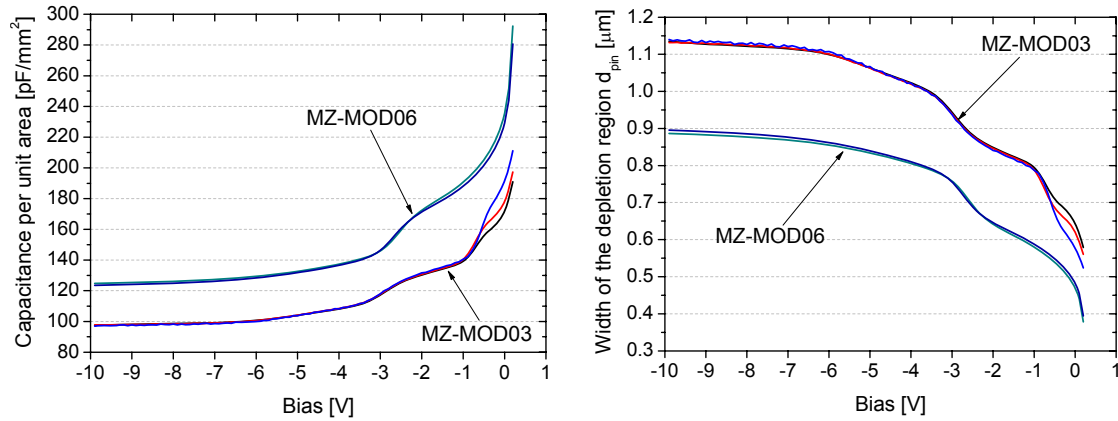


Fig. 4.41 Measured C-V curves with two different i-region thickness

Fig. 4.41 illustrates that  $C_{pin}$  increases 25% after optimization. This will result in a bigger  $C_L$  as described in (4.3.4) and a higher  $n_\mu'$  as described in (3.3.4), which will finally lead to the velocity mismatch. However, the above introduced sandwiched BCB layer can compensate the increased  $n_\mu'$ . As shown in Fig 4.29, the microwave index of the unloaded CPS decreases from 2.6 to 2.3 after using the BCB buffer layer.

The loading capacitance will increase correspondingly from 125pF/m to 151pF/m as shown in Fig. 4.43, which is calculated using (3.3.8) with  $Z_0=50 \Omega$  and  $n_{opt}=3.7$ .

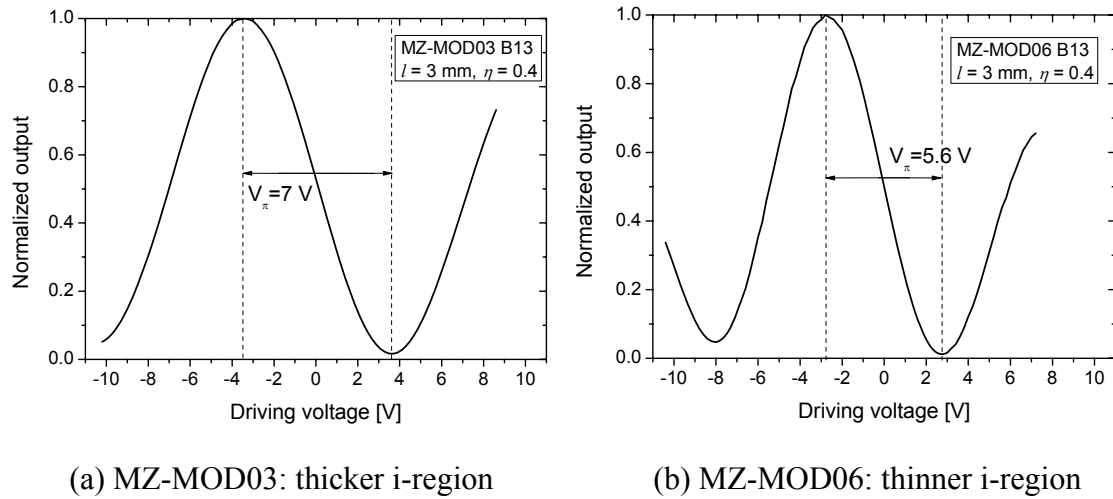


Fig. 4.42 The measured  $V_\pi$  before and after optimizing i-layer's thickness

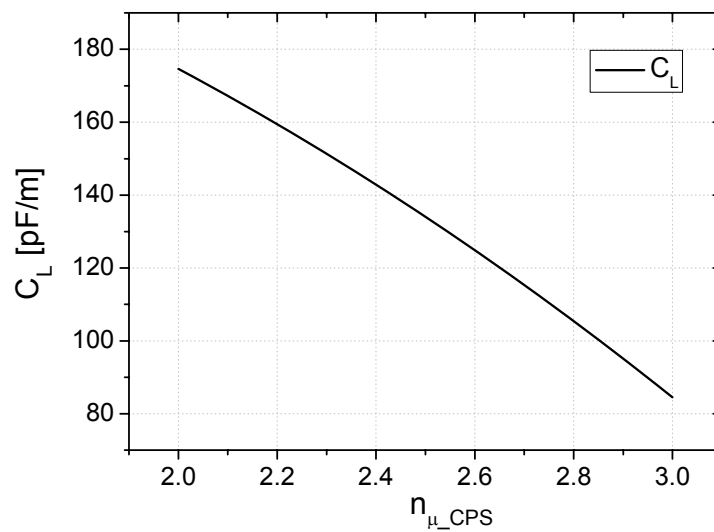


Fig. 4.43 Loading capacitance as function of microwave index of the unloaded CPS

#### 4.9 REDESIGN OF THE ELECTRODE GEOMETRY

Summarizing the strategies mentioned in the preceding sections towards wider bandwidth and lower driving voltage, we get in an optimized modulator:

1. The mesa should be designed as narrow as possible to reduce the microwave loss which exists in the CPS;
2. The n-layer in the mesa should be designed as thick as possible to reduce the series bulk resistance of the n-layer, which improves the microwave loss in the active area;
3. The i-layer should be as thin as possible for a strong electric field across the optic waveguide, which leads to a low driving voltage;
4. A thick BCB layer should be sandwiched between the outer electrode and the substrate to reduce the microwave loss and to achieve a better velocity match.

Fig. 4.44(b) shows the cross section of the optimized modulator, as a reference the cross sectional view of the modulator before optimization is shown in Fig. 4.44(a).

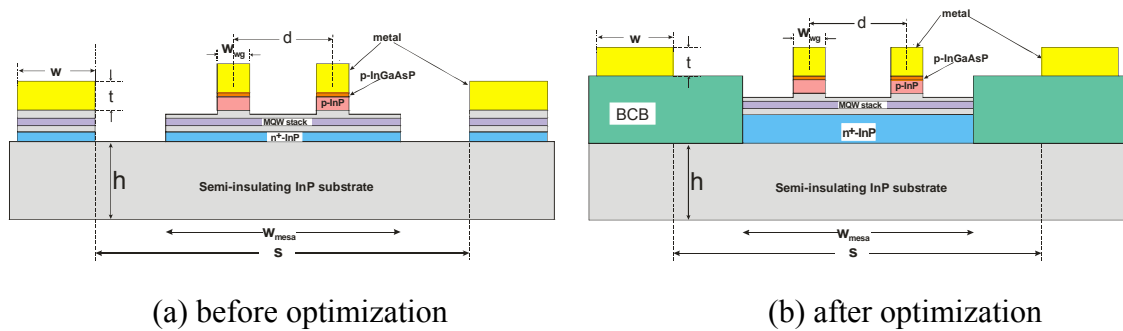


Fig. 4.44 Cross sectional view of the modulator (a) before and (b) after redesign

After optimization, the inserted BCB layer can cause a smaller  $\epsilon_{eff}$  for the device, the characteristic impedance of unloaded CPS will also be larger than before, to keep the device's characteristic impedance of  $50 \Omega$ , the geometry parameter of the unloaded CPS should be redesigned. To study the effect of the BCB layer on the

characteristic impedance of the unloaded CPS, a series of test CPS structures with different  $w$  and  $s$  are fabricated. The cross section of the test CPS structures is the same as shown in Fig. 4.29. The characteristic impedances of the test structures are then calculated from the measured S-parameter using (2.2.15) and (2.2.13). The experimental results are shown in Fig. 4.45. The curves in the figure are calculated using the equations listed in table 2.1. The measured microwave index of 2.3 which is read from Fig. 4.29 is used as  $\sqrt{\epsilon_{eff}}$  for the calculation of the characteristic impedance of the CPS with the buffered BCB layer. Since the experimental points validate the calculated curves, so the equations listed in table 2.1 can be used to design the geometry parameters of the desired CPS.

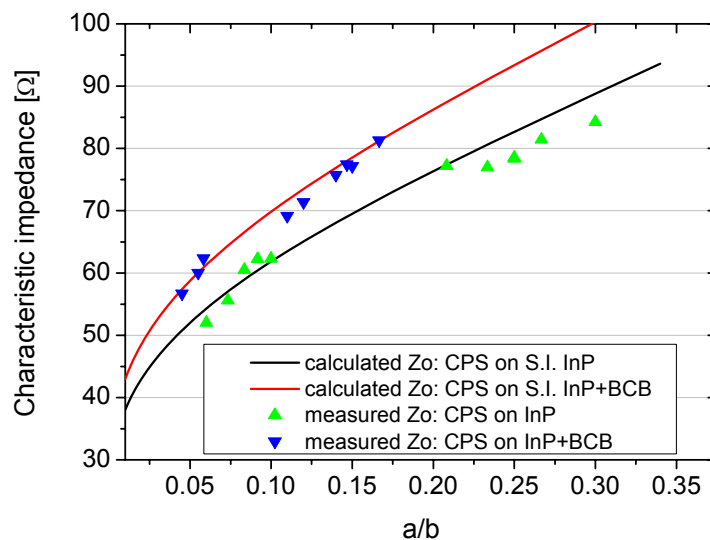


Fig. 4.45 Characteristic impedance for CPS as a function of aspect ratio  $a/b$

The microwave index of the CPS which uses BCB as a buffer layer is 2.3. The optical index of the modulator determined by Fabry-Perot method is 3.7. The characteristic impedance of the modulator is set as 50  $\Omega$ . The modulator fulfilled these three conditions has a traveling-wave structure with the capacitance per unit length of 95 pF/m and the inductance per unit length of 617 nH/m, i.e. the characteristic impedance of 80  $\Omega$ , which can be translated into geometry of the CPS with  $w = 120 \mu\text{m}$

and  $s = 60 \mu\text{m}$  using the curve in Fig. 4.45. The capacitive load of the CPS is  $151 \text{ pF/m}$ . Inserting the experimental data: the reverse biased p-i-n junction's capacitance of  $130 \text{ pF/mm}^2$  and the parasitic capacitance of  $294 \text{ pF/m}$ , one gets the fill factor of  $0.5$ . To ensure the Bragg frequency does not appear in the desired  $3 \text{ dB}_{\text{co}}$  bandwidth, the period length should not exceed  $300 \mu\text{m}$ . This redesign process is illustrated in Fig. 4.46.

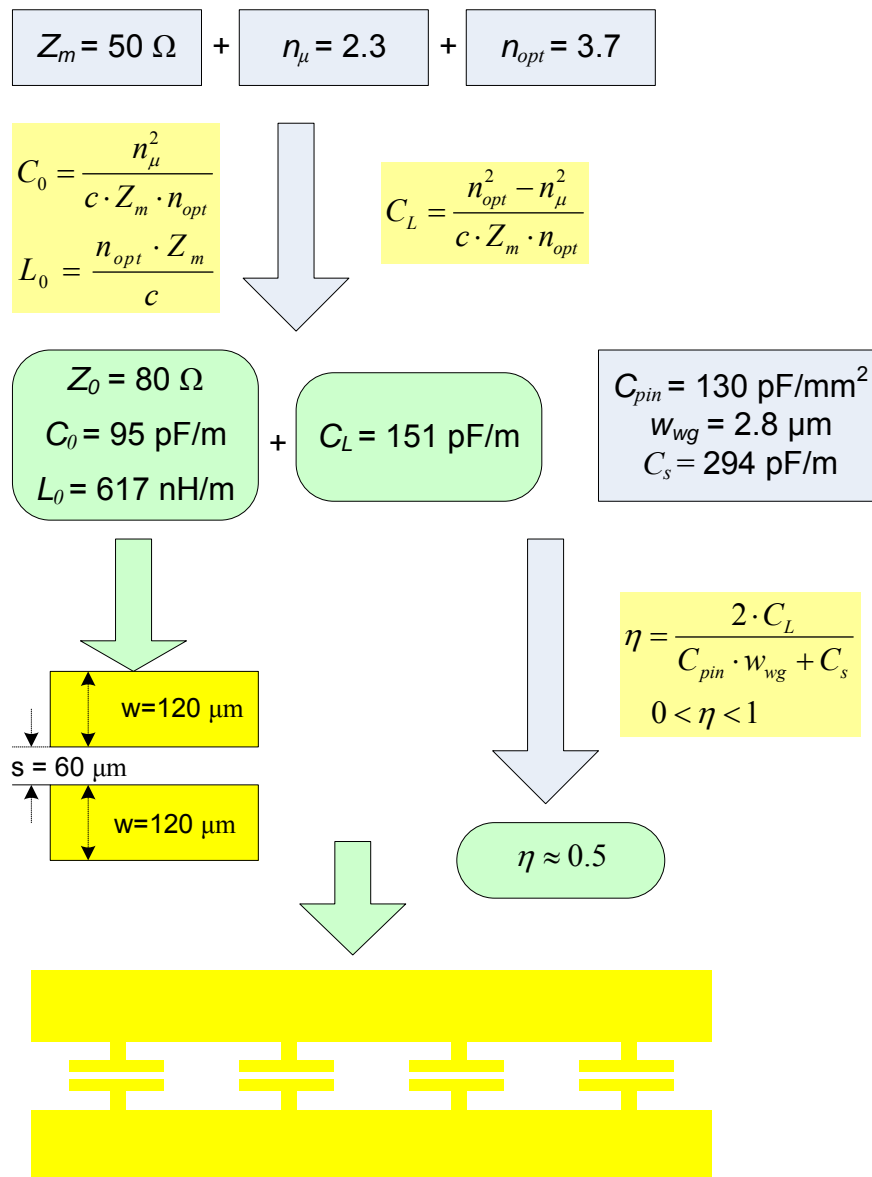


Fig. 4.46 Flow chart of the redesign process

## REFERENCES

- [1] "User's guide of HFSS v9", Ansoft
- [2] S. M. Sze, "Semiconductor devices: physics and technology", Wiley, New York (1985)
- [3] S. L. Chuang, "Physics of optoelectronic devices", Wiley, (1995)
- [4] S. Adachi, "Physical properties of III-V semiconductor compounds: InP, InAs, GaAs, GaP, InGaAs, and InGaAsP", Wiley (1992)
- [5] W. Walukiewicz, "Electron mobility and free-carrier absorption in InP; determination of the compensation ratio", J. Appl. Phys. 51(5), (1980)
- [6] W. Walukiewicz, "Electron mobility and free-carrier absorption in GaAs: determination of the compensation ratio", J. Appl. Phys. 50(2), (1979)
- [7] H. Klein, "Vergleichende Analyse elektrooptischer Effekte in Multi-Quantenfilm- und Bulk-Schichten zur Realisierung von InP-Mach-Zehnder-Modulatoren für 40 Gbit/s", Diplomarbeit, TU-Berlin (2004)
- [8] K. Chang, "Handbook of optical components and engineering", Wiley, Hoboken, NJ (2003)
- [9] S. L. March, "Simple equations characterize bond wires", Microwave & RF, Nov., 105-110 (1991)
- [10] David M. Pozar, "Microwave engineering", 3<sup>rd</sup> Ed., Wiley (2005)
- [11] M. J. W. Rodwell, S. T. Allen, R. Y. Yu, M.G. Case, U. Bhattacharya, M. Reddy, E. Carman, M Kamegawa, Y. Konishi, J. Pusch and R. Pallela: "Active and nonlinear wave propagation devices in ultrafast electronics and optoelectronics," Proc. IEEE **82**, 1037-1059 (1994)
- [12] H. Chen, H. N. Klein, D. Hoffmann, K.-O. Velthaus and H. Venghaus, "Improvement strategy towards 80 Gbit/s low drive voltage InP based Mach-Zehnder modulator", Proceed. 4<sup>th</sup> joint symposium on opto- and microelectronic devices and circuits, SODC2006 85-89 (2006)
- [13] R. G. Walker: "High-Speed III-V Semiconductor Intensity Modulators," IEEE J. Quantum Electron. **27**, 654-667 (1991)
- [14] E. Voges and K. Petermann, "Optische Kommunikationstechnik", Springer, Berlin (2002)
- [15] R. Spickermann, S. R. Sakamoto and N. Dagli, "In traveling wave modulators which velocity to match?", Lasers and Electro-Optics Society Annual Meeting, 1996. LEOS 96., IEEE **2**, 97-98 (1996)

- [16] W. S. Lee: "80+ Gbit/s ETDM system implementation: an overview of current technologies," Opt. Fiber Commun. Conf. OFC2006, paper OTuB3
- [17] Datasheet of SHF product, 803P, Rev. 3.0, (2004)



## Chapter 5

### Fabrication and Packaging

#### 5.1 FABRICATION

The designed modulator test structures were fabricated on a 2 inch wafer by Fraunhofer-Institute for Telecommunications, Heinrich-Hertz-Institut.

The device layouts were transferred by the Mentor Graphics CAD software. The generated mask set comprises 15 individual masks which were fabricated by electron beam lithography.

Standard techniques for processing electro-optic devices based on InP, such as MOVPE, contact lithography, reactive ion etching, wet chemical etching, etc., were used to fabricate the modulator.

The metallization bridges spanning the isolation grooves around the TWE mesas are formed by a galvanic air bridge technique. During this fabrication step, the TWEs are also coated with a 4  $\mu\text{m}$ -thick Au layer. Compared to evaporated metallization layers the lower resistance of electro-plated electrodes considerably improves the RF-performance of the device.

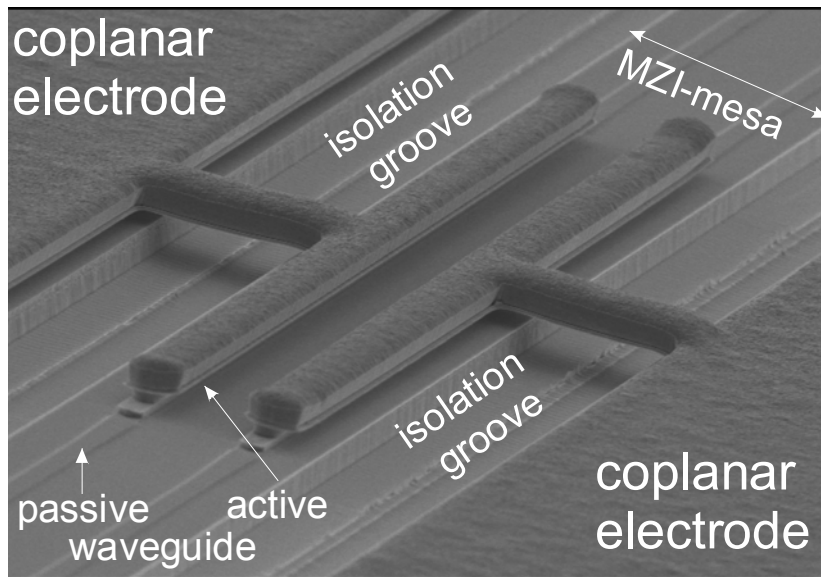


Fig. 5.1 SEM photo of a pair of air bridges between TWE and optical waveguide in a fabricated modulator

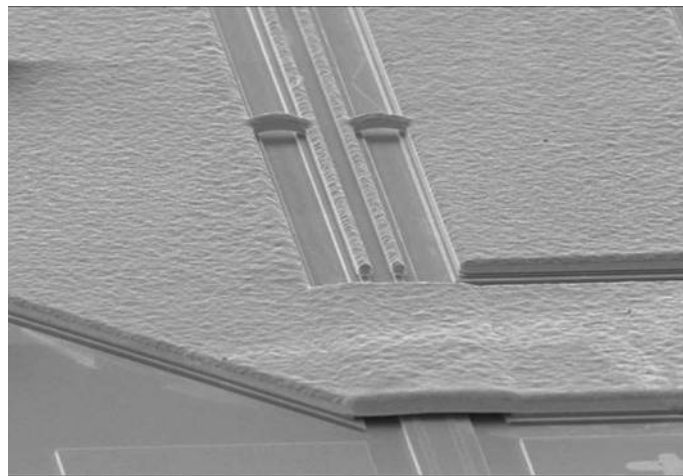


Fig. 5.2 SEM photo of one side of a fabricated modulator

## 5.2 PACKAGING

### 5.2.1 Optical Input and Output

In order to reduce the packaging costs for a commercial product, to enhance the reliability and to decrease optical insertion loss, a spot size converter (SSC) (cf. Fig. 5.3a) is integrated into the modulator for an efficient fiber/chip coupling.

Theoretical calculations showed that for the length of the spot size converter transformation efficiencies from the fiber port waveguide to the chip waveguide of up to 90% can be achieved by proper design of the taper ramp. The measured improvement of the insertion loss compared to coupling with tapered fibers is about 4 dB [1].

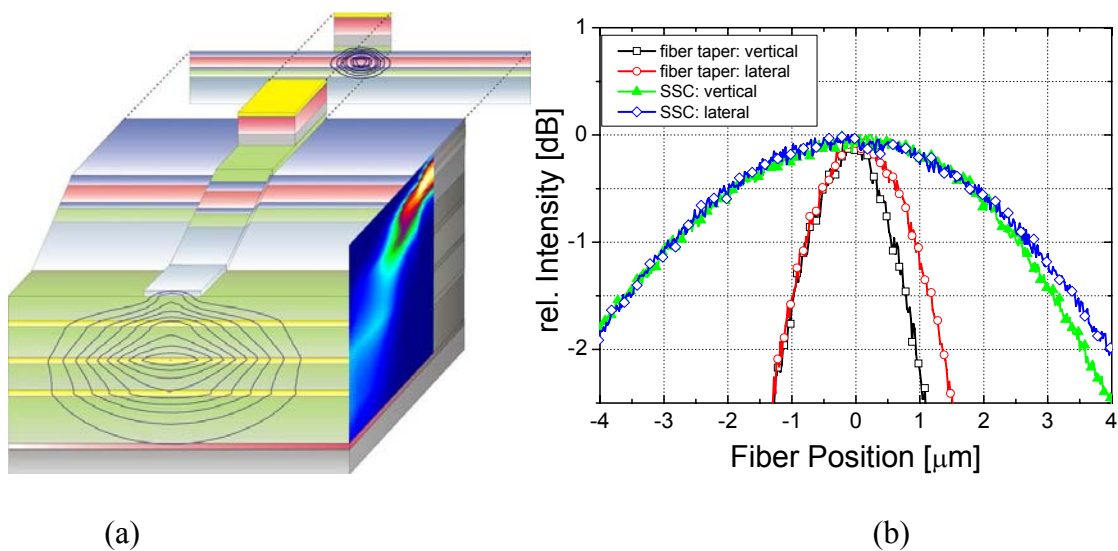


Fig. 5.3 (a) A 3-D model of the spot size converter with field distribution for the fundamental mode in the passive and fiber port waveguide, respectively (b) Alignment tolerances measured at the input port of the modulator compared to that of the tolerances of a tapered fiber to a passive waveguide [1]

The successful function of the SSC is shown also by the improved alignment tolerances to a standard single mode fiber in Fig. 5.3(b). Submicron precision is required to align a tapered fiber to the chip waveguide for 0.5 dB excess loss. With the

integrated SSC a shift of 2  $\mu\text{m}$  of the fiber is tolerable for the vertical and horizontal direction, respectively. Furthermore, the SSC simplifies the excitation of the basic waveguide mode. It works as a mode filter in this configuration [1].

### 5.2.2 The Module

Fig. 5.4 shows CAD model of a modulator module in detail. The modulator is packaged in a metal box. On the right side of the box are two V connectors which can operate up to 65 GHz. On the left side, six pins are reserved for the bias, DC control signal and ground. Optic fibers are located on the other two sides, to take advantage of the integrated SSC, the joint between the fiber and the optical waveguide of the chip is butt coupled. The chip is put in the center of metal box. Inside the box, two coaxial cables are used to combine the V connector and input and output ports of the chip. Under the chip, an integrated Peltier element and an NTC resistor are implemented to stabilizing the working temperature.

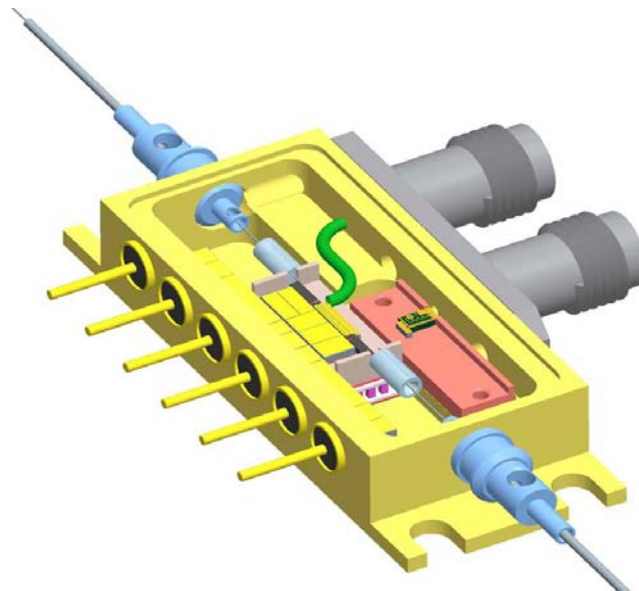


Fig. 5.4 The CAD drawing of a packaged modulator module

### 5.2.3 Electrical Bonding and Connection

The packaged device performance is primarily depend on the chip performance, however, for the device whose work-speed is about and above 40 Gbit/s, the electrical bonding and connecting in the module should not be neglected. Therefore, in order to approach the chip performance, the electrical connection in a packaged module must be designed carefully. Fig. 5.5 shows the insertion loss of a modulator before and after packaging, in which the electrical connection was not designed properly. In the figure, the red curve describes the insertion loss of the modulator chip; the blue curve describes the insertion loss after packaging. In this example, the 6 dB point of electrical insertion loss shrinks from 45 GHz to 20 GHz after packaging.

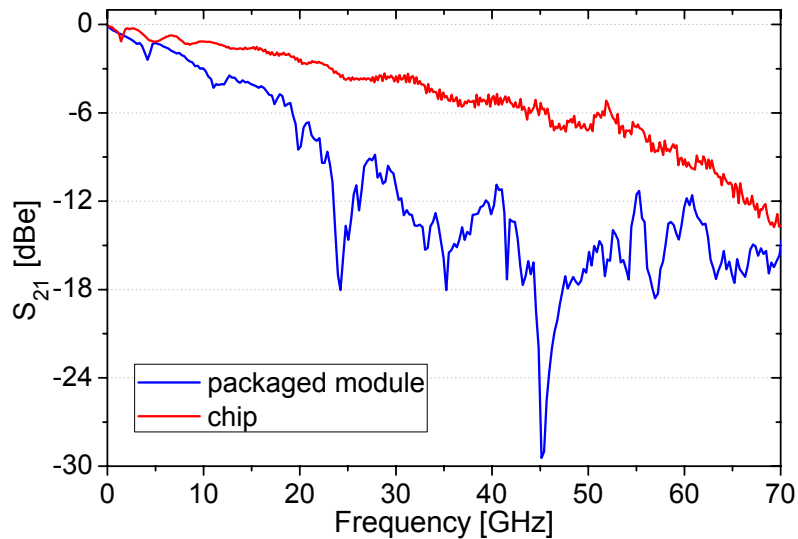


Fig. 5.5 Measured electrical loss  $S_{21}$  of a modulator before and after packaging

To study this problem, a simplified 3-D model of a packaged module (cf. Fig. 5.6, Fig. 5.7(a) and Fig. 5.7(b)) was established in HFSS. It is introduced that in the packaged module two coaxial cables are used to connect the V connectors and the chip. However, it is technologically difficult to connect the chip and the coaxial cable directly. Therefore, there is a middle block between them which is composed of  $\text{Al}_2\text{O}_3$ -

ceramic. The middle block is covered by metal. As a transmission line, it has the characteristic impedance of  $50 \Omega$ . The coaxial cable is stuck to the one side of the middle block through conducting resin. On the other side, the middle block is connected with the modulator chip by bonding wires. The geometry parameters of the model are based on the module which has been tested.

In Fig. 5.7(c), the measured and the simulated curves are presented. The simulation result fits the measured data. It can be concluded that the simple model has characterized the losses of the packaged module. Therefore, on the basis of this model, one can optimize the connection between the chip and the V connector to achieve a better module performance.

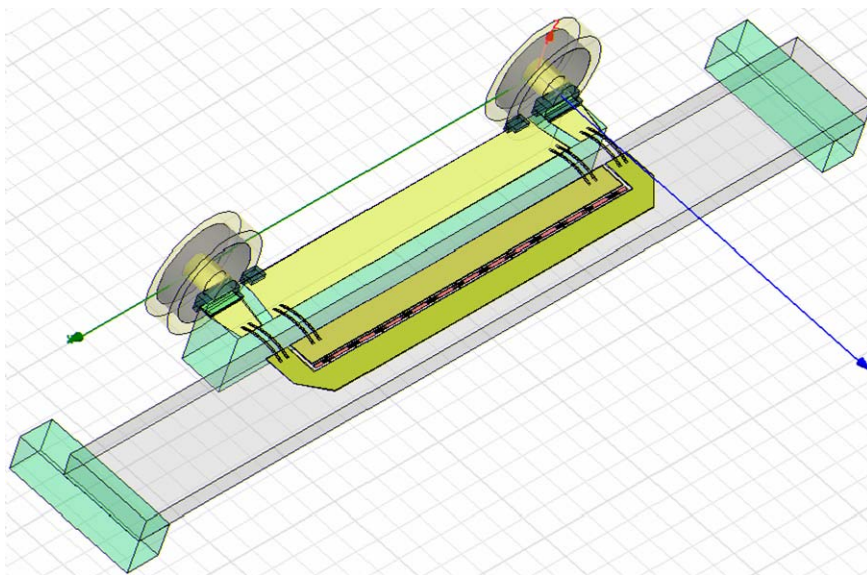
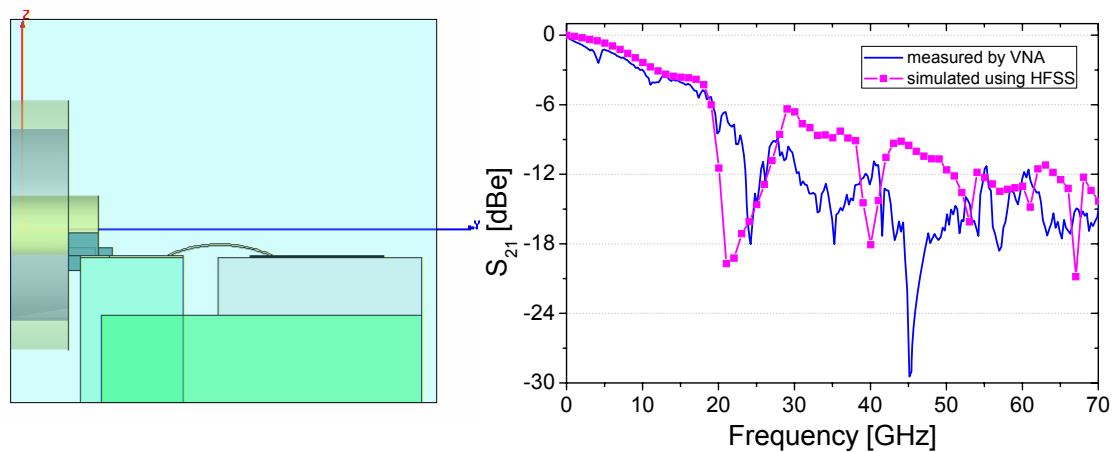


Fig. 5.6 A simplified 3-D model in HFSS



(a) Top-view of a 3-D model of packaged module



(b) Side-view of the model

(c) Measured and simulated insertion loss

Fig. 5.7 Top-view and side-view of the 3-D model of a packaged module and simulation results

The study shows that the long bonding wires between the middle block and the chip, and the abrupt signal transition from a symmetry structure (coaxial cable) to an asymmetric interface (CPS), are two sources of extra losses that make the performance of the packaged module different from that of the chip.

To improve the module's performance, the distance between the middle block and the chip should be as short as possible. This requires that the margin between the chip side and the connecting pad is small, and the middle block is placed so carefully that it can abut on the chip. By these means, the distance can be shortened to 50-70  $\mu\text{m}$ . If possible, increasing the number of the bonding wires can also reduce the parasitic inductance (cf. Fig. 5.8).

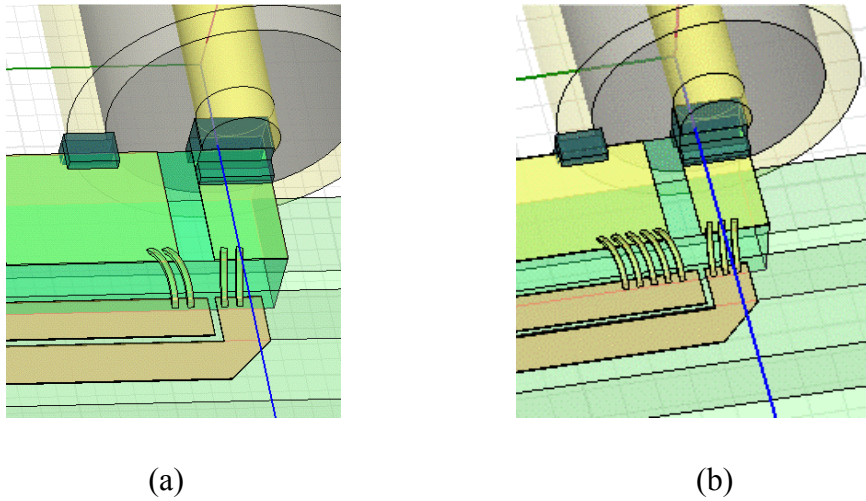


Fig. 5.8 Bonding wires (a) two bonding wires for each connection, (b) five bonding wires for ground and three for signal

The transition from an asymmetric CPS to a symmetric structure is not avoidable because of the inherent electrical modulator structure. However, the transition can be optimized so that the extra loss could be suppressed [2]. The transition can be arranged inside the chip as well as outside the chip. To simplify the packaging process, an inside transition section is designed (cf. Fig. 5.9) and CPWs are used as symmetrical input and output ports of the chip.

As shown in Fig. 5.9, the proposed transition connects CPS with CPW by the air-bridge structure. Two ground planes of the CPW port are connected at their ends by a short gold line which is only 100 nm thick. With a height of 2.5  $\mu\text{m}$  the signal line of the CPW passes over the short thin connection between two grounds and is connected to the signal electrode of the modulator.

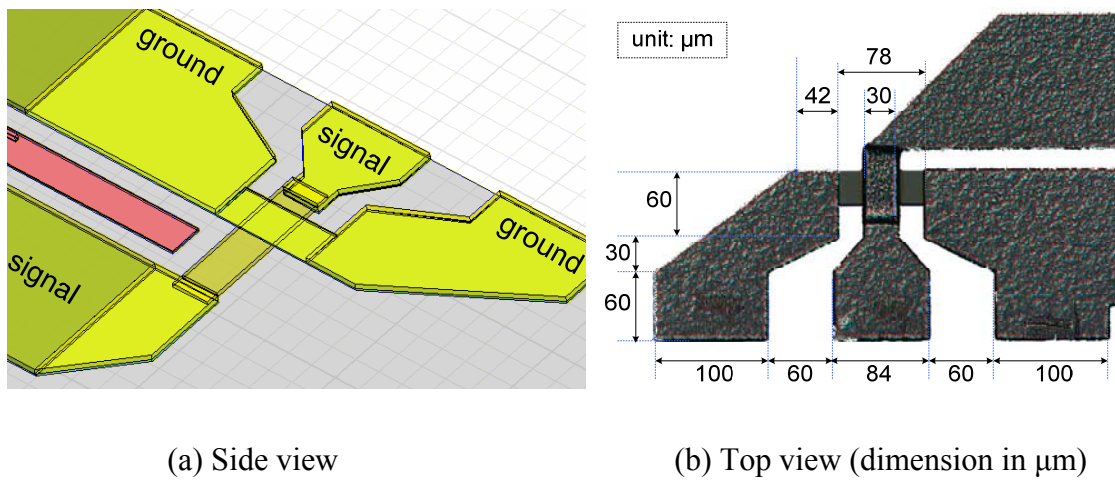


Fig. 5.9 An optimized integrated CPS-CPW transition in a modulator

To study the performance of this transition and compare it with the structures without such transitions, three 1 mm CPS test-structures have been designed and fabricated (cf. Fig. 5.10 (a)-(c)). Two of them do not contain the transitions and are with right-angled bends at both ends, the one, type A, is so-called asymmetric (cf. Fig. 5.10 (a)), because the signal strip is longer than the ground strip, the other one, type B, is symmetric (cf. Fig. 5.10 (b)). The third one, type C, uses two transitions on both ends, and the input/output ports are CPW ports.

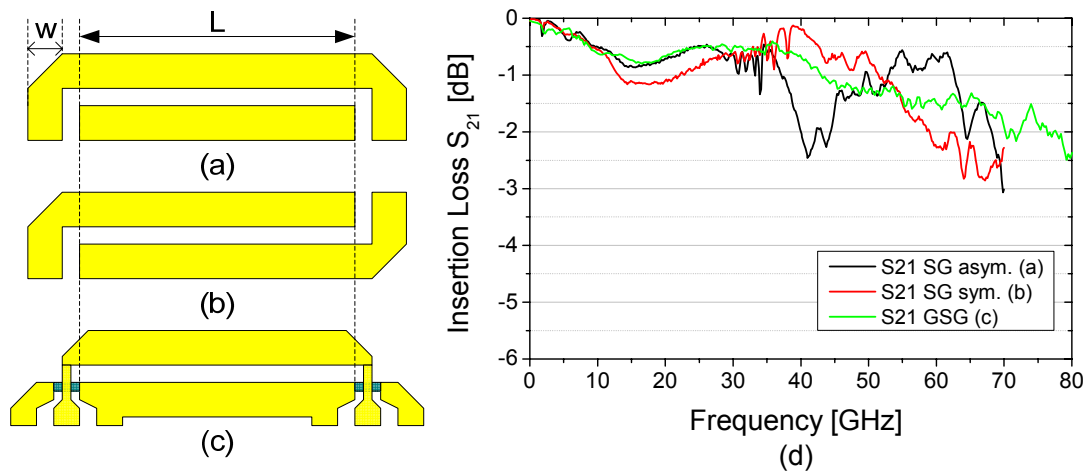


Fig. 5.10 Three different configurations of input and output pads (a) asymmetrical S-G configuration, (b) symmetric S-G configuration, (c) G-S-G pads, (d) measured electrical insertion losses of the three different configurations

To measure these three test structures needs three different pairs test probes, namely S-G, S-G; S-G, G-S and G-S-G, G-S-G, for type A, B and C respectively. Each pair of test probes should be calibrated. The measured results, which are shown in Fig. 5.10(c), show that these three test structures have similar performance. Comparing curve (a) and (b) to (c), one can see that the CPS-CPW transition doesn't induce obvious extra insertion loss.

The ground ring in the module, which is composed of the ground bar on the middle block and ground strip of the modulator, induces the parasitic resonance. To avoid this resonance, one can either connect these two strips by uniform-spaced metal bridges (cf. Fig. 5.11), or cut the ground bar on the middle block into 2 parts (cf. Fig. 5.12). Fig. 5.13 shows the calculated insertion loss of the modules as shown in Fig. 5.11 and Fig. 5.12, and compares them to that of the chip. After optimizing, the module electrical performance is much better than before and is close to that of the chip. This packaging technology ensures the 40 Gbit/s modulator's performance and can be further used for 80 Gbit/s modulator modules.

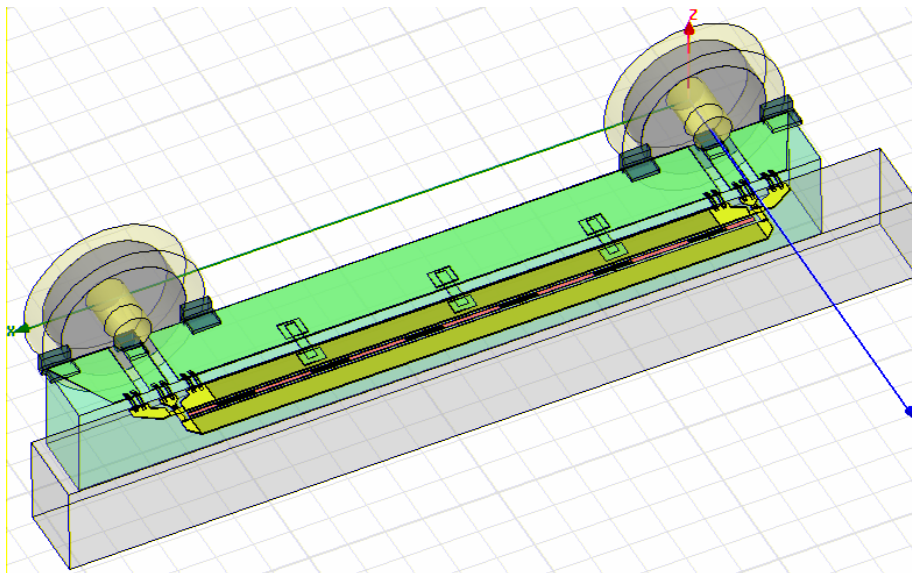


Fig. 5.11 The module using G-S-G pads with long ground bar on the middle block

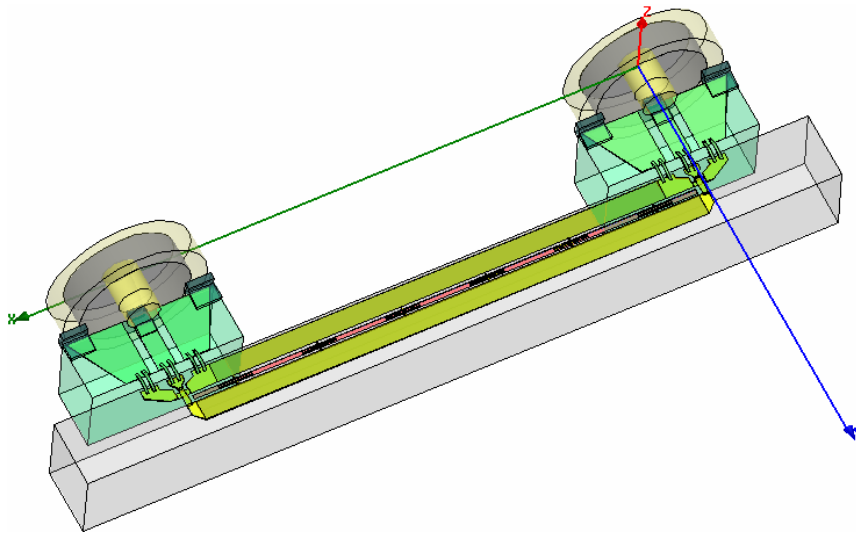


Fig. 5.12 The module using G-S-G pads with separated middle blocks

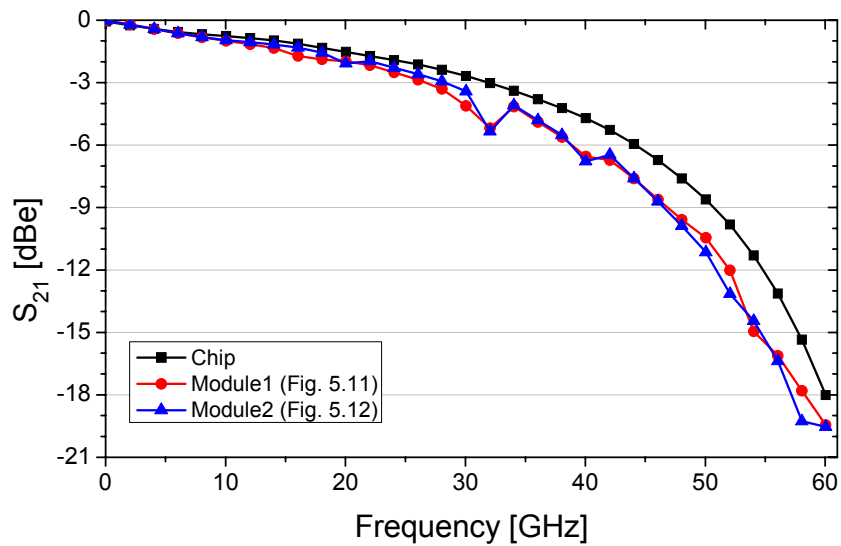


Fig. 5.13 Simulated electrical insertion loss  $S_{21}$  of a modulator before and after optimized packaging

## REFERENCES

- [1] D. Hoffmann, S. Staroske and K.-O. Velthaus, "45 GHz bandwidth travelling wave electrode Mach-Zehnder modulator with integrated spot size converter", IPRM2004, (2004)
- [2] S.Kim, S. Jeong, Y.-T. Lee, D.-H. Kim, and K.-S. Seo, "Ultra-wideband (from DC to 110 GHz) CPW to CPS transtion", Electronics Lett. **38** 622-623 (2002)

## Chapter 6

### Characterization of Modulators and Measurements

#### 6.1 C-V CHARACTERISTIC MEASUREMENT

In order to identify the bias-dependent depletion capacitance of the p-i-n structure in the modulator, the capacitance–voltage (C–V) characteristic measurement was carried out on a probe station using an HP 4275A multi-frequency LCR meter. Open and short calibration procedures were accomplished in order to remove the influence of the probes and cables.

Since it is difficult to directly measure the C-V characteristic in the segmented modulator device, a series of circular diodes (diameter  $d = 50 \mu\text{m}$ ,  $100 \mu\text{m}$ ,  $150 \mu\text{m}$ ,  $200 \mu\text{m}$ ) with known area ( $A = 707 \mu\text{m}^2$ ,  $7,854 \mu\text{m}^2$ ,  $1,7671 \mu\text{m}^2$ ,  $31,416 \mu\text{m}^2$ ) were made on the modulator wafer (cf. Fig. 6.1) which have the same p-i-n structure as the modulators. The measured C-V curves are shown in Fig. 6.2.

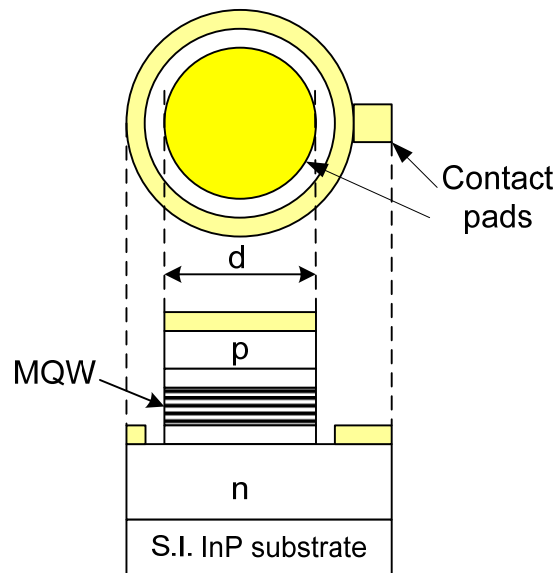


Fig. 6.1 The circular diode test structure: top view and cross sectional view.

The C-V characteristic measurement can also be used to identify the bias-dependent effective thickness of the depletion layer  $d_{pin}$ , in the p-i-n structure which is an important structure parameter in the HFSS simulation. Equation (2.4.13) can be applied to calculate  $d_{pin}$  using the measured capacitance of a diode with known area and dielectric constant.

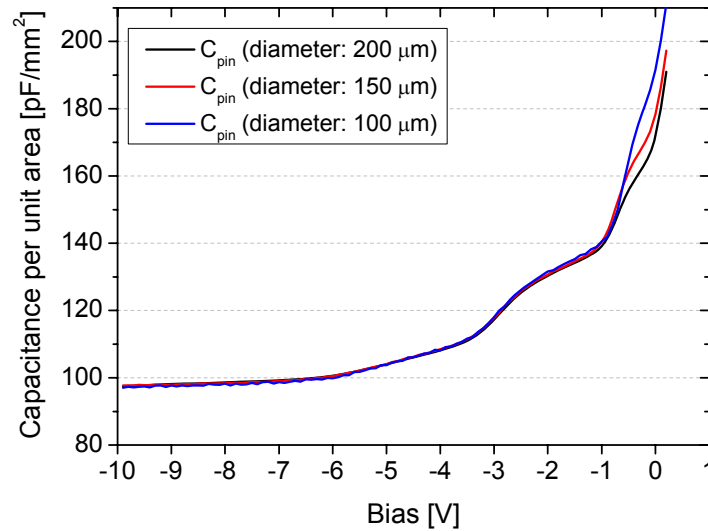


Fig. 6.2 Measured C-V characteristic of round diodes

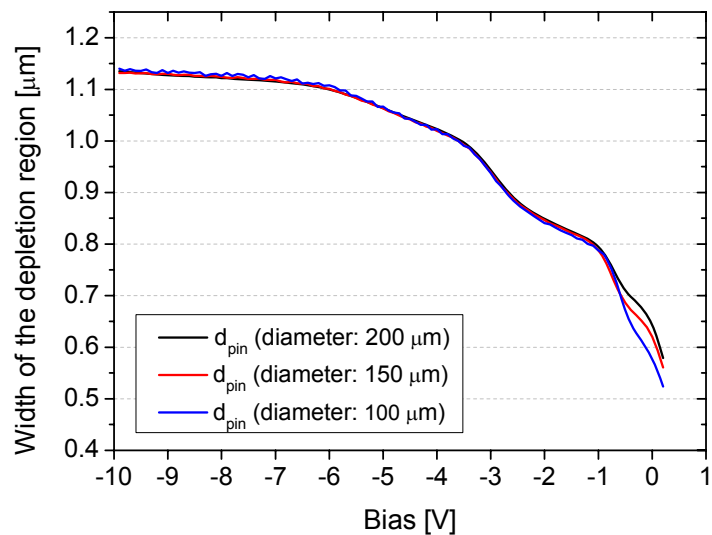


Fig. 6.3 Intrinsic layer thickness over bias voltage deduced from C-V measurements

In the analysis, the static dielectric constant of InP was used which may slightly underestimate  $d_{pin}$ , especially in the case of a partly quaternary depletion region.

Fig. 6.3 gives the resulting intrinsic layer thicknesses for the fabricated wafers. The depletion layer thickness increases with higher reverse bias which can be attributed to some residual background doping ( $10^{15} \text{ cm}^3 \sim 10^{16} \text{ cm}^3$ ) of the not intentionally doped (n.i.d.) layers. From the above measured data, the loading capacitance of the modulator is 120 pF/m, 150 pF/m and 180 pF/m at  $V_{\text{bias}} = -6 \text{ V}$ , respectively, estimated by appropriate scaling of the active area with corresponding fill factor,  $\eta$ , 0.4, 0.5 and 0.6, respectively.

## 6.2 MEASUREMENT OF THE P-CONTACT RESISTANCE

As discussed in Chapter 4, the p-contact resistance in the modulator is a decisive parameter for the high frequency performance of a MZI modulator. Higher p-contact resistance will induce a higher microwave loss in a modulator and can correspondingly cause a lower 6 dB<sub>e</sub> frequency. Therefore, it is necessary to identify this p-contact resistivity  $\rho_c$ .

A series of test structures (cf. Fig. 6.4) was made on the same wafer with the modulators because it is impossible to directly measure the value in a modulator.

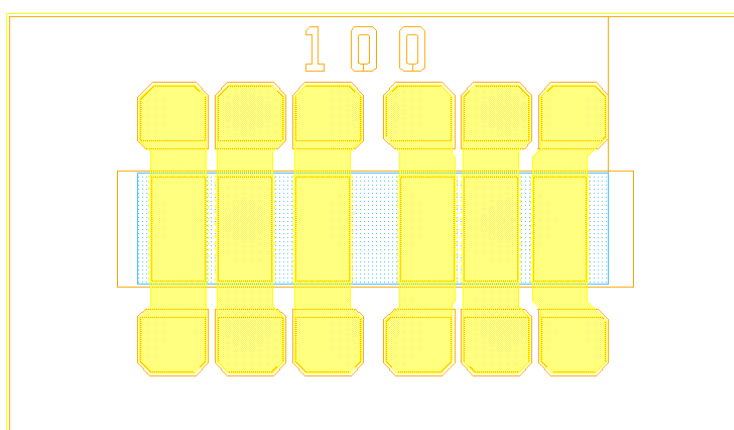


Fig. 6.4 Layout of one TLM structure ( $w_c=100 \mu\text{m}$ )

The contact resistance was then measured, using the transmission line method (TLM), which relies on resistance measurements between a series of pads with varying spacing.

The measurements require simple I-V curves. This was done with a probe station and a parameter analyzer like HP4142B using the Kelvin measurement method [1]. Four probes are needed to accurately measure the resistance between any two contacts, two to provide a current between the pads, and two to measure the voltage between them. Since essentially no current could flow between the voltage monitoring probes due to high internal resistance, their measured voltage was only the difference between the two pads, independent of other factors like the resistance due to the probe contacts with the metal surface themselves. From this the resistance between those two pads is calculated ( $R=V/I$ ), and a subsequent line fit to the I-V plot of each of the contact chains does then yield the resistance.

The corresponding contact resistivity was calculated using (2.5.6). Fig. 6.5 shows two series of p-contact resistivities, they are calculated from the measured data of two modulator wafers. Due to an extra post-doping process used in wafer MZ-MOD03, the contact resistivity was improved from  $0.9 \sim 2 \times 10^{-5} \Omega \cdot \text{cm}^2$  to  $2 \sim 6 \times 10^{-6} \Omega \cdot \text{cm}^2$ .

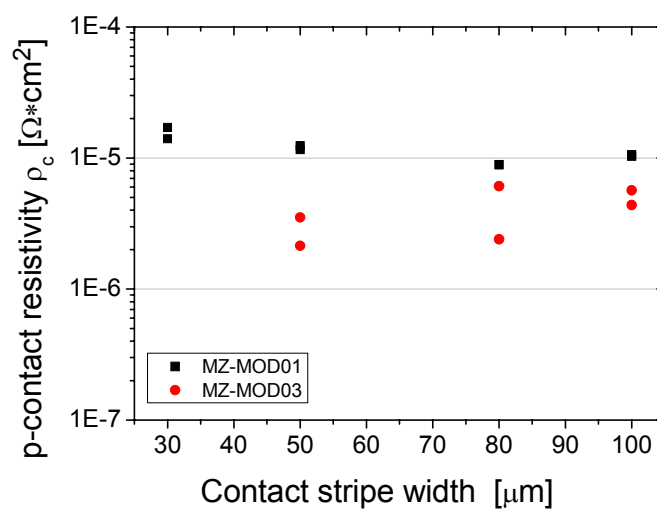


Fig. 6.5 Measured p-contact resistivities of two modulator wafers

### 6.3 DC MEASUREMENTS

Characterization of the DC properties is the first step to make sure whether a modulator can work properly or not. Fig. 6.6 shows the experimental setup.

The optical signal is supplied by a tunable external cavity laser (ECL) source (Photonetics Tunics Plus) whose wavelength ranges from 1460 nm to 1590 nm, and optic power is up to 4 mW. After the polarization adjuster, the optical signal is coupled into the modulator chip on a probe station through fiber.

On the other side, the output optical signal is either coupled into a fiber or received by a lens. At both sides, two mechanical 3-axes piezoelectric translation stages are employed to adjust the fiber or lens position in order to ensure the maximal coupling efficiency. Photodiodes are used on the end to transfer the optical signal to the electrical one, which is easier to sample and analyze by using a data-acquisition-card (NI DAQ) in a computer. After the lens a polarization filter is used to examine the polarization state of the optical signal. The beam received by the lens is partly inspected by an infrared camera which is connected to a monitor.

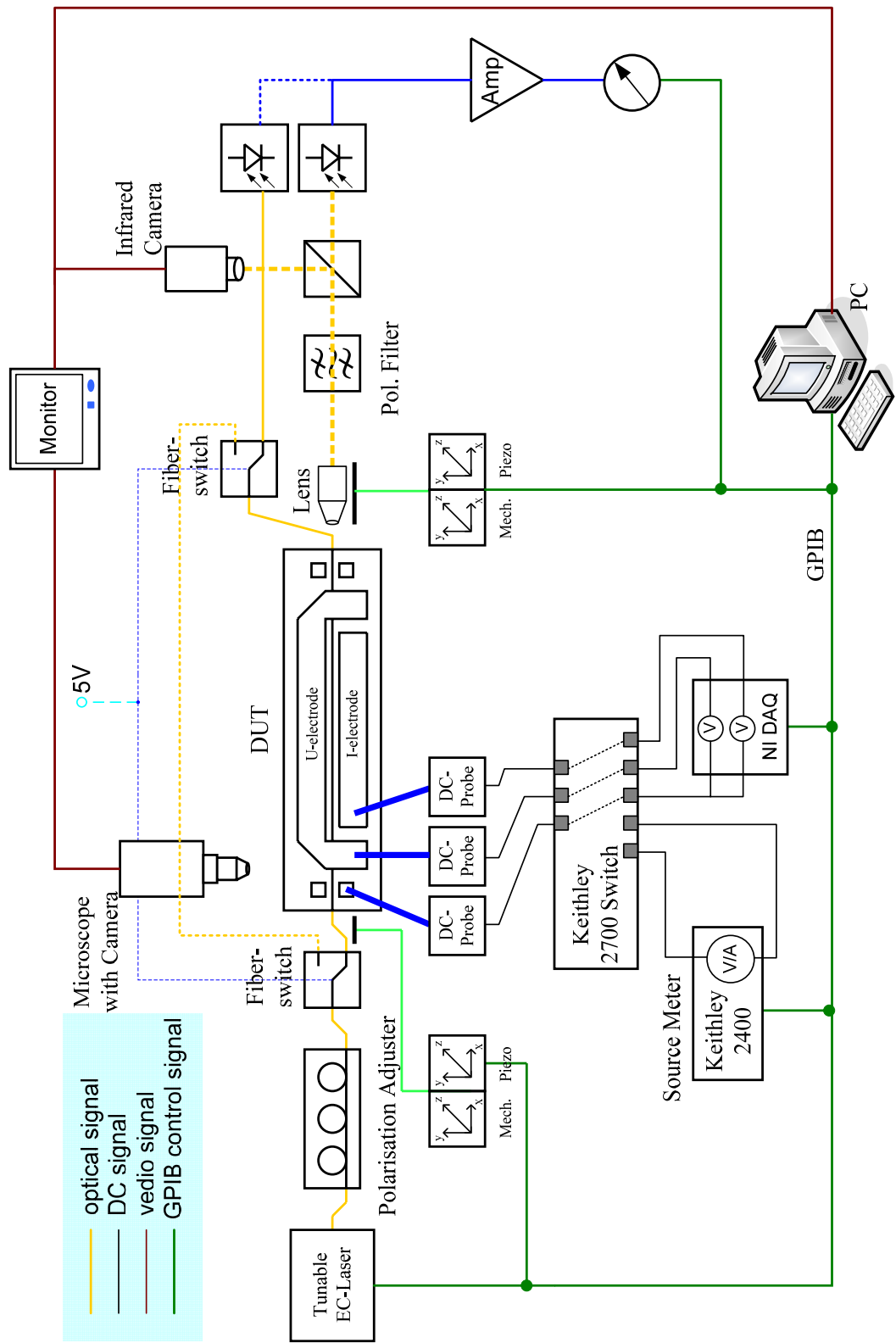


Fig. 6.6 Setup of DC matrix measurement [2]

DC probe heads are used to apply bias voltages on U-electrode and I-electrode of a modulator, respectively. The contacts can be controlled from the monitor which is connected to a microscope camera.

The DC characterizations include DC-matrix measurement and I-V characteristics.

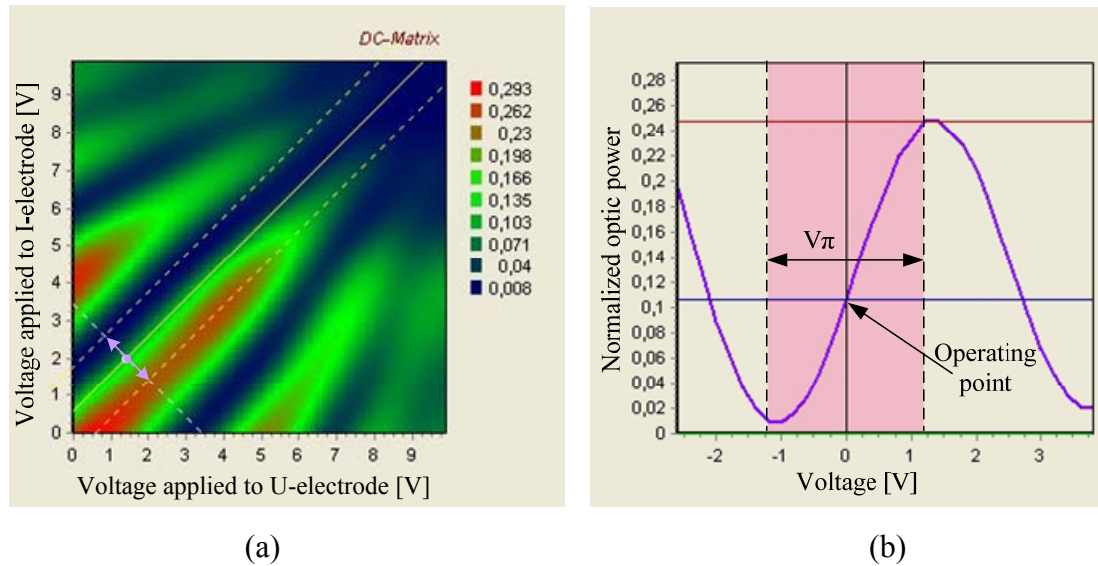


Fig. 6.7 (a) Normalized optical transmission with applied voltage to I- and U-electrode. (b) The transfer curve of the corresponding operating point in (a)

The DC-matrix as shown in Fig. 6.7 (a) illustrates the normalized optical transmission of a modulator with bias voltage applied to the I- and U-electrodes. It is measured for each output of a modulator with the reverse bias applied to each electrode varying from 0 V to 10 V, using a 1 mW (0 dBm) optical signal at wavelength of 1550 nm. From the DC-matrix, one can easily find the best operating point, at which the modulator has the optimum transmission characteristic. The transmission characteristic of the corresponding operating point in Fig. 6.7 (a) is shown in Fig. 6.7 (b).

## 6.4 S-PARAMETER MEASUREMENT

The transmission line properties of the travelling wave electrode Mach-Zehnder modulator were analyzed on-wafer in the frequency range from 45 MHz to 70 GHz with a vector network analyzer (VNA) HP 8510XF. S-G probe heads were used for contact at the input and output ports. The SOLT (Short, Open, Load, Thru) calibration method was used in on-wafer calibration.

The VNA HP 8510XF operates up to 110 GHz, but the frequency range of our measurement was limited to 70 GHz by the S-G probe heads. As discussed in Chapter 5, if the new G-S-G pads were integrated in the modulator, the S-parameter measurement could be extended to 110 GHz, which should be enough for the characterisation of a 100 Gbit/s modulator.

## 6.5 ELECTRO-OPTIC MEASUREMENT

Fig. 6.8 shows the experimental setup of the electro-optical small signal response measurement. The laser signal is provided by an ECL. A polarization controller is used after ECL in order to ensure the incident light to be TE polarized.

At the input side, the laser signal is coupled into the modulator through a butt joint. The fiber position is carefully adjusted to transfer maximum light into the modulator which is placed on a probe station. The electrical modulating signal comes from an RF signal generator (Agilent E8257D 0-65GHz) and is applied onto the modulator through an S-G probe. The modulating signal's power is kept constant at a level of -7 dBm.

At the output side, the modulated optical signal is coupled into a fiber again through a butt joint and is amplified by an erbium doped fiber amplifier (EDFA). To minimize the ASE (amplified spontaneous emission) noise, the EDFA is followed by a tunable optical bandpass filter. An integrated power meter is used to read out the optical power. Finally, the modulated optical signal is injected into a photodiode, the

output of the photodiode is introduced into an electrical spectrum analyzer (Agilent E8565EC, frequency ranges from 200 MHz to 50 GHz). Since the frequency range is limited to 50 GHz by the electrical spectrum analyzer, an external Preselected Millimeter Mixer (Agilent 11974V, from 50 GHz to 65 GHz) is used to extend the upper frequency from 50 GHz to 65 GHz which is necessary for the measurement of an 80 Gbit/s modulator.

Two source meters (Keithley 2400) are employed to provide asymmetric bias voltages to the modulator. The modulator is electrically terminated with a 50  $\Omega$  resistor.

The test instruments are all controlled by a computer through connected general purpose interface bus (GPIB) cables. The complicated electro-optical small signal response measurement is partly automated by a special test program.

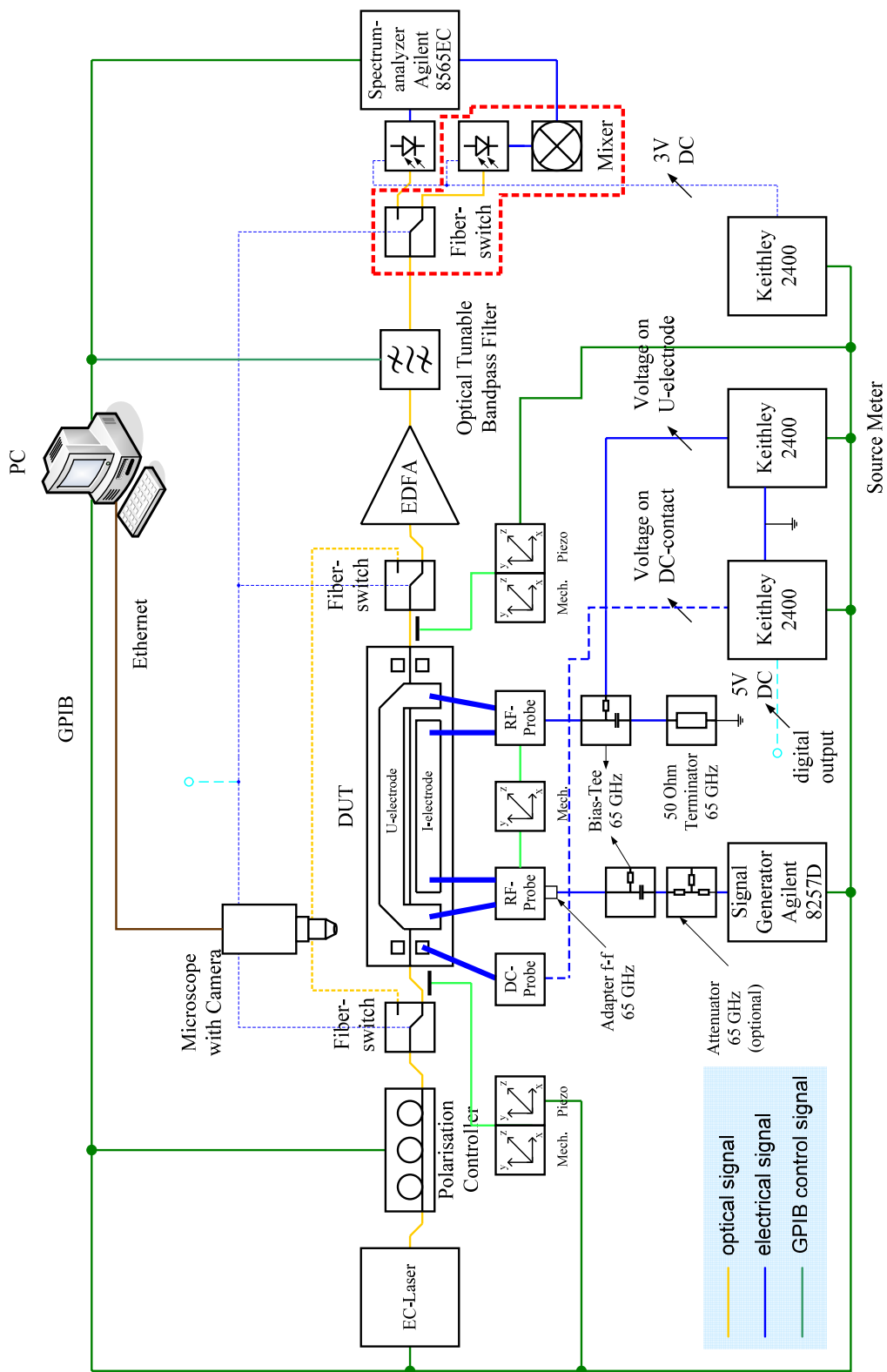


Fig. 6.8 The setup of electrooptic response measurement (200 MHz – 65 GHz) [3]

## 6.6 SYSTEM MEASUREMENTS

As shown in Fig. 6.9, the 40 Gbit/s eye diagram is measured using an Agilent 86100B oscilloscope with a precision time base (Agilent 86107A) and a dual 70+ GHz electrical remote head (Agilent 86118A). To generate the  $2^{31}-1$  PRBS (pseudorandom binary sequence) pattern with bit rates of 40 Gbit/s as the input signal for the module, a pattern generator (SHF BPG 4×11) and a multiplexer (SHF 5005A 4×1) are used together with an electrical amplifier (SHF 804EA).

An optical amplifier (EDFA) at the output of the modulator ensured a constant optical power level of +7 dBm at 1.55  $\mu\text{m}$  on the high speed photodiode (u<sup>2</sup>t, XPDV2020R) when the optical input power on the modulator varies. An optical filter is used to reduce EDFA-ASE noise.

To measure 80 Gbit/s eye diagrams, an 80 Gbit/s 2:1 multiplexer is inserted between the 4:1 multiplexer and the electrical amplifier as shown in Fig. 6.10. The *data* and  $\overline{\text{data}}$  outputs of the 4:1 multiplexer are used as two input data signals for the 2:1 multiplexer. A 40 GHz clock source is used instead of the 20 GHz one in 40 Gbit/s system measurements.

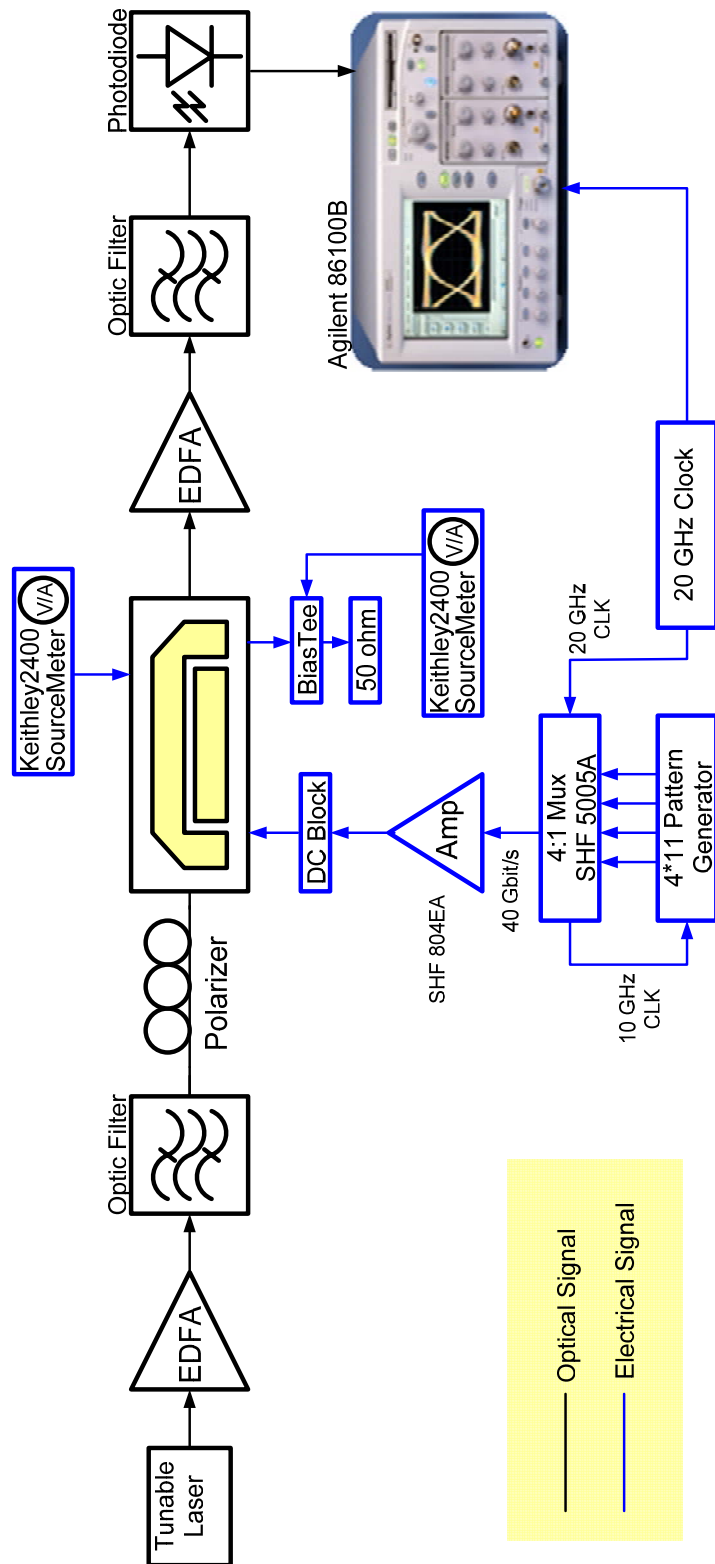


Fig. 6.9 Setup for 40 Gbit/s eye-diagram measurements of modulator

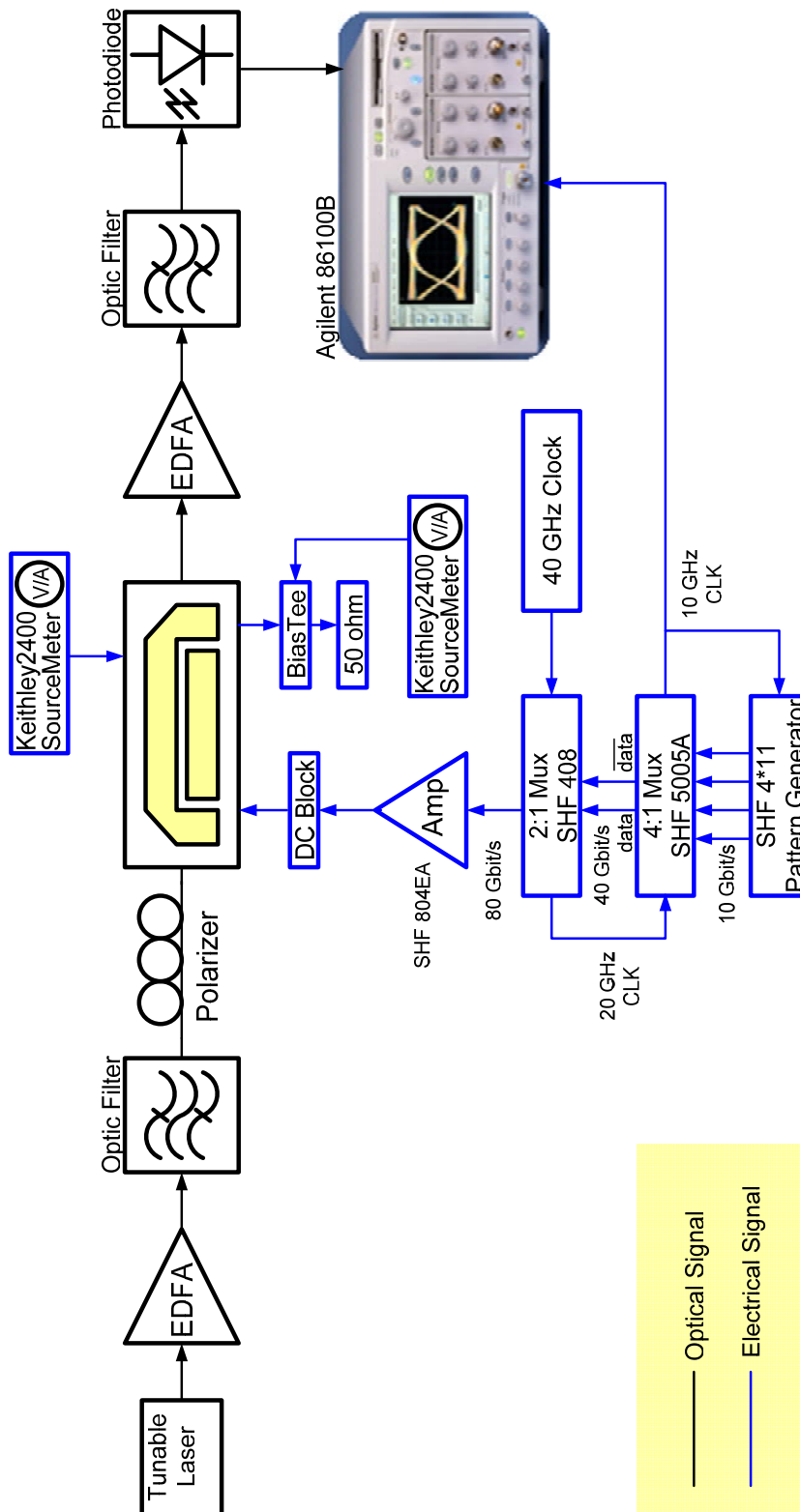


Fig. 6.10 Setup for 80 Gbit/s eye-diagram measurements of modulator

## REFERENCES

- [1] D. K. Schroder, "Semiconductor material and device characterization", 3<sup>rd</sup> Ed., Wiley (2006)
- [2] Klein Holger, "Vergleichende Analyse elektrooptischer Effekte in Multi-Quantenfilm- und Bulk-Schichten zur Realisierung von InP-Mach-Zehnder-Modulatoren für 40 Gbit/s", Diplomarbeit, TU-Berlin (2004)
- [3] Daniel Kunowski, "Erweiterung und Klassifizierung eines Hochfrequenzmessplatzes für Mach-Zehnder-Modulatoren bis 65 GHz", Diplomarbeit, TFH-Berlin, (2006)

## Chapter 7

### Measured Results and Conclusions

In this chapter, the experimental results of a packaged InP-based MQW TWE MZM and an InP-based MQW TWE MZM chip are presented. These results show that the designed InP-based MZI modulators can work properly in 40 Gbit/s optic communication systems as well as in 80 Gbit/s ones.

#### 7.1 MEASURED RESULTS OF MODULATOR

Due to the continuing optimization work for the high-speed modulator, we have a few modulators from different wafers which achieved 80 Gbit/s. Some of them have been packaged, and the newly produced modulators which have exhibited a better performance will be packaged later.

##### 7.1.1 Measured Results of the First Generation 80 Gbit/s Modulator

A 10 mm long InP based MZI modulator chip (#45 A50) with a TWE electrode length of 4 mm was packaged into a fiber pigtailed module (cf. Fig. 7.1). The period length  $\Lambda$  of the modulator is 125  $\mu\text{m}$ , and the active electrode length  $l_E$  per period is 62.5  $\mu\text{m}$ . The chip is fixed on a ceramic submount and connected to V-type RF connectors via semi-rigid coaxial cables. The RF power is fed into the left V-type RF connector. The right output connector is used for an external 50  $\Omega$  terminator. An integrated Peltier element and an NTC resistor were additionally implemented for temperature stabilization.



Fig. 7.1 A packaged modulator module [1]

Fig. 7.2 shows the normalized output vs. driving voltage of the module with a  $V_{\pi}$  of 2.6 V at an applied bias of -2.8 V.

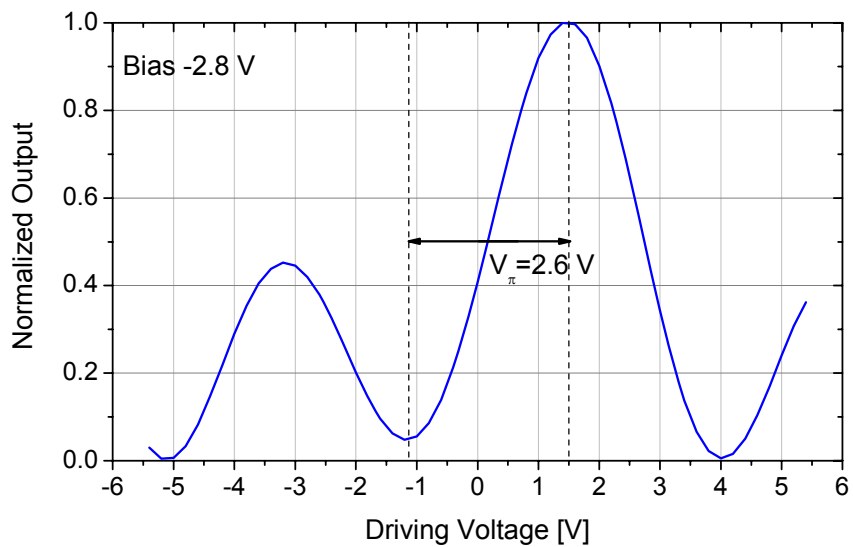


Fig. 7.2 Normalized output vs. driving voltage of the module (#45 A50) at -2.8 V bias

The 3 dB<sub>eo</sub> bandwidth of the packaged modulator is 45.6 GHz as can be seen in Fig. 7.3 which shows its small signal electro-optic response.

A clear open NRZ eye diagram at 40 Gbit/s has been measured at -2.8 V bias indicating a dynamic extinction ratio of 12 dB and an rms jitter of 881 fs (cf. Fig. 7.4).

The rms jitter of the electrical amplifier signal was typically 700 fs suggesting that the modulator does not increase the rms jitter too much.

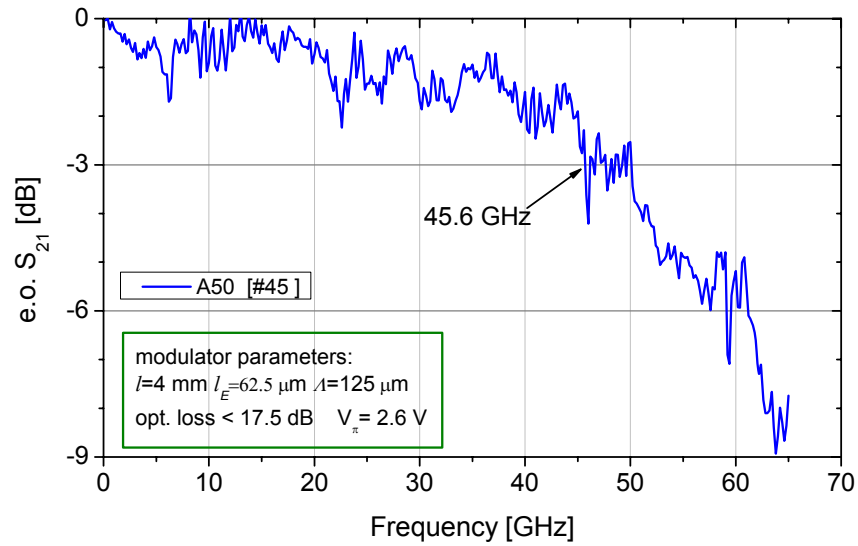


Fig. 7.3 EO response of the packaged MZI modulator (#45 A50) at -2.8 V bias [1]

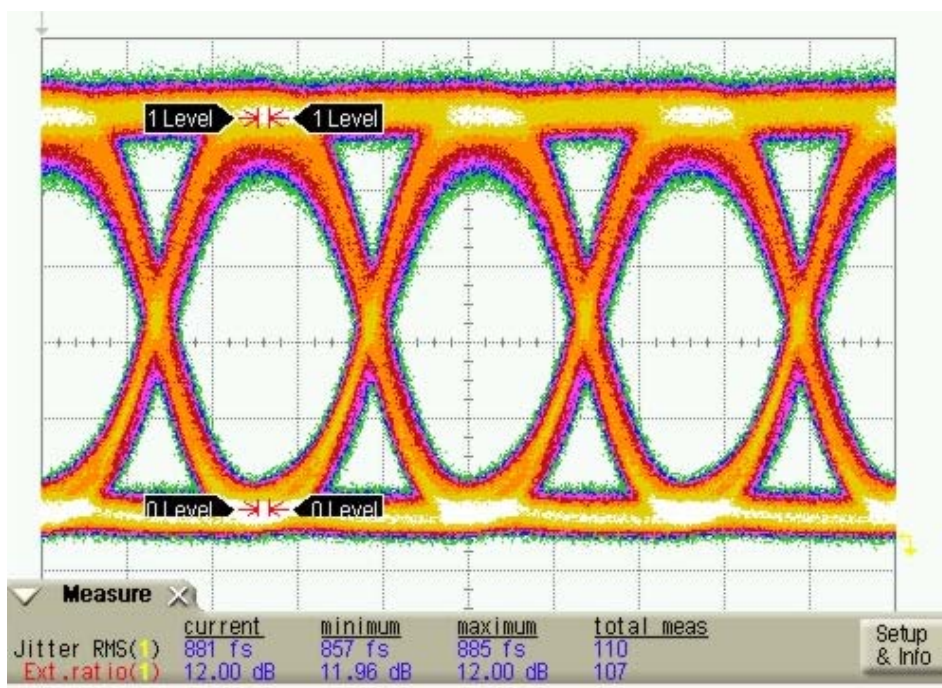


Fig. 7.4 Measured NRZ eye diagram of the packaged MZI modulator (#45 A50) at 40 Gbit/s with 1.55  $\mu\text{m}$  optical signal (PRBS word length:  $2^{31}-1$ , 10 ps/div) [1]

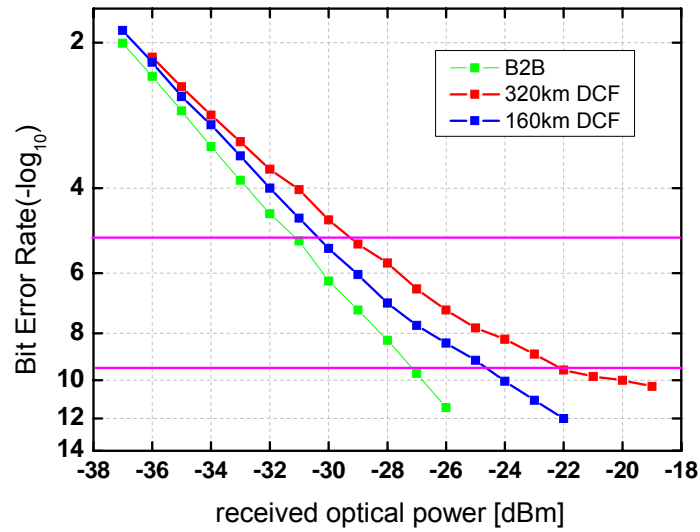


Fig. 7.5 Measured 40 Gbit/s PRBS BER curves of the packaged modulator (#45A50)

Fig. 7.5 shows the measured bit error rate (BER) curves under 40 Gbit/s operation for back-to-back (B2B) connection, after 160 km, and after 320 km transmission, respectively, in an optic transmission system. Error free operation can be expected down to an optical power of -26 dBm for a B2B configuration.

Fig. 7.6 shows the large signal performance of this packaged modulator under 80 Gbit/s operation. An open NRZ eye diagram has been measured at -4.5 V bias indicating a dynamic extinction ratio of >8 dB.

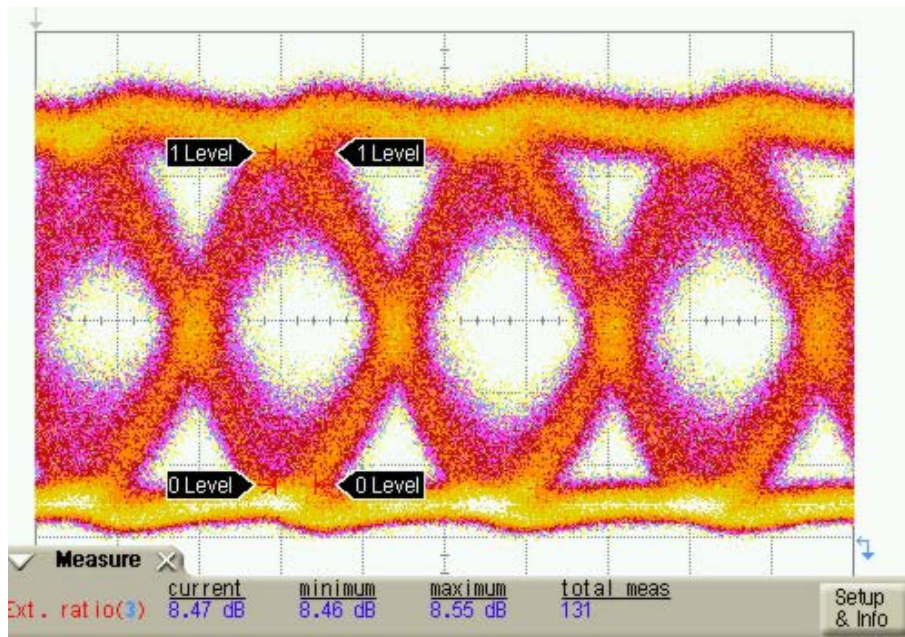


Fig. 7.6 Measured NRZ eye diagram of the packaged MZI modulator (#45 A50) at 80 Gbit/s with 1.55  $\mu\text{m}$  optical signal (PRBS word length:  $2^{15}-1$ , 5ps/div)

### 7.1.2 Measured Results of the Second Generation 80 Gbit/s Modulator

The second generation modulator has a better p-contact. As shown in Fig. 6.5, the p-contact resistivity for the second generation is  $6 \times 10^{-6} \Omega \cdot \text{cm}^2$ , compared to the first generation of  $2 \times 10^{-5} \Omega \cdot \text{cm}^2$ .

The electro-optical small signal response has been measured up to 65 GHz. Fig. 7.7 shows an improved 3 dB<sub>eo</sub> bandwidth of 57 GHz for 4 mm long Mach-Zehnder modulators at a bias voltage of -6 V. This bandwidth is suitable for an 80 Gbit/s operation using NRZ singals. This is also the best experimental result so far. The sharp roll-off of the curve after 55 GHz is caused by the Bragg phenomenon. This can be prevented by using a shorter period length during the design as discussed in Chapter 4.

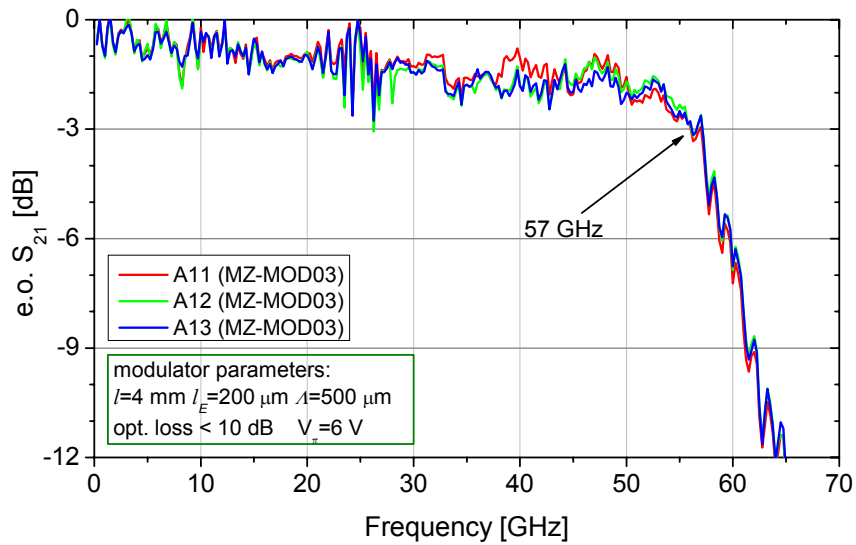


Fig. 7.7 Electro-optical response of a modulator (on-chip) with a TWE length of 4 mm. ( $l_E=200$   $\mu\text{m}$ ,  $\lambda=500$   $\mu\text{m}$ , -6 V bias)

## 7.2 CONCLUSIONS AND OUTLOOK

A packaged InP based Mach-Zehnder Modulator with 4 mm long traveling-wave electrodes and a  $V_{\pi}$  of 2.6 V at -2.8 V bias has been realized. It has a clear open eye diagram with a dynamic extinction ratio of 12 dB and an rms jitter of 881 fs under 40 Gbit/s NRZ operation. An eye diagram with a dynamic extinction ratio of 8.5 dB under 80 Gbit/s NRZ operation has also been shown. To the best of our knowledge, this is the first time that 80 Gbit/s data transmission is reported for an ETDM fiber optical transmitter with NRZ signal from a packaged InP-based MZI modulator.

The second generation modulators with a traveling-wave electrode length of 4 mm show 57 GHz electro-optical bandwidth which should be suitable for the 80 Gbit/s NRZ signal modulation. The optical insertion loss has also been controlled to less than 10 dB. Due to the missing 80 Gbit/s multiplexer and demultiplexer, the corresponding 80 Gbit/s system test could not be included in the work presented here.

An analysis of the recently produced modulators indicates that further optimization of the modulator may be possible in order to approach expected future standard system bit rates of 100 Gbit/s, such as the developing 100 G Ethernet.

## REFERENCE

- [1] H. N. Klein, H. Chen, D. Hoffmann S. Staroske, A. G. Steffan, and K.-O. Velthaus, "1.55  $\mu\text{m}$  Mach-Zehnder Modulators on InP for optical 40/80 Gbit/s transmission networks", Proceed. 18<sup>th</sup> Int. Conf. InP and Related Materials, IPRM2006 171-173 (2006)

## Appendix A The Scattering Matrix & the Transmission Matrix

### The scattering matrix

Consider the N-port network shown in Fig. A.1, where  $V_n^+$  is the amplitude of the voltage wave incident on port  $n$ , and  $V_n^-$  is the amplitude of the voltage wave reflected from port  $n$ . The scattering matrix, or  $[S]$  matrix, is defined in relation to these incident and reflected voltage waves as [1]

$$\begin{bmatrix} V_1^- \\ V_2^- \\ \cdot \\ \cdot \\ \cdot \\ V_N^- \end{bmatrix} = \begin{bmatrix} S_{11} & S_{12} & \cdot & \cdot & \cdot & S_{1N} \\ S_{21} & S_{22} & \cdot & \cdot & \cdot & S_{2N} \\ \cdot & \cdot & \cdot & \cdot & \cdot & \cdot \\ \cdot & \cdot & \cdot & \cdot & \cdot & \cdot \\ \cdot & \cdot & \cdot & \cdot & \cdot & \cdot \\ S_{N1} & S_{N2} & \cdot & \cdot & \cdot & S_{NN} \end{bmatrix} \begin{bmatrix} V_1^+ \\ V_2^+ \\ \cdot \\ \cdot \\ \cdot \\ V_N^+ \end{bmatrix} \quad (\text{A.1})$$

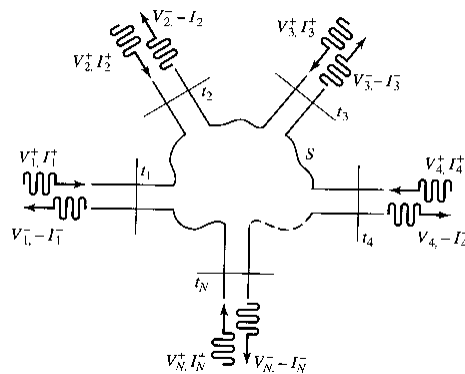


Fig. A.1 An arbitrary N-port network [1]

$S_{ii}$  is the reflection coefficient seen looking into port  $i$  when all other ports are terminated in matched loads, and  $S_{ij}$  is the transmission coefficient from port  $j$  to port  $i$  when all other ports are terminated in matched loads.

The scattering parameters can be directly measured by a vector network analyzer. Once the scattering parameters of the network are known, conversion to other matrix parameters can be performed, if needed [1].

### The transmission matrix

The transmission matrix is also called ABCD matrix and is defined for a two-port network in terms of the total voltages and currents as shown in Fig. A.2 and the following:

$$\begin{bmatrix} V_1 \\ I_1 \end{bmatrix} = \begin{bmatrix} A & B \\ C & D \end{bmatrix} \cdot \begin{bmatrix} V_2 \\ I_2 \end{bmatrix} \quad (\text{A.2})$$

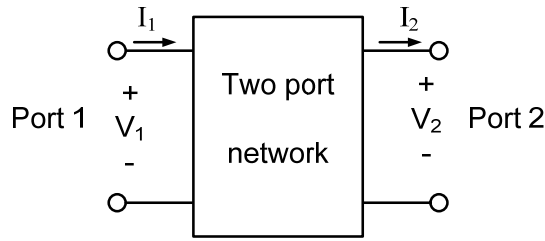


Fig. A.2 A two-port network

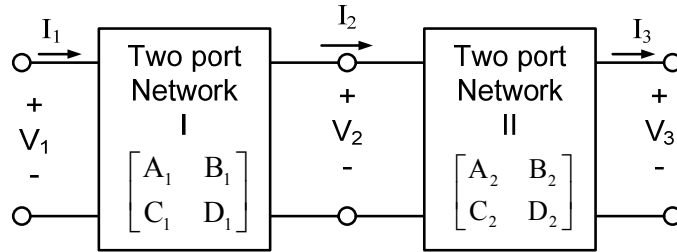


Fig. A.3 A cascade connection of two two-port networks

In the cascade connection of two two-port networks shown in Fig. A.3, we have

$$\begin{bmatrix} V_1 \\ I_1 \end{bmatrix} = \begin{bmatrix} A_1 & B_1 \\ C_1 & D_1 \end{bmatrix} \cdot \begin{bmatrix} V_2 \\ I_2 \end{bmatrix} \quad (\text{A.3})$$

$$\begin{bmatrix} V_2 \\ I_2 \end{bmatrix} = \begin{bmatrix} A_2 & B_2 \\ C_2 & D_2 \end{bmatrix} \cdot \begin{bmatrix} V_3 \\ I_3 \end{bmatrix} \quad (\text{A.4})$$

Substituting (A.4) into (A.3) gives

$$\begin{bmatrix} V_1 \\ I_1 \end{bmatrix} = \begin{bmatrix} A_1 & B_1 \\ C_1 & D_1 \end{bmatrix} \cdot \begin{bmatrix} A_2 & B_2 \\ C_2 & D_2 \end{bmatrix} \cdot \begin{bmatrix} V_3 \\ I_3 \end{bmatrix} \quad (\text{A.5})$$

which shows that the ABCD matrix of the cascade connection of the two networks is equal to the product of the ABCD matrices representing the individual networks. Note that the order of multiplication of the matrix must be the same as the order in which the networks are arranged, since matrix multiplication is not, in general, commutative.

## Appendix B Euler's formula

The Euler's formulas are

$$e^{j \cdot x} = \cos x + j \cdot \sin x \quad (\text{B.1})$$

$$\cos x = \frac{e^{j \cdot x} + e^{-j \cdot x}}{2} \quad (\text{B.2})$$

$$\sin x = \frac{e^{j \cdot x} - e^{-j \cdot x}}{2 \cdot j} \quad (\text{B.3})$$

Using (B.1) to (B.3), one can derive (3.4.11) from (3.4.10) as follows:

$$r(\omega_m) = e^{\frac{-\alpha \cdot l}{2}} \cdot \left| \frac{\sin\left(\frac{-j \cdot \alpha \cdot l}{2}\right)}{\frac{-j \cdot \alpha \cdot l}{2}} \right| = e^{\frac{-\alpha \cdot l}{2}} \cdot \frac{e^{\frac{\alpha \cdot l}{2}} - e^{\frac{-\alpha \cdot l}{2}}}{2 \cdot j \cdot \frac{-j \cdot \alpha \cdot l}{2}} = \frac{1 - e^{-\alpha \cdot l}}{\alpha \cdot l} \quad (\text{B.4})$$

## Appendix C

Table I Electron mobility, carrier concentration in n-type InP at 300K [2, 3]

Carrier concentration	Electron mobility $\mu_e$ ( $\frac{cm^2}{V \cdot s}$ )	
	InP $\mu_{e\_InP}$	GaAs $\mu_{e\_GaAs}$
$1.0 \times 10^{15}$	4710	7810
$3.0 \times 10^{15}$	4570	7540
$1.0 \times 10^{16}$	4250	6980
$1.0 \times 10^{17}$	3220	5330
$5.0 \times 10^{17}$	2720	4470
$1.0 \times 10^{18}$	2570	4100
$1.0 \times 10^{19}$	1990	-

### References

- [1] David M. Pozar, microwave engineering 3<sup>rd</sup> Ed. Wiley, 174-184 (2005)
- [2] W. Walukiewicz, J. Lagowski, L. Jastrzebski, P. Rava, M. Lichtensteiger, C.H. Gatos, and H.C. Gatos, "Electron mobility and free carrier absorption in InP; determination of the compensation ratio", J. Appl. Phys. **51** 2659-2668, (1980)
- [3] W. Walukiewicz, "Electron mobility and free-carrier absorption in GaAs: determination of the compensation ratio", J. Appl. Phys. **50**(2) (1979)